UC San Diego

UC San Diego Electronic Theses and Dissertations

Title

Engineering Multifunctional Separators and Electrodes to Improve Battery Safety and Lifetimes

Permalink

https://escholarship.org/uc/item/2r23v7g5

Author

Gonzalez, Matthew Stephens

Publication Date

2021

Peer reviewed|Thesis/dissertation

eScholarship.org Powered by the California Digital Library
University of California

UNIVERSITY OF CALIFORNIA SAN DIEGO

Engineering Multifunctional Separators and Electrodes to Improve Battery Safety and Lifetimes

A dissertation submitted in partial satisfaction of the
requirements for the degree Doctor of Philosophy

in

Nanoengineering

by

Matthew Stephens Gonzalez

Committee in charge:

Professor Ping Liu, Chair
Professor Zheng Chen
Professor James Friend
Professor Shirley Meng
Professor Yu Qiao

2021

Copyright (or ©)

Matthew Stephens Gonzalez, 2021
All rights reserved.

The dissertation of Matthew Stephens Gonzalez is approved, and it is acceptable in quality and form for publication on microfilm and electronically.

University of California San Diego

2021

DEDICATION

In recognition of reading this manual before beginning to format the doctoral dissertation or master's thesis; for following the instructions written herein; for consulting with the Graduate Division Academic Affairs Advisers; and for not relying on other completed manuscripts, this manual is dedicated to all graduate students about to complete the doctoral dissertation or master's thesis.

In recognition that this is my one chance to use whichever justification, spacing, writing style, text size, and/or text font that I want to while still keeping my headings and margins consistent.

EPIGRAPH

You should never ask an engineer to explain a thing…
because he will!

-Arthur Golden

Life is like riding a bicycle.
To keep your balance
you must keep moving.

-Albert Einstein

TABLE OF CONTENTS

LIST OF FIGURES

LIST OF TABLES

ACKNOWLEDGEMENTS

I would like to acknowledge Professor Ping Liu for his support as the chair of my committee. Through the many drafts, edits, rewriting, and reworking my best work came through.

I would also like to acknowledge the rest of the Liu Lab and the other UCSD engineers and scientists who aided me along the way.

Chapter 2, in full, is a reprint of the material as it appears in Advanced Functional Materials 2021, early view, 2102198. M. S. Gonzalez, Q. Yan, J. Holoubek, M. Li, Z. Wu, H. Zhou, S. Kim, H. Liu, B-Y, J, S-W Lee, Z Chen, P. Liu. The dissertation author was the primary investigator and author of this paper.

Chapter 3, in full, is a reprint of the material as it appears in Advanced Materials 2020, 32. M. S. Gonzalez, Q. Yan, J. Holoubek, Z. Wu, H. Zhou, N. Patterson, V. Petrova, H. Liu, P. Liu. The dissertation author was the primary investigator and author of this paper.

Chapter 4, in full, has been submitted to Advanced Materials 2021. M. S. Gonzalez, Z. Wu, J. Holoubek, Q. Yan, H. Liu, P. Liu. The dissertation author was the primary investigator and author of this material.

VITA

2015	Bachelor of Science, Johns Hopkins University
2016	Master of Engineering, Johns Hopkins University
2016-2021	Research Assistant, University of California San Diego
2021	Doctor of Philosophy, University of California San Diego

FIELDS OF STUDY

Major Field: Nanoengineering

Studies in Electrochemical Materials
Professor Ping Liu

ABSTRACT OF THE DISSERTATION

Engineering Multifunctional Separators and Electrodes to Improve Battery Safety and Lifetimes

by

Matthew Stephens Gonzalez

Doctor of Philosophy in Nanoengineering

University of California San Diego, 2021

Professor Ping Liu, Chair

To meet the demand for applications ranging from cell phones to electric vehicles, battery energy density continues to rise. With the use of highly energetic materials such as Li-metal anodes coupled with a reduction of the inactive components generally tasked with safety, failure events from misuse or manufacturing defects will inevitably increase. Furthermore, catastrophic battery failures due to internal short are extremely difficult to detect and can occur even under normal working conditions. To enable next generation Li-metal batteries, an inexpensive "fail safe" mechanism for internal shorting that does not sacrifice energy density is highly desirable. In this dissertation two novel battery separator designs and an easily implementable cathode design modification have been developed to improve battery safety, control, and lifetimes by approaching these problems from both the ionic and the electronic pathways.

Firstly, an iongate separator was developed to increase battery calendar life and improve inherent safety by using a rapid and reversible battery shut-off mechanism enabled by a 10x

increase in internal ionic resistance. Secondly, a nano-composite Janus separator was implemented to intercept dendrites with a high-resistance interlayer, now controlling the internal electronic resistance of the cell. This separator provides protection and early failure detection, nearly completely eliminating short circuit current and the accompanying cell temperature rise. Lastly, this concept was simplified by using a gradient-conductivity cathode that directly utilizes the inherent resistive properties of the battery active material to create the protection mechanism, halving short circuit current and cell temperature during shorting events. This simplified approach is broadly applicable and results in a particularly inexpensive protection scheme without incurring penalty to energy density. In summary, this dissertation introduces three novel approaches to improve battery safety by controlling both the internal ionic and electronic pathways that are at fault for often catastrophic battery failures.

Chapter 1: Introduction

In response to the need of portable electronics and electric vehicles, the energy densities of lithium-ion batteries have continued to rise. In the near term, reduction of inactive materials has proven to be successful. The thickness of commercial battery separators has been reduced to <10 μm,[1] while electrode areal specific capacity [mAh/cm^2] continue to rise.[2] In the long-term, the graphite anode will be replaced by higher capacity electrode materials, namely silicon containing materials[3] and ultimately lithium metal.[4]

These changes in design and materials make battery safety an increasingly difficult challenge.[5] For LIBs, it is well known that mechanical deformation[6] and overcharging[7] can induce internal shorting and dangerous thermal runaway. However, this can also occur without discernable external cause while operating under normal conditions.[8],[9] The suspected cause of these type of events is a failure of the separator creating a low *electronic resistance* internal short circuit within the battery.[10] The challenge of separator failure further increases with the use of lithium metal anodes, especially during rapid charging when the likelihood of Li dendrite penetration increases.[11]

Approaches to improve battery safety generally add a protective element within the battery to block, drain, or cut off the short circuit. Battery separators play an essential role in this function. The addition of various porous polymer layers,[12] non-woven mats,[13] or ceramic coatings[14] have shown improvement of mechanical properties over standard polyolefin separators and aid to physically block dendrite propagation. All ceramic solid ion conductors acting as both separator and electrolyte can also suppress dendritic growth.[15] Materials can be added within the separator that are reactive towards Li and serve to etch away oncoming dendrites, but are limited by the material capacity past which dendrite propagation begins again.[16] Similarly, third electrodes

sandwiched in the separator have been implemented to detect dendrite penetration and diagnose the health of the cell.[17] Most commonly battery separators are designed with an additional layer of porous material that undergoes a phase transformation and pore collapse at elevated temperature to cut off the ionic pathway and suspend shorting—ideally accomplished before thermal runaway initiates.[18]

Another approach beyond modifying the separator is to break the electronic pathways within the electrodes themselves to limit the impact of shorting. Several methods have been developed to electronically isolate the active material. Current collectors have been designed to fracture upon mechanical deformation limiting self-discharge to small, isolated regions.[19] Positive thermal coefficient (PTC) materials have also been coated on the current collector or on the cathode itself to insulate the active material from the current collector or each other upon reaching elevated temperatures.[20],[21],[22] Unlike these temperature-trigged methods, we have recently introduced a partially electronically conductive (PEC) Janus separator to intercept oncoming dendrites. The PEC layer, in contact with the cathode, is permeable to lithium ions but adds electronic resistance to the short circuit formed when a dendrite makes contact, thus limiting the internal short circuiting current and the temperature rise, rendering the short practically harmless.[23]

All of these protection schemes, whether separator or electrode based, involve adding a component to the battery which invariably incurs increased manufacturing costs, adds to the overall volume, and increases the electronic or ionic resistance of the battery. In order for a protection scheme to be not only effective, but also economically scalable, it should ideally utilize the intrinsic properties of the electrode materials and architecture without incurring penalties in cell volume, weight, or resistance.

Chapter 2: Reversible Internal Resistance Switching Using Iongate Separators

Over the past three decades lithium-ion batteries (LIBs) have fundamentally changed society by enabling portable consumer electronics.[1] Within the next three decades LIB price ($\$ kWh^{-1}) is projected to decrease by nearly 80%,[2] while production is expected to increase 30% year-to-year.[3] LIBs remain the leading candidates for vehicle electrification[4] as well as grid-scale energy storage.[5] The demand for increased energy density coupled with ever-developing applications that require energy storage systems (ESS) continues to drive battery innovation and optimization. However, if left unaddressed the more reactive electrode materials and extreme operating conditions often required for these applications can result in faster battery degradation[6] and increasingly energetic failure events.[7]

For one, self-discharge and calendar life loss must be paid close attention to in large scale and electric vehicle (EVs) energy storage systems (ESS), particularly when operating under elevated temperatures.[8,9,10] The two primary degradation mechanisms during storage are the parasitic oxidation reactions of the electrolyte at the cathode surface, where Li^+ can then re-intercalate into the cathode upon combination with liberated electrons,[11] and dissolution of cathode transition metal ions into the electrolyte which then cross-over to and are reduced by the anode.[12] The compromised solid electrolyte interface (SEI) then consumes more active charges in order to self-repair. This results in lost capacity from the cathode itself, generation of a thicker and more resistive SEI on the anode surface, and irreversible consumptions of total Li capacity available in the cell.[6] Battery management systems can disconnect the electronic pathway between electrodes and selective ion barriers have been developed to suppress unwanted cross-over;[13,14] however, there remains no simple and reversible method to ionically isolate the two electrodes thereby avoiding this problematic cross-talk during storage.

Furthermore, extremely rapid self-discharge can occur in the event of an internal electrical short. This short can be the result of mechanical damage to the cell or from an internal defect while operating under normal conditions.[15] These short circuits can result in dangerous thermal runaway as evident by the recent ignition of EV's battery packs[16] or the Boeing Dreamliner aircraft's auxiliary power unit forcing multiple emergency landings.[17] During these severe shorting events, rapid self-discharge and Joule heating can quickly raise temperatures above the melting point of the separator and begin decomposing the electrode materials (150-250 °C), in turn triggering a chain of exothermic reactions and thermal runaway.[18,19] The use of lithium metal anodes, the demand for rapid charging, and ever thinning separators all increase the likelihood of dendrite growth and other defect-induced shorting in addition to increased risk from mechanical deformation. To improve safety performance of high energy density cells, current collectors have been designed to fracture upon mechanical deformation,[20] or with thermo-responsive polymers to electrically isolate active materials in an attempt to reduce the severity of failure events.[21] Numerous flame-retardant,[22,23,24,25] over-charge protection redox shuttle,[26] or even shear thickening[27] electrolyte additives have been developed to greatly improve battery safety; unfortunately, these are often electrochemical unstable at high voltages and sacrifice overall cell energy density.

The battery separator is a critical component that can be innovated to address these calendar life and safety challenges. Ideally, the separator should function as a reversible ion gate. Ion transport should be shut off during long-term storage or in the event of an internal short. Conversely, ion transport should remain on during charge and discharge. Most of the separator designs lack this reversibility. For example, many common battery separators go through non-reversible pore collapse at elevated temperatures which eliminates ion flux between the electrodes

before thermal runaway begins.[28] Recently, more advanced features in separators have emerged. One such separator with a metal mesh sandwiched between two porous polypropylene layers acting as a third electrode can detect dendrite penetration, but the design requires constant monitoring and does not actually prevent shorting.[29] A similar trilayer separator with reactive nanoparticles sandwiched in the middle layer was shown to etch away hazardous Li dendrites thus increasing the time-to-failure. We have recently shown that a bilayer Janus separator where one side is coated with a partially electronically conductive can not only detect the onset of dendritic shorting, but also dramatically slow the rate of self-discharge with minimal temperature rise during severe shorting events.[30]

To this point, safety design has been largely focused on controlling the electronic pathway, making it very desirable to develop a novel method that allows reversible and dynamic control of the ionic conductivity of a cell. If ion flux could be temporarily shut-off during storage, so should the self-discharge and ion cross-over while inherently improving safety. Additionally, having a mechanism that is electrochemically activated rather than thermally triggered does not require temperatures to reach dangerous levels before initiating safety features.

Here we improve battery control and safety by developing an iongate separator that exploits the switchable ionic conductivity exhibited in the conducting polymer polypyrrole (PPy) **(Figure 2.1)**. By depositing a polypyrrole membrane on a conventional polyolefin separator it is possible to fabricate an "iongate separator" that displays low ionic resistance while in its oxidized "on" state, and high ionic resistance while in the reduced "off" state. This is achieved by the rapid and reversible redox state transition of PPy where Li^+ ions are conducted via mobile anion dopants along the PPy backbone while in the "on" state, but are blocked in the non-conductive "off" state as the ions are expelled upon reduction.[31] In other words, the oxidized polypyrrole membrane can

be converted from a polycationic exchange membrane to a more neutral state upon reduction, which if sufficiently dense prevents ion crossover.[32] We demonstrate this switching can be achieved by *ex situ* means using a potentiostat connected to a third iongate electrode or by directly shorting the iongate material to the anode. Previous reports show a PPy iongate electrode can successfully prevent transient ion crossover in aqueous solutions;[32,33] however, the concept has never been demonstrated in organic electrolytes or in a battery configuration to the best of our knowledge.

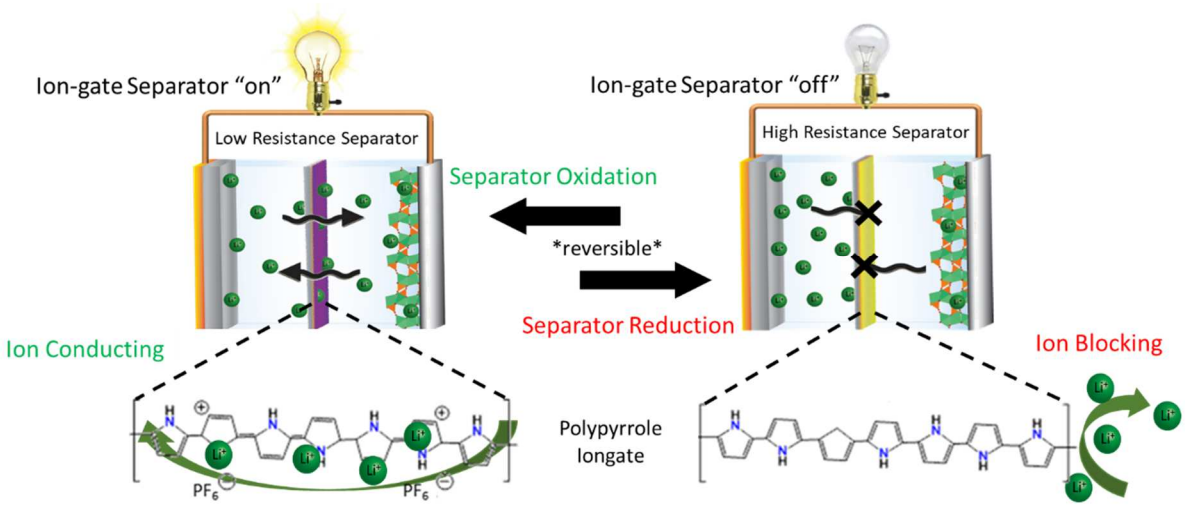

Figure 2.1: A schematic of the iongate separator in a low resistance oxidized "on" state and a high resistance reduced "off" state. While in the "on" state Li^+ ion are conducted through the oxidized Polypyrrole, whereas Li^+ ions are blocked by the reduced Polypyrrole in the "off" state.

Polypyrrole is a well-known battery and pseudocapacitor material owing to its high conductivity, chemical, and electrochemical stability.[34] Within batteries, PPy has found use in modifying electrode surfaces to improve performance of both cathode[35,36] and anode materials,[37] and even as an electrode material itself.[38,39] Additionally, electrochemical polymerization

provides a simple and versatile method to conformally deposit PPy films in a variety of configurations and morphologies.[40]

Unfortunately, PPy suffers from poor adhesion due to lack of strong intermolecular interactions between PPy and common electrode surfaces. Polydopamine (PDA) has found use as a stable adhesive polymer for a number of applications;[41] specifically, recent reports found introducing dopamine (DA) during pyrrole (Py) electropolymerization dramatically improves adhesion while maintaining electrochemical properties.[42,43] Using a ratio of 2:1 Py:DA during electrochemical deposition **(Figure 2.2**a**)** results in a well adhered polypyrrole:polydopamine (PPy:PDA) thin film on Au sputter-coated Celgard **(Figure 2.2**b**)**. Higher magnification SEM/EDS elemental mapping of the iongate separator cross-section (**Figure 2.2**c**)** shows the 300 nm PPy:PDA membrane, with N present in both the PPy and the PDA polymer, is conformally coated on and makes intimate contact with the underlay Au-coated Celgard without penetrating into the bulk of the Celgard. The Au coating was used as an electrochemically inert current collector[29] for film deposition and *in situ* switching of the iongate material, and the coating process maintains the original porosity of the Celgard surface (Supporting Information, Figure 2.S1). This Au coating layer is only ~50 of nm thick and has negligible contribution to the overall thickness of the separator.

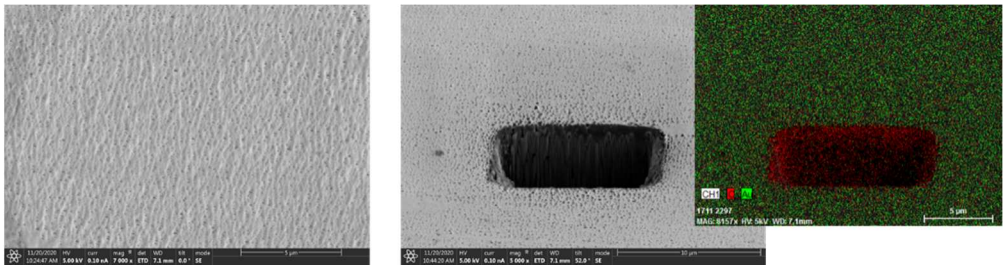

Figure 2.S1: Surface SEM and FIB cross-section SEM-EDS of Au coated Celgard showing Au solely on the surface of the Celgard while maintain surface porosity.

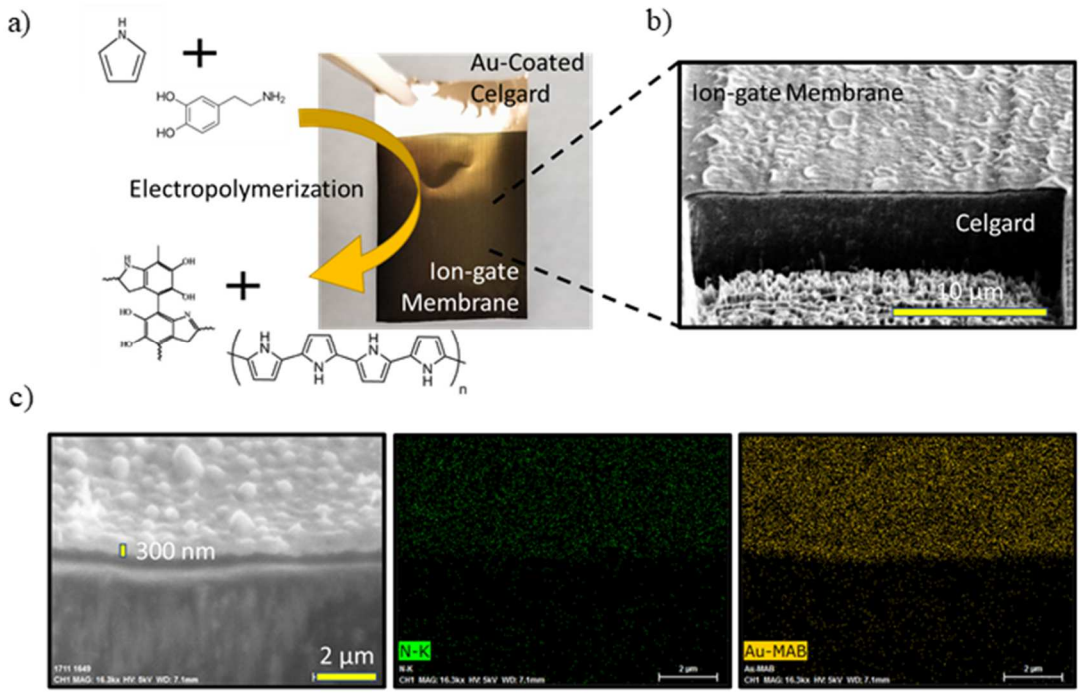

Figure 2.2: a) Polypyrrole:Polydopamine (PPy:PDA) iongate membrane electro-polymerization scheme and optical photograph of final iongate separator. **b)** Focused ion beam (FIB) cross-sectional SEM of iongate thin film polymerized directly on Au-coated Celgard. **c)** Higher magnification SEM/EDS elemental mapping showing the roughly 300 nm iongate film has not penetrated into the underlaying separator. N is present in both the PPy and PDA which cover the Au current collector to act as a third electrode.

An optimization of the membrane switching ratio vs thickness was performed and from this 300 nm was chosen as the final thickness (Supporting Information, Figure 2.S2). As the layer

becomes thinner, more pin holes form in the iongate due to underlaying surface porosity of the Celgard substrate. This allows the liquid electrolyte to leak through an ideally dense iongate layer and decreases the reduced "off-state" resistance. When the iongate layer becomes too thick, the resistance in both the oxidized and the reduced state becomes much greater than that of a conventional cell without the iongate separator and hinders battery operation at realistic current densities.

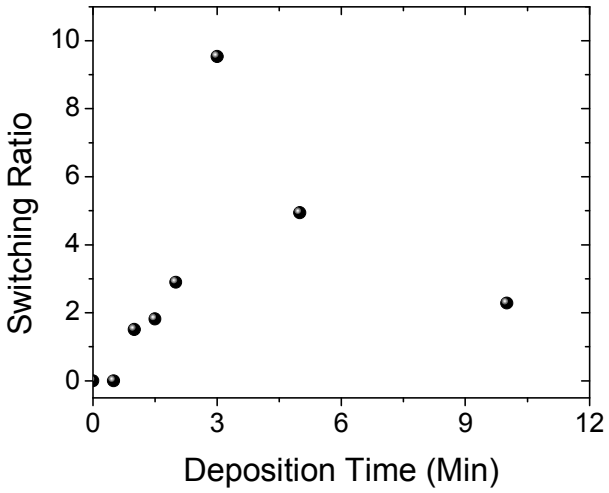

Figure 2.S2: Thickness vs switching ratio of iongate separators deposited at various times, where a 3 minute deposition resulted in the optimal switching ratio that showed good oxidized on-state conductivity to allow normal battery cycling and large reduced off-state resistance.

The deposition process for this film requires only 3 minutes using a simple potentiostatic deposition method (0.65 V vs Ag^{+}/AgCl) and occurs in a relatively non-hazard aqueous solution containing 0.1 M Py, 0.05 M DA, and 0.1 M LiTFSI as the dopant ion (Supporting Information, Figure 2.S3)**.** Raman spectroscopy confirms the co-polymerization of PPY:PDA and match

previous reports describing the copolymerization of PPy and PDA (Supporting Information, Figure 2.S4).[43]

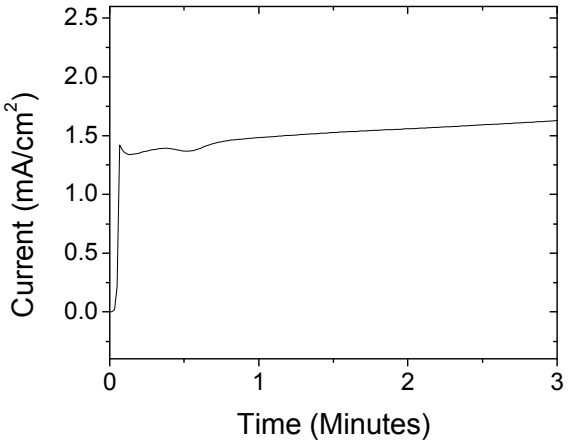

Figure 2.S3: Typical Iongate deposition profile using a 0.65 V (vs Ag^+/AgCl) potentiostatic hold.

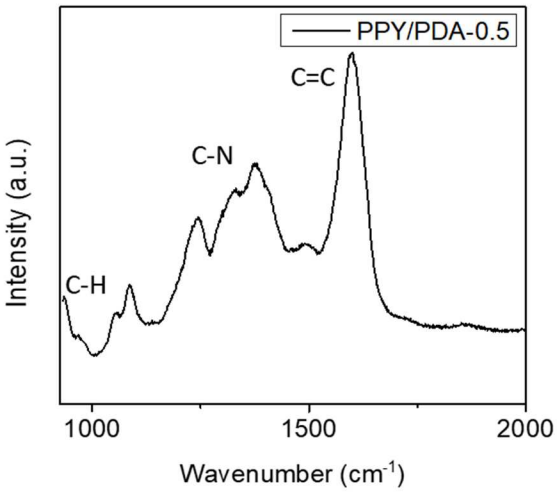

Figure 2.S4: Raman spectra of the 2:1 Py:DA deposition confirming the co-polymerization of a PPy:PDA iongate.

Additional iongate membranes were deposited with and without DA (Supporting Information, Figure 2.S5). SEM shows clear delamination from the Au coated celgard without the addition of DA. Furthermore, various ratios of Py:DA were also examined (Supporting Information, Figure 2.S6), where the higher the ratio of DA was shown to improve mechanical adhesion; however, above a 1:1 monomer ratio an undesirable porous morphology was observed. The 2:1 ratio results in the most d esirable dense morphology required for the iongate. Further details can be found in the experimental details section.

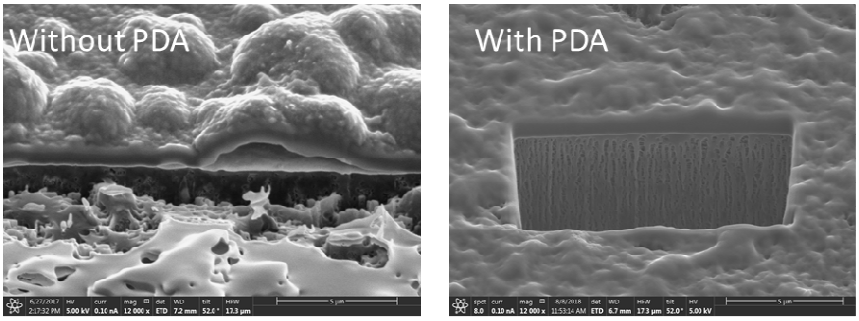

Figure 2.S5: Iongate membrane without and with PDA deposited over 10 minutes each. Delamination from the underlaying Au coated celgard is clearly visible in the film without PDA.

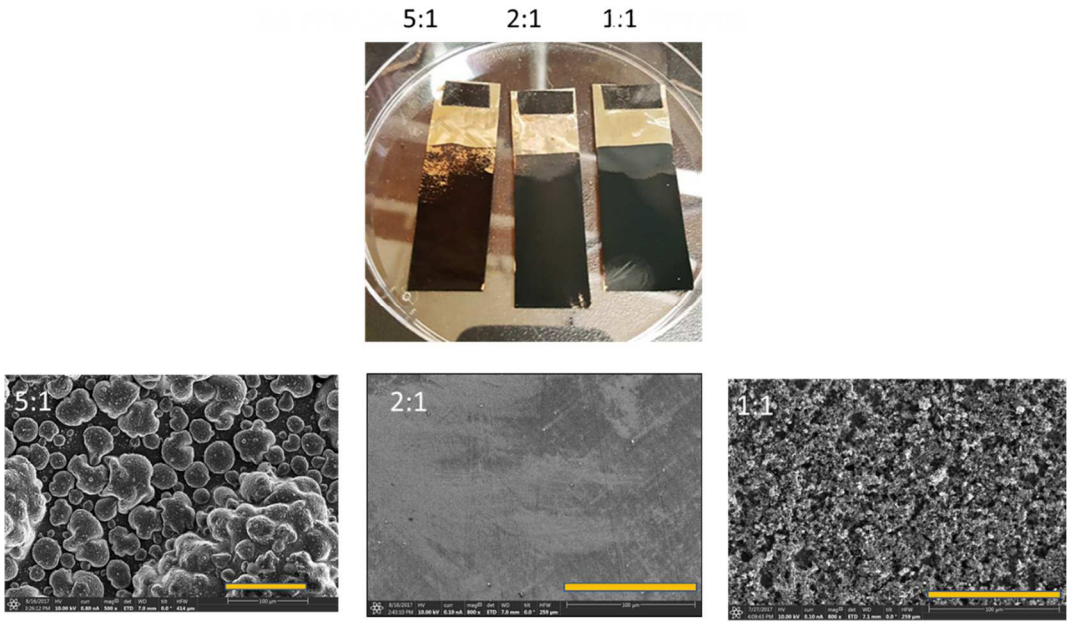

Figure 2.S6: Adhesion results performed by mechanical wiping test with a Kimwipe and surface SEM images of electrodeposited PPy:PDA iongate separators with various Py and Da precursor ratios of 5:1, 2:1, and 1:1.

Due to the hydrophilic nature of PDA, the iong ate separator exhibits exceptional wettability. The iongate membrane over the top of the hydrophobic polypropylene Celgard dramatically improves the overall wettability of the iongate separator when compared to a pristine Celgard separator (Supporting Information, Figure 2.S7).

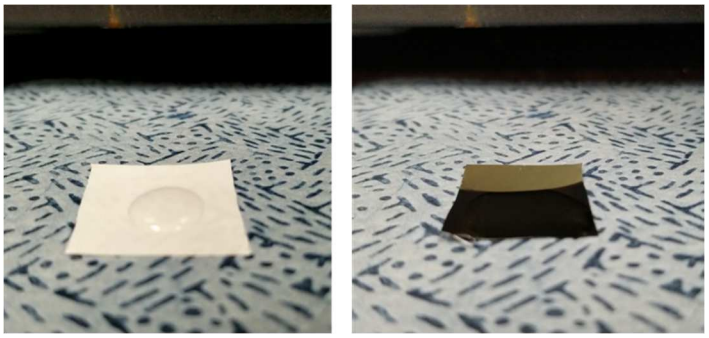

Figure 2.S7: Wettability test using 1:1 wt% EC:DMC on pristine Celgard and the iongate separator.

To measure the electrochemical performance of the iongate separators, a three-electrode cell was assembled in both Li/iongate/Li and Li/iongate/NMC configurations as seen in **Figure 2.3**a. The potential of the iongate separator can be controlled through this third electrode contact to reduce or oxidize the iongate material. This is akin to discharging (reducing) and charging (oxidize) the iongate electrode, wherein discharging de-dopes the PPy material switching it to the "off-state" while charging re-dopes the PPy switching it to the "on-state."

These cells used LP30 as the electrolyte (1M $LiPF_6$ in EC:DMC 1:1 wt%). Pouch cells were fabricated to have an third electrode[44] contact to the iongate separator through the exposed Au-coated Celgard remaining from the deposition process. An additional pristine Celgard was used to insulate the iongate membrane coated side from the other electrodes—the backside of the separator remains pristine Celgard. Further details can be found in the experimental details section.

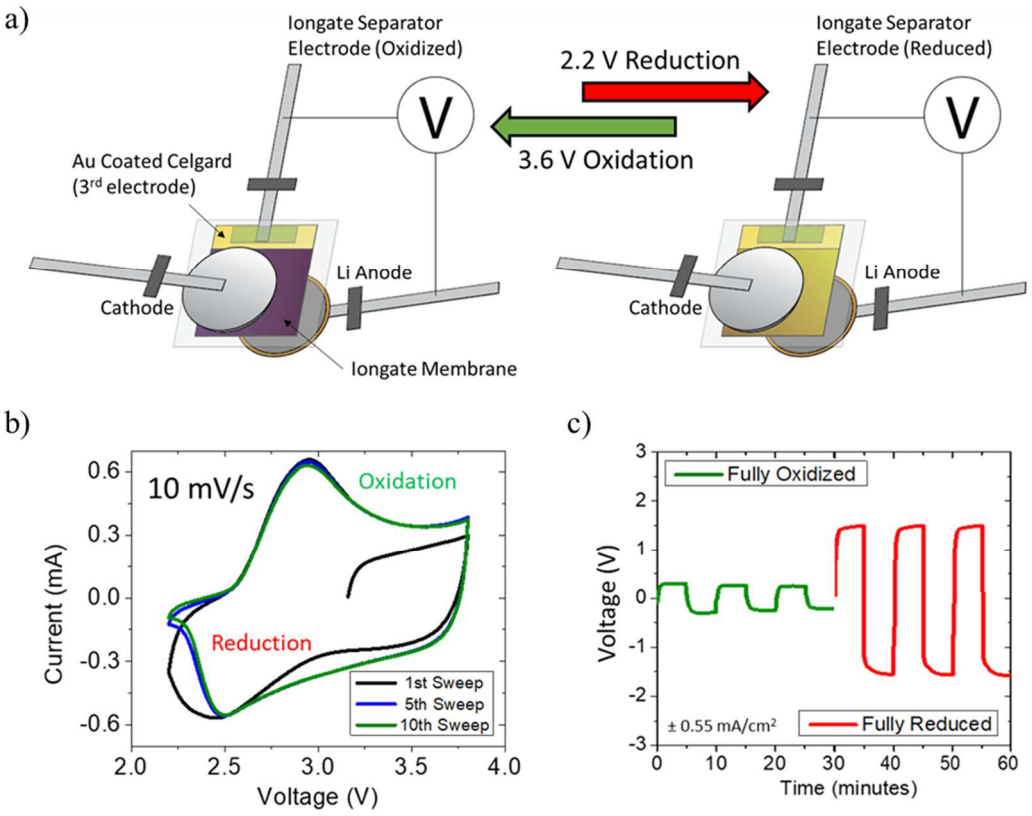

Figure 2.3: a) Schematic of three-electrode configuration for both Li/iongate/Li and Li/iongate/NMC cells where an additional contact is made to the iongate separator. Through this additional contact various voltage can be applied to reduce (2.2 V) or oxidized (3.6 V) the iongate separator. **b)** Cyclic voltammetery of the iongate separator using a Li metal electrode as the counter and reference electrode. **c)** DC voltage profile showing resistance switching between the oxidized "on" state and the reduced "off" state.

Cyclic voltammetry of the iongate separator using the Li electrode as a counter and reference was performed to determine the redox properties. Two highly reversible redox peaks appear around 2.9 V for oxidation and 2.5 V for reduction using a scanning rate of 10 mV s^{-1} **(Figure 2.3**b**)**. There is a distortion during the 1st reduction compared to subsequent voltage sweeps likely due to expulsion of $TFSI^-$ dopant used during deposition. Since the overall amount of PPy in the cell is so small, less than 0.0005 M $TFSI^-$ is expected to be in solution and should not result in significant change to the electrolyte. During the following oxidation PF_6^- from the bulk

electrolyte is re-doped into iongate membrane and the peaks remain stable and highly reversible as seen by the 5th and 10th voltage sweeps. With this information, 3.6 V and 2.2 V were chosen as stable potentiostatic oxidation and reduction switching potentials for the follow across-membrane tests to ensure complete redox of the iongate.

The Li/iongate/Li configuration was used to measure the across-membrane DC resistance of the film in the oxidized "on" state and the reduced "off" state **(Figure 2.3**c**)**. After the CV shown in **Figure 2.3**b, the iongate separator was held at 3.6 V for 30 minutes in order to ensure full oxidation of the iongate material. A DC square-wave current of ±1 mA (0.55 mA cm^{-2}) was then applied across membrane and a resulting voltage polarization of roughly 250 mV was measured between the two Li electrodes. The iongate was next held at 2.2 V for 30 minutes to reduce the membrane, and again a current of ±1 mA was applied across membrane resulting in a voltage polarization of 1500 mV. From this data, the iongate areal resistance of the oxidized state and reduced state was determined to be 255 Ωcm^2 and 2443 Ωcm^2. These are calculated by subtracting off the average baseline resistance of 200 Ωcm^2 (*i.e.,* a cell with only pristine Celgard (Supporting Information, Figure 2.S8)) from the resistances measured in the iongate cell while in the on- and off-states to determine the added resistance of solely the iongate separator, yielding a reversible iongate switching ratio of nearly 10x.

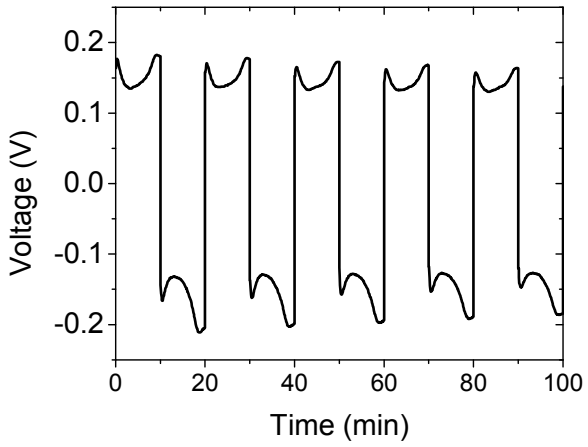

Figure 2.S8: Square-wave voltage profile of Li/Li baseline cell using 0.90 mA cm^{-2} without an iongate separator and two pristine Celgard separators showing a nominal areal resistance of roughly 200 Ωcm^2.

Additional common battery electrolytes were tested to confirm the robustness of the iongate concept. Since the iongate is deposited in LiTFSI, a 1 M LiTFSI in 1:1 wt% EC:DMC electrolyte was first tested in the Li/iongate/Li configuration. This similarly exhibited nearly an order of magnitude switching ratio in the iongate material between the oxidized and reduces states. The validity in an ether based electrolyte was also tested using 1 M LiTFSI with 0.5 M $LiNO_3$ in 1:1 DOL:DME. While still showing clear switching, the magnitude of switching was slightly less—roughly 5x—owing to increased "off-state" conductivity despite similar redox characteristics as seen by the cyclic voltammetry. Further optimization and better understanding of iongate/electrolyte swelling interactions may be required for these systems; regardless, it appears that the iongate concept can be applied to numerous electrolyte systems. Detailed results can be found in Supporting Information, Figure 2.S9.

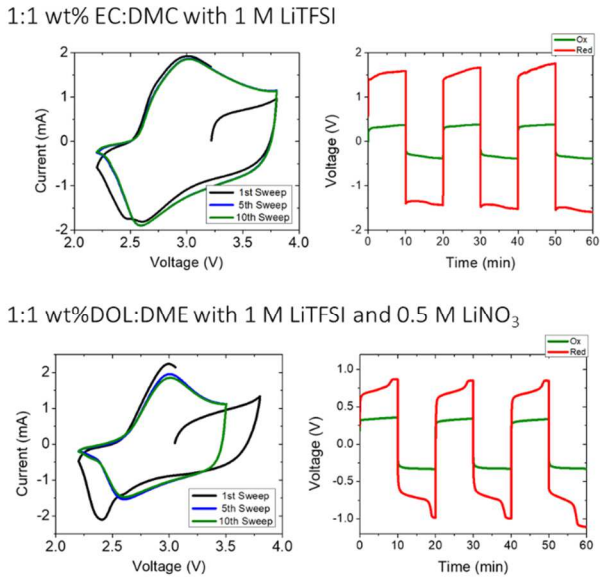

Figure 2.S9: Li/Iongate/Li switching in additional electrolytes 1:1 wt% EC:DMC with 1 M LiTFSI showing roughly 8x iongate switching ratio and 1:1 wt% DOL:DME with 1M LiTFSI and 0.5 M $LiNO_3$ showing a switching ratio of roughly 5x. The CV scan rate was 10 mV s^{-1} and the DC current was 1 mA cm^{-2}.

To better understand the doping (oxidation) and de-doping (reduction) process, which is critically important to iongate working mechanism, XPS was performed on an oxidized and reduced sample of the iongate separator (Supporting Information, Figure 2.S10). The doping level of the $TFSI^-$ counterion ion the oxidized state was calculated using the XPS survey scan to be 23%, or roughly one dopant ion for every four repeat pyrrole units, indicating a highly dope material. The doping level is effectively 0% for the reduced state indicating full reduction of the iongate material.

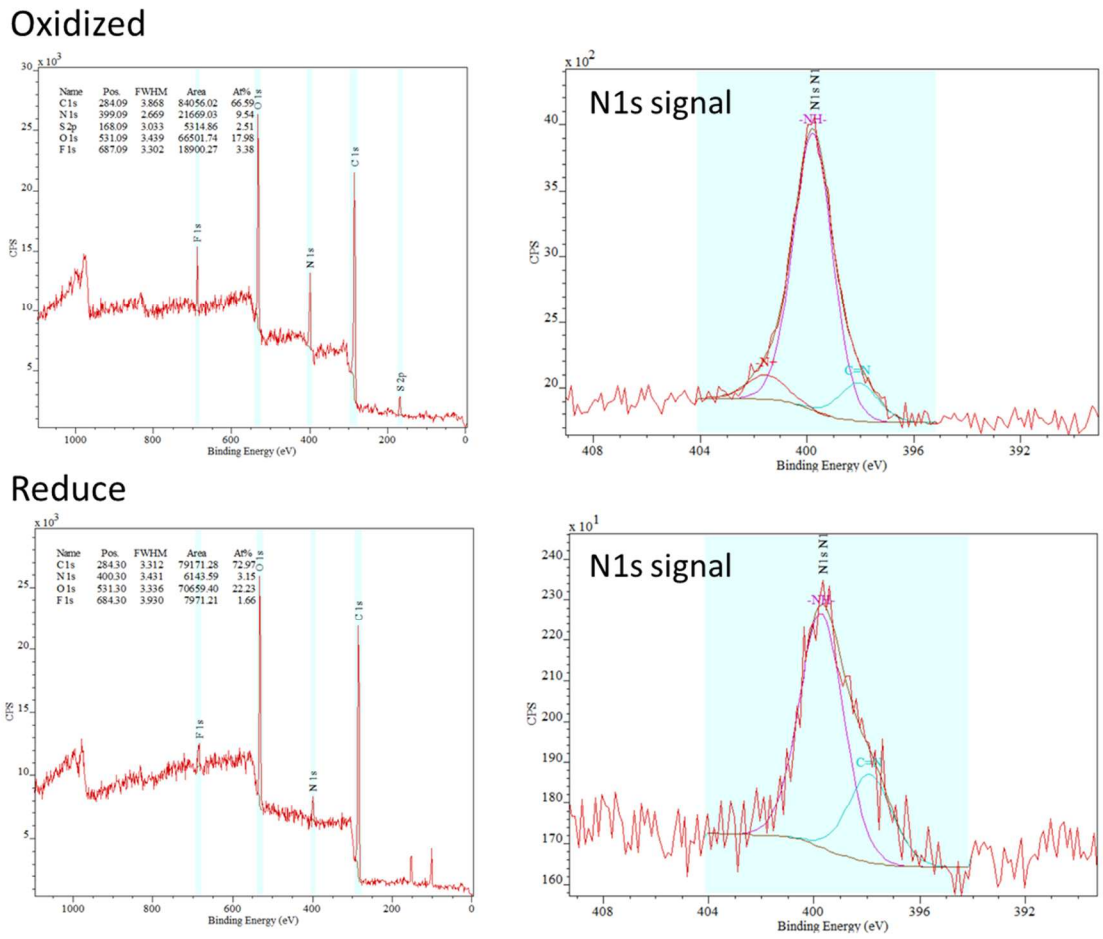

Figure 2.S10: XPS survery and N1s spectra of the oxidzed and reduced iongate. These calculations consider a 2:1 ratio of S:N attributed to the $TFSI^-$ dopant and a 2:1 of PPy:PDA, where ultimately the ratio of $TFSI^-$:PPy is evaluated. Furthermore, the N1S signals were also fitted. The peaks were deconvoluted into the neutral amine structure (-NH) assigned to 399.5 eV, an additional neutral imine structure (=NH) assigned to 398 eV, and a charge bipolaron structure ($-NH^+$) signal assigned to 401.5 eV. Upon reduction the biopolaron ($-NH^+$) signal completely disappears and we observe an increase in the relative imine (=N) signal indicating the conversion of charged N species to neutral N groups.

We next evaluated the iongate separator as a barrier for dissolved transitional metal ions, a well known challenge when lithium-ion batteries are stored at elevated temperatures. Here we choose a Li/iongate/NMC configuration, hereafter referred to as "iongate battery" **(Figure 2.4)**. A "normal battery" was also fabricated without the iongate separate (*i.e.* only pristine Celgard).

Further details of the battery fabrication can be found in the experimental details section. It should be noted that to ensure the iongate material was in a fully oxidized state before battery cycling the iongate separator underwent cyclic voltammetry and a 30-minute oxidation hold at 3.6 V, as performed in **Figure 2.3**. The cells were then cycled at a ra te of C/20 between 2.7-4.5 V with a 4.5 V hold until current decayed to C/40 for the first two cycles and the third charge process. The iongate was then reduced using a 2.2 V hold and pinned to that potential for storage. Both cells were then stored in this fully charged state at 55 °C for approximately 2 weeks to promote ion dissolution and self-discharge[45] while measuring OCP in storage (Supporting Information, Figure 2.S11). The iongate cell measured a higher OCP throughout storage appearing to significantly suppress the initial potential decay by ~50 mV after 2 days and remained >10 mV higher after 14 day. Cells were returned to room temperature and the iongate was reoxidized using a 3.6 V hold for 30 mins. After this aging process, the cells were then discharge using a rate of C/40 at room temperature and the remaining capacity from the previous charge was 96.4% and 94.3% for the iongate battery and the normal battery, respectively **(Figure 2.4**a **&** d**)**. This equates to a capacity loss reduction of approximately 37%. This noticeable improvement in capacity retention is attributed to the reduced state iongate's ability to largely limit the crossover of ions across the separator during high temperature storage.

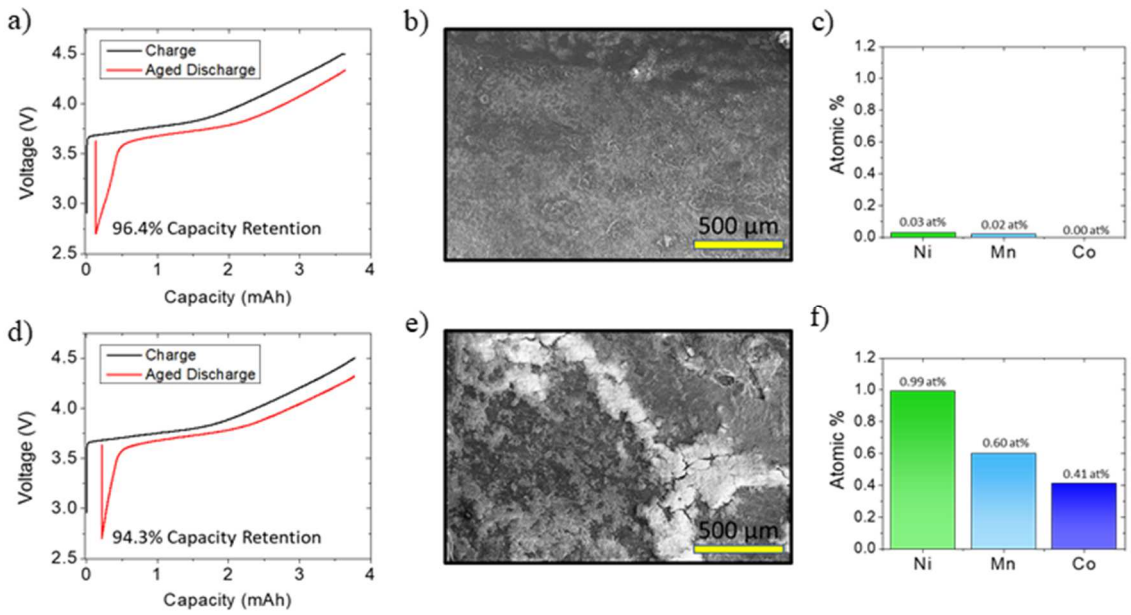

Figure 2.4: a) Charge and subsequent aged discharge profile of a battery with an iongate separator after being stored in the charged state for two weeks at 55 °C. During storage, the iongate separator was reduced, placing the battery in an "off-state" to limit spontaneous ion cross-over and self-discharge. **b)** SEM of the Li metal anode surface after the 55 °C storage and discharge showing a uniform and dense SEI layer, and **c)** EDS elemental survey of the shown area with almost no transition metals (*i.e.* Mn, Co, Ni) detected. **d)** Charge and subsequent aged discharge profile of a normal battery without an iongate separator stored in the same conditions. **e)** SEM of the Li metal anode surface after the 55 °C storage and discharge showing a very non-uniform SEI that greatly varies in thicknesses. **f)** The EDS elemental survey of this area with a significant amount of transition metals detected.

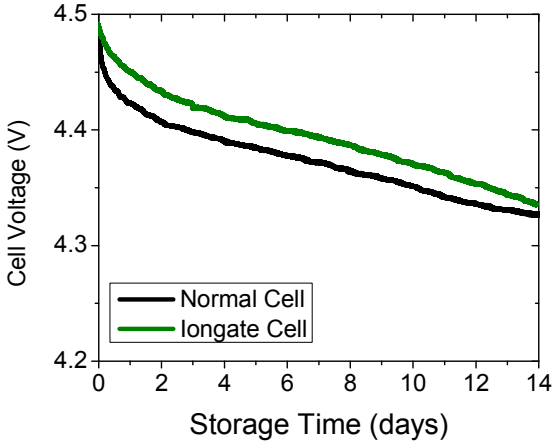

Figure 2.S11: Measured OCP of the charged normal and iongate cell while being stored at 55 °C for two weeks.

Our hypothesis is supported by the difference in morphology and chemical composition of the SEI formed on the Li metal anode surface during storage. After the final discharge, both cells were disassembled, and the Li metal anodes were gently washed using pure DMC solvent. SEM of the anode surface show two very different morphologies: The iongate battery anode has a relatively uniform and dense SEI **(Figure 2.4**b**)** whereas the normal battery anode SEI is very inhomogeneous with areas of greatly varying thickness **(Figure 2.4**e**)**. It is well known that non-uniform SEIs are extremely prone to future dendrite growth due to irregularities in surface resistance and Li^+ ion flux.[46] EDS elemental mapping for these anode areas (Supporting Information, Figure 2.S12) show the iongate battery has a uniform distribution of C, O, F, and P—common components of SEI associated with LP30 electrolyte[47]—with almost no transition metal signal, while the normal battery has high concentrations of C, O, F, P and additional signal from Ni, Mn, and Co in the thicker regions of the SEI. The elemental survey of the iongate battery anode detects at most 0.03 at% of any transition metal **(Figure 2.4c)** whereas the normal battery has

approximately 2 at% of the SEI comprised of transition metals in a nearly exact ratio of 5:3:2 (Ni:Mn:Co) that agrees with the cathode chemistry **(Figure 2.4**f**)**. Full elemental survey data can also be found in Supporting Information, Figure 2.S12. Clearly the iongate effectively suppresses transition metal ion cross-over and dramatically improves SEI formed at these elevated temperatures and during long periods of storage time..

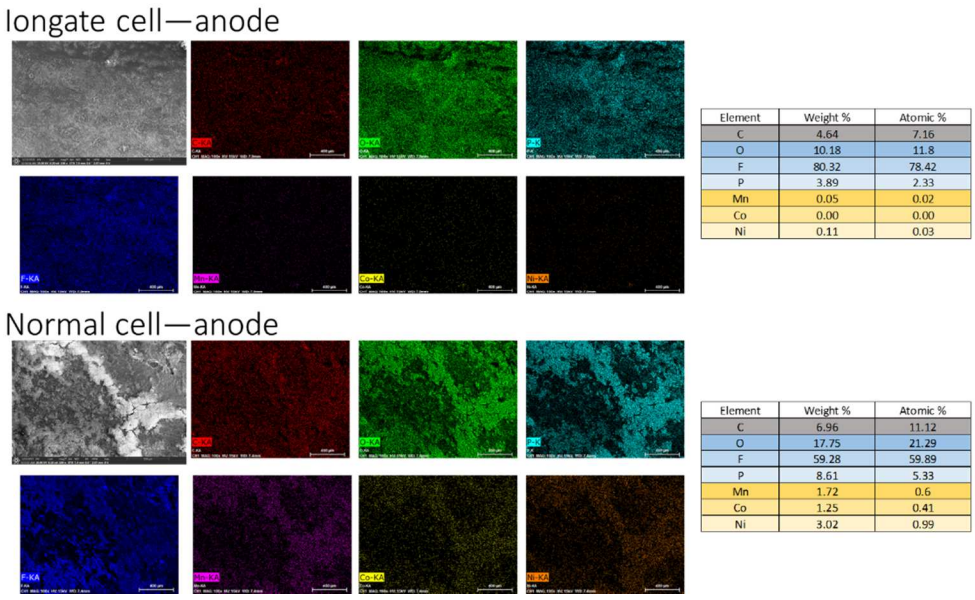

Element	Weight %	Atomic %
C	4.64	7.16
O	10.18	11.8
F	80.32	78.42
P	3.89	2.33
Mn	0.05	0.02
Co	0.00	0.00
Ni	0.11	0.03

Element	Weight %	Atomic %
C	6.96	11.12
O	17.75	21.29
F	59.28	59.89
P	8.61	5.33
Mn	1.72	0.6
Co	1.25	0.41
Ni	3.02	0.99

Figure 2.S12: SEM-EDS of the Li metal anode surfaces of the iongate and normal cell after 2 week storage at 55 °C. The iongate shows uniform distribution of C, O, P, and F with almost no signal detected for Mn, Co, and Ni. The normal shows non-uniform distribution of C, O, P, F and additional significant signal from Mn, Co, and Ni.

Lastly, the iongate separator shut-off performance was evaluated in an iongate battery configuration **(Figure 2.5)**. Again, to ensure the iongate was in a fully oxidized state before battery cycling the iongate separator underwent cyclic voltammetry and a 30-minute oxidation hold at 3.6 V, as performed in **Figure 2.3 & 2.4**. Cycling of the cell with the iongate separator in the "on"

state shows performance similar to a conventional cell at charging rates of C/10, C/5, and C/3 **(Figure 2.5**a**)**. All discharge rates were maintained at C/10. However, when the iongate separators is reduced at 2.2 V for 30 minutes and cycling is resumed negligible capacity is achieved at C/3, effectively resulting in complete battery shut-off due to large polarization of >1 kΩ. This is reflected in the cell impedance rise measure by EIS in **Figure 2.5**b. The spectra were best fitted with an equivalent circuit as shown in Supporting Information, Figure 2.S13 with 3 RC elements correspond to the cathode, the anode, and the iongate separator, respectively. Fitting results show a large increase of nearly 10x in the resistive element of the iongate component which matches well with the results seen in DC measurements. This indicates that the iongate in the "off" state shows a dramatically reduced rate for ion transport. This observation is further supported by EIS measurements of the iongate separator as the working electrode (Supporting Information, Figure 2.S14), which most notably shows a huge increase (nearly two orders of magnitude) in the Warburg diffusion tail element when the material is reduced, denoting the reduced rate of diffusion processes within the iongate material. It is this decrease in diffusion rate in the iongate materi al itself that translates to the switching performance observed in the full cell.

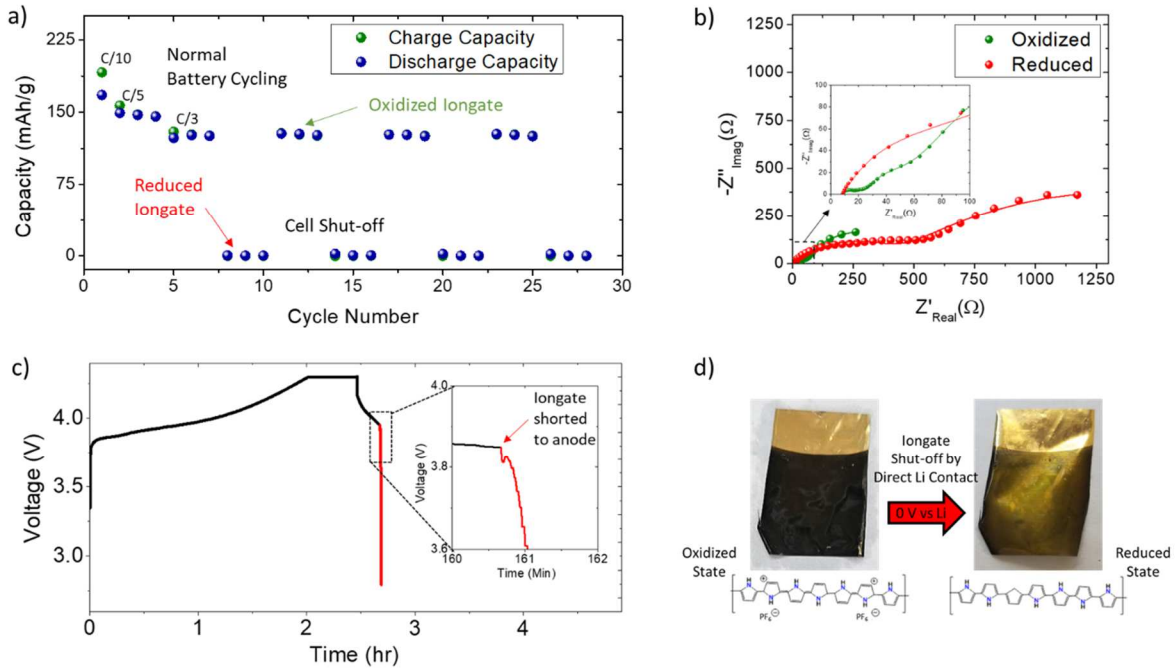

Figure 2.5: a) Cycling and *ex operando* switching capacity profile of an Li/iongate/NMC cell showing similar performance to a conventional cell while the iongate is in the oxidized "on" state, but cell shut-off while the iongate is in the reduced "off" state. The dots are measured data points and the lines are fitted results. **b)** Full cell EIS spectra showing the cell resistance difference between the two iongate redox states. c**)** Voltage profile of rapid *in operando* cell shut-off achieved by directly shorting the iongate separator electrode to the Li anode. **d)** Optical images showing iongate color change after direct shorting at 0 V to the Li anode.

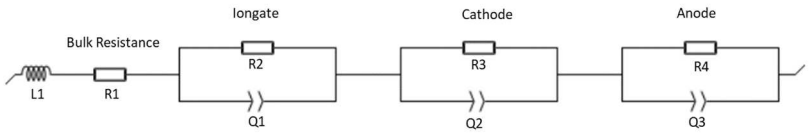

Fitting equation: L1+R1+R2/Q1+R4/Q3+R3/Q2

Circuit Component	Oxidized	Reduced
L1 (H)	0.151 7e-6	0.151 7e-6
R1 (Ω)	7.438	7.438
R2 (Ω)	173.4	1 839
Q1 (F.s^(a - 1))	0.155 5e-3	0.937 8e-3
a1	0.567	0.49
R3 (Ω)	456.8	370.8
Q2 (F.s^(a - 1))	3.69E-03	2.10E-05
a2	0.797	0.619
R4 (Ω)	33.6	33
Q3 (F.s^(a - 1))	1.08E-03	0.477 5e-6
a3	0.807	0.988

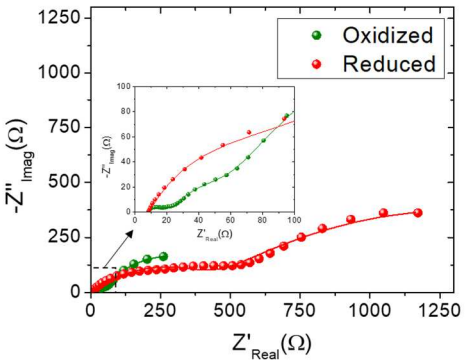

Figure 2.S13: EIS Fitting of the NMC/Iongate/Li metal cell where NMC is the working electrode and Li metal is the counter/reference. The EIS spectra were fitted to an equivalent circuit that consisted of three RC elements that represented the iongate material, the anode, and the cathode, respectively, along with an inductor L (due to wiring) and R (other contact and ionic resistances). For C, the capacitive element, a constant phase element, Q, is always used instead. The fitting is excellent and the parameters are listed in the table as shown below, were we observed a large increase of 10x in the resistive element of the iongate component (R2) between the oxidized and reduced state.

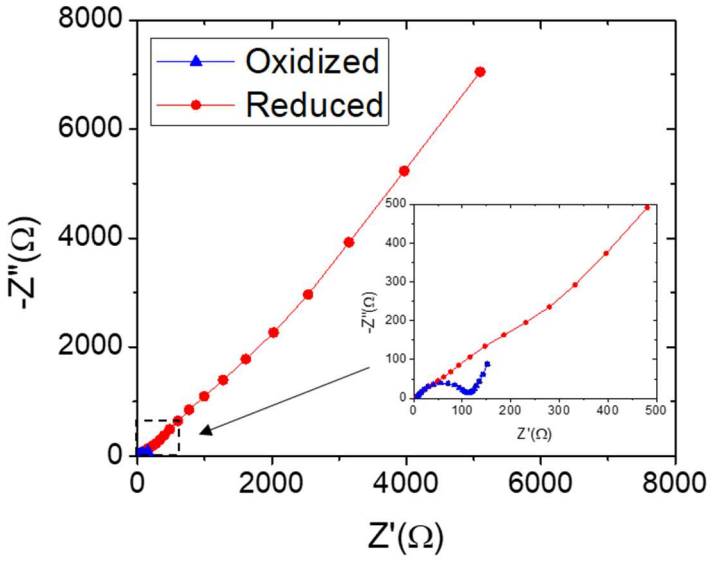

Figure 2.S14: EIS measure of the iongate separator itself (*i.e.* the iongate separator is the working electrode and the Li metal anode is the counter and reference) in the oxidized and reduced state.

Additionally, a cycling stability test was perform comparing a normal cell without the iongate separator to a cell with an iongate separator that was kept in the oxidized state throughout the entirety of cycling. The addition of the iongate has a negligible effect on cell capacity and cycling stability although the re is an increase in cell resistance (Supporting Information, Figure 2.S15).

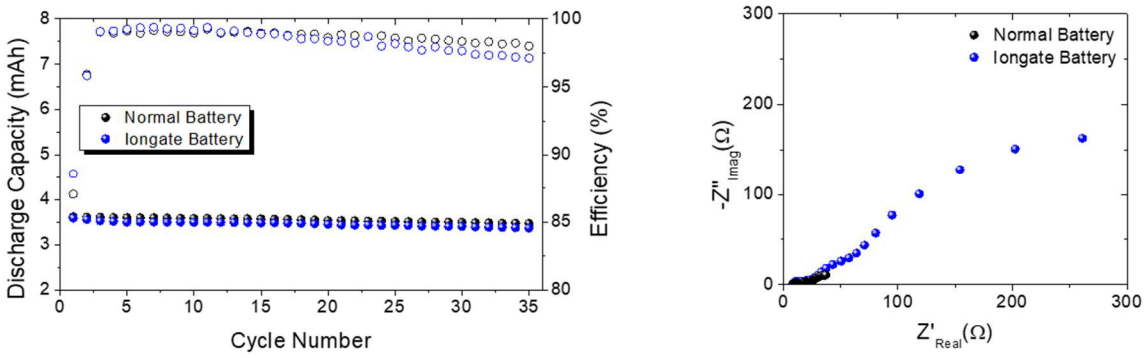

Figure 2.S15: Cycling stability test of a normal battery without the iongate separator and a battery containing an iongate separator that was maintained in the oxidized state through the entirety of cycling. EIS impedance shows an increase in resistance due to the addition of the iongate separator which translate to a minor decrease in capacity due to resistive losses.

While 30-minute potential holds were applied to the iongate to ensure full oxidation or reduction during most of our experiments, due to the pseudocapacitive nature of PPy as an electrode material the majority of switching capacity is achieved in a matter of seconds (Supporting Information, Figure 2.S16). Considering this rapid oxidation state switching of the iongate, *in situ* shut-off of the cell was investigated by directly shorting the iongate separator to the anode during discharge of the battery **(Figure 2.5**c**)**. By externally shorting the iongate separator to the 0 V Li anode, rapid reduction occurs with concurrent increase in overall cell impedance. This in turn results in cell shut-off as the discharge voltage rapidly decayed to the 2.7 V lower cut-off limit. The inlay of the discharge voltage profile highlights the moment the iongate is shorted and the fall in cell voltage, where this process only takes 10s of seconds. *Post mortem* optical image of the reduced iongate separator shows a clear color change from the original darker oxidized state to a yellow-ish hue indicating that the direct contact with Li has indeed fully reduced

the entire separator to an "off" state **(Figure 2.5**d**)**. This color change is to be expected as PPy is a well know electrochromic material,[48] marking an effective safety mechanism during failure events such as Li dendrite penetration or mechanical deformation that would short the iongate to the anode.

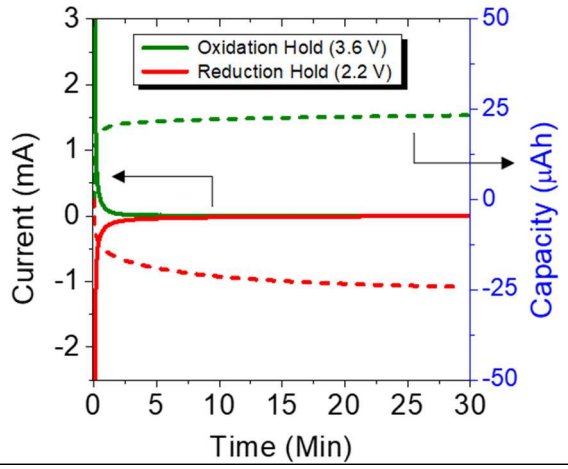

Figure 2.S16: Iongate switching profile vs Li metal anode using 3.6 V oxidation hold and 2.2 V reduction hold.

In summary, we have developed an ultra-thin (300 nm) polypyrrole/polydopamine (PPy:PDA) iongate membrane coated directly on a conventional Celgard separator that is capable of rapid and reversible switching of its ionic conductivity. The iongate separator maintains flexibility and displays improved wettability. A switching ratio of 10x was achieved between its oxidized "on" state and reduced "off" state. This iongate separator represents a novel approach to battery safety and control by allowing dynamic control of the separator ionic conductivity and overall ion flux. When storing a battery with the iongate separator in the reduced "off" state, ion flux can be dramatically suppressed. The iongate battery showed approximately 37% reduction in capacity loss verses a normal cell and nearly completely eliminated transition metal (Ni, Mn, Co) crossover when stored at 55 °C for two weeks. The iongate battery also displays cycling

performance similar to a normal battery while in the "on" state, but effectively shuts-off of the cell when the iongate is reduced to the "off" state. Furthermore, the iongate can be turned off by directly shorting it to the lithium anode, pointing to its potential as a safety mechanism in the event of an internal short. Improvements to performance still remain, but there is an extensive library of conducting polymer materials with similar properties that show great promise for future development of iongate separators for battery and other electrochemical storage applications.

Experimental Section/Methods

Au Sputter Coating Celgard: Celgard 2400 was cut into large square (10 cm x 10 cm) and gently cleaned with ethanol and Kimwipe to remove any dust and other surface contaminates. These squares of Celgard were then placed into the vacuum chamber of a Ladd / Hummer™ 6.2 sputter coat machine equipped with an 99.999% Au target and Ar gas. The vacuum chamber was evacuated to 80 mTorr with a steady flow of Ar and 7 minutes of sputter coating was performed at a current of 20 mA. This results in an approximately 10 nm Au coating on the surface of the Celgard estimated according to the standard deposition rates for the system published by the manufacturer.

Distillation and Purification of Pyrrole: The pyrrole monomer was purified before each deposition using a simple distillation process. The purified pyrrole solution appeared clear and was stored in a refrigerator in a sealed vial under an Ar blanket to prevent oxidation in ambient air.

Ion-gate Deposition Solution: The deposition solution is 0.1 M pyrrole and 0.05 M dopamine for the 2:1 ratio (for other ratios the pyrrole concentration remains 0.1 M and dopamine is altered), and 0.1 M $LiClO_4$ or 0.1 M LiTFSI all dissolved in 18 mohm water prepared by reverse osmosis. This solution is stirred for at least 10 minutes to ensure a well-mixed solution.

Ion-gate Deposition Process: The Au coated Celgard was connected to Gamry Interface 1000 potentiostat as the working electrode, a stainless-steel shim as the counter electrode, and an Ag/AgCl electrode as the reference. These were secured in place parallel to each other and dipped into the deposition solution so that about 6 cm of the Celgard is submerged and 4 cm is left as exposed Au. To improve deposition quality the deposition solution is slightly stirred (magnetic stir bar at 300 RPM) and cooled using an ice bath to reach a temperature below 5 °C.

To electro-polymerize the PPy:PDA onto the Au coated Celgard, a constant potential of 0.65 V (vs Ag/AgCl) was applied. The deposition time determines the thickness of the ion-gate membrane and 180 seconds results in the 300 nm LiTFSI dope membrane.

The deposited ion-gate separators were removed from the solution and rinsed in a di-ionized water bath three times to remove excess monomers and salt. They were dried overnight before assembling into other electrochemical cells.

XPS Characterization: XPS spectra (Supporting Information, Figure 2.S10) used to calculate the doping level of iongate material was performed by a PHI Quantera SXM, Scanning X-ray Microprobe and was carried out using Al anode source at 15 kV and all the peaks were fitted based on the reference C–C bond at 284.6 eV. All XPS measurements were collected with a 300 mm × 700 mm spot size using a charge neutralizer during acquisition. Survey scans were collected with a 1.0 eV step size, and were followed by high resolution scans with a step size of 0.05 eV for N1s regions.

Li/ion-gate/Li Cell Set up: A symmetric three electrode pouch cell was used to measure ion-gate across membrane performance as seen in **Figure 2.3**. Two 15 mm diameter disks of Li were pressed onto Cu foil and a Ni tab was taped to the backside as a current collector. The ion-gate separator was placed between the Li disks and an additional pristine Celgard separator was

used to prevent the exposed PPy:PDA membrane from contacting the Li metal. An additional Al tab was taped to the exposed Au coated Celgard to provide electrical contact to the iongate separator The entire cell was filled with LP 30 (1 M $LiPF_6$ in 1:1 EC:DMC), or other electrolyte, and seal using an MTI vacuum sealer within a Ar filled glovebox.

Cyclic voltammetry (CV) and the potentiostatic voltage holds to switch the redox states were performed using the ion-gate separator/Au Contact as the working electrode and the Li electrode 1 as the counter and reference electrode. The CV was performed at 10 mV sec^{-1} sweeping between 2.2 V and 3.8 V and the voltage holds to reduce and oxidized the ion-gate were performed at 2.2 V and 3.8 V for 30 minutes to ensure full switching. The working electrode was then disconnected from the ion-gate separator and switched to Li electrode 2. Across membrane DC galvanostatic testing and AC impedance were performed immediately after the end of the ion-gate switching voltage holds. ±1 mA (0.57 mA cm^{-2}) was applied for the DC measurement and AC impedance was acquired between 7 Mhz to 10 mHz at open circuit potential.

Li/ion-gate/NMC Pouch Cell Parameters and Testing: Small pouch cells were assembled with the ion-gate separator between a Li metal anode and NMC532 ($Li_xNi_{0.5}Mn_{0.3}Co_{0.2}O_2$) cathode and used for testing results shown in **Figure 2.4 & 2.5**. The cathode has a capacity of 2.2 mAh cm^{-2} and contains NMC532, CNT, and PVDF in a mass ratio of 97.5:1:1.5 on Al foil (Hunan Hong Xiang New Energy Technology CO.LTD). These were cut into 1.77 cm^2 disks and contacted with an Al tab tapped to the back. The anode current collector was a copper sheet with a Ni tab tapped to the back. 500 um thick Li disk with an area of 2.27 cm^2 was rolled onto the surface of the Cu inside of an Ar glovebox (O_2 < 1 ppm , H_2O < 1 ppm). The ion-gate separator area was at least 4.2 mm x 4.2mm to ensure full coverage of the active area with an additional pristine Celgard to prevent physical contact with the electrode. An Al tab was pressed and tapped directly to an area

exposed Au that was outside of the active material area. The laminated pouch cell was sealed using a MTI MSK-115A-S vacuum sealer in an argon filled glove box after approximately 0.5 mL of electrolyte (excess) was added. Parafilm and plexiglass sheets were used to apply pressure to the cell and ion-gate contact with spring loaded clamps.

Acknowledgments:

Chapter 2, in full, is a reprint of the material as it appears in Advanced Functional Materials 2021, early view, 2102198. M. S. Gonzalez, Q. Yan, J. Holoubek, M. Li, Z. Wu, H. Zhou, S. Kim, H. Liu, B-Y, J, S-W Lee, Z Chen, P. Liu. The dissertation author was the primary investigator and author of this paper.

Chapter 3: Bleeding Out Short Circuits With The Janus Separator

Lithium-ion batteries have enabled the consumer electronics society[1] and are the leading candidate for vehicle electrification[2] and grid storage.[3] Further increase in energy density is necessary to reduce battery size, weight, and cost. In the near term, without changing active materials, the focus has been on reduction of the inactive mass in the battery. For example, the thickness of commercial battery separators has been reduced to ~10 μm[4] and the electrode thickness and areal specific capacity [mAh cm^{-2}] continue to rise.[5] In the long term, new electrode materials are being proposed to replace the graphite anode, first with silicon containing materials,[6] finally with lithium metal.[7]

The relentless pursuit of higher energy density presents challenges in battery safety.[8,9] A thinner separator raises the danger of puncturing and the use of lithium metal introduces the possibility of dendrite penetration and shorting. In the case of a short, Joule heating from the large current induced by rapid self-discharge through the low resistance electronic pathway can bring temperatures to the break down point of the separator and the electrode materials (150-250 °C),[10] setting off a chain of exothermic reactions and thermal runaway.[11,12] Internal shorting can be induced by external causes such as mechanical deformation (e.g. during nail penetration tests[13,14]) and overcharging, but can also occur for no discernable external cause, as exemplified by recent incidents in self ignition of parked electric vehicles.[15] Postulated mechanisms include the growth of conductive filaments in batteries which eventually penetrate the separator and short the cell.[16] Various approaches of preventing and managing Li-ion battery thermal runaway have been developed, which include pressure release vents, [17] advanced battery management systems to prevent overcharging, current collectors that are designed to fracture in order to electronically isolate the short circuit,[18] and fire retardant additives.[19]

Among the battery components, battery separators are primarily responsible for preventing and managing battery shorting and thermal runaway. Thermally responsive separator are engineered to collapse or expand in response to high temperatures, blocking ion-flow to effectively shut off the cell.[20,21] With the help of a third electrode, separators are able to detect a penetrating dendrite.[22] Alternatively, mechanically robust separators can in principle block internal shorting due to lithium dendrite penetration.[23,24,25] Among them, separators based on porous polymeric materials and non-woven mats have shown improved mechanical properties over conventional polyolefins.[26] Ceramics particles, commonly alumina or silica, are either coated on the separator or mixed into the separator to improve thermal shrinkage resistance but also have been shown to physically obstruct dendrite propagation.[27,28,29,30,31] Furthermore, all ceramic solid ion conductors with high modulus can act both as the separator and the electrolyte to suppress dendritic growth.[32] However, these more robust blocking separators often only serve to delay dendritic penetration and the subsequent shorting can results in an even more violent failure.[33]

Table 3.S1: Nomenclature used in the modeling

Nomenclature	
R_{Short}	Total resistance of the internal short [Ω]
R_{Den}	Resistance of lithium dendrite [Ω]
R_{PEC}	Added electrical resistance of the PEC layer of the Janus separator [Ω]
R_{Int}	Total internal cell resistance [Ω]
R_o	Bulk internal resistance of the cell [Ω]
R_p	Charge Transfer Resistance [Ω]
C_p	Capacitive effects from electrical double layer [F]
R_{Tot}	Total cell resistance [Ω]

A separator that can allow controlled and safe shorting of a battery—while still ultimately resulting in cell failure—is an attractive alternative to separators that block and simply prolong time to catastrophic failure. Controlling the resistance of the internal short circuit (R_{Short}) is crucial to mitigating shorting and rapid self-discharge. This can be accomplished by inserting a partially electronically conductive (PEC) separator material with tunable electronic conductivity between the anode and the cathode **(Figure 3.1**a**)** to intercept the oncoming dendrite and effectively increase the short circuit resistance (R_{short}). Since the layer is electronically conductive and would naturally result in a short circuit itself, an additional fully insulating separator material placed between the PEC material and the anode is required to prevent this. The PEC material can be directly coating on the electronically insulating material, resulting in a single Janus separator. When a dendrite penetrates the electronically insulating side and is intercepted by the PEC side, the additional resistance provided by the PEC side (R_{PEC}) forms the circuit seen in **Figure 3.1**b. Additionally, both are required to be sufficiently ionically conductive to leave normal battery performance unimpeded (R_{Int}). Table S1, Supporting Information lists the nomenclatures used in the circuits. Conversely, once a dendrite has fully penetrated a conventional single layer separator it has no means to prevent a low resistance internal short circuit from forming, rapidly discharging the cell and potentially resulting in thermal runaway **(Figure 3.1**c&d**)**.

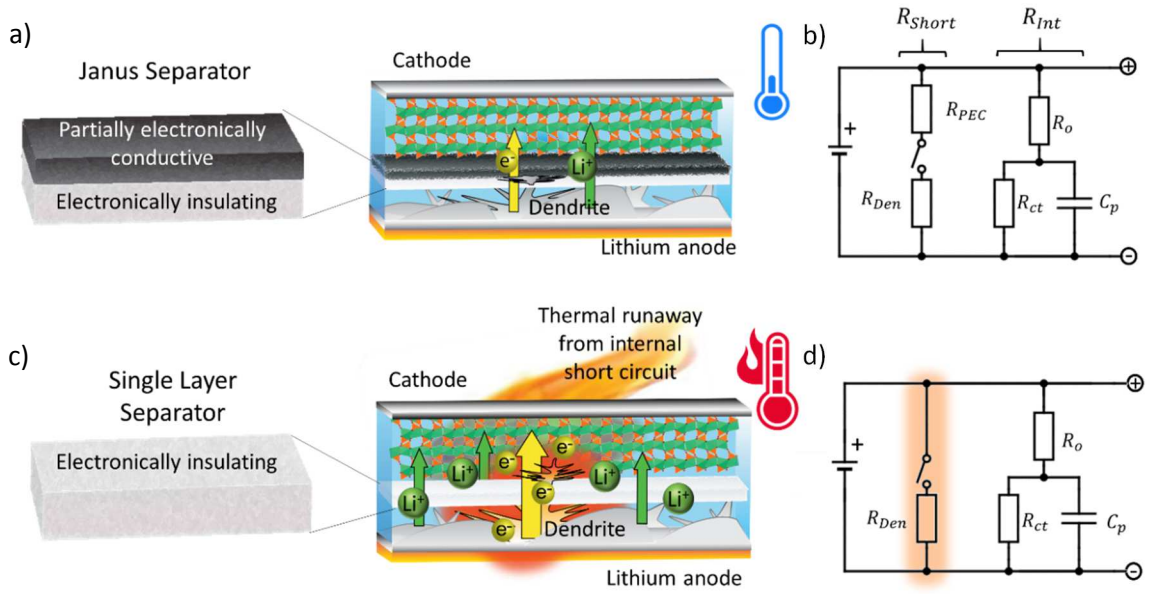

Figure 3.1: a) Schematic of the Janus separator implemented in a lithium battery. The black side is partially electronically conducting (PEC) and the white side is electronically insulating. The Janus separator limits the rate of self-discharge by intercepting the dendrite and increasing the short circuit resistance. b) The Thévenin equivalent circuit of the cell containing a Janus separator during internal shorting with the additional resistance, R_{PEC}, from the Janus separator. c) Schematic of a single layer separator implemented in a lithium battery. A dendrite penetrates the separator resulting in rapid self-discharge of the cell and thermal runaway. d) The Thévenin equivalent circuit of the cell containing a single layer separator during internal shorting

In order to easily incorporate an electronically conductive filler and reproducibly study dendrite penetration through these separators, we chose a PVdF-HFP:SiO_2 polymer gel electrolyte as the base separator material.[34] This system, while not as commonly seen in contemporary commercial production, was originally developed and commercialized by Bellcore[35] and makes for an excellent proof-of-concept platform to study shorting behavior. The separator provides a high ionic conductivity (10^{-3}-10^{-4} Scm^{-1})[36] and relatively poor mechanical properties with a tensile strength ~5MPa (compared to polyolefins, >100 MPa) that is well suited for dendritic

shorting experiments. The PVdF-HFP gel electrolyte was additionally chosen since it enables fabrication of a monolithic Janus separator—where both layers cofntain the same polymer gel structure.

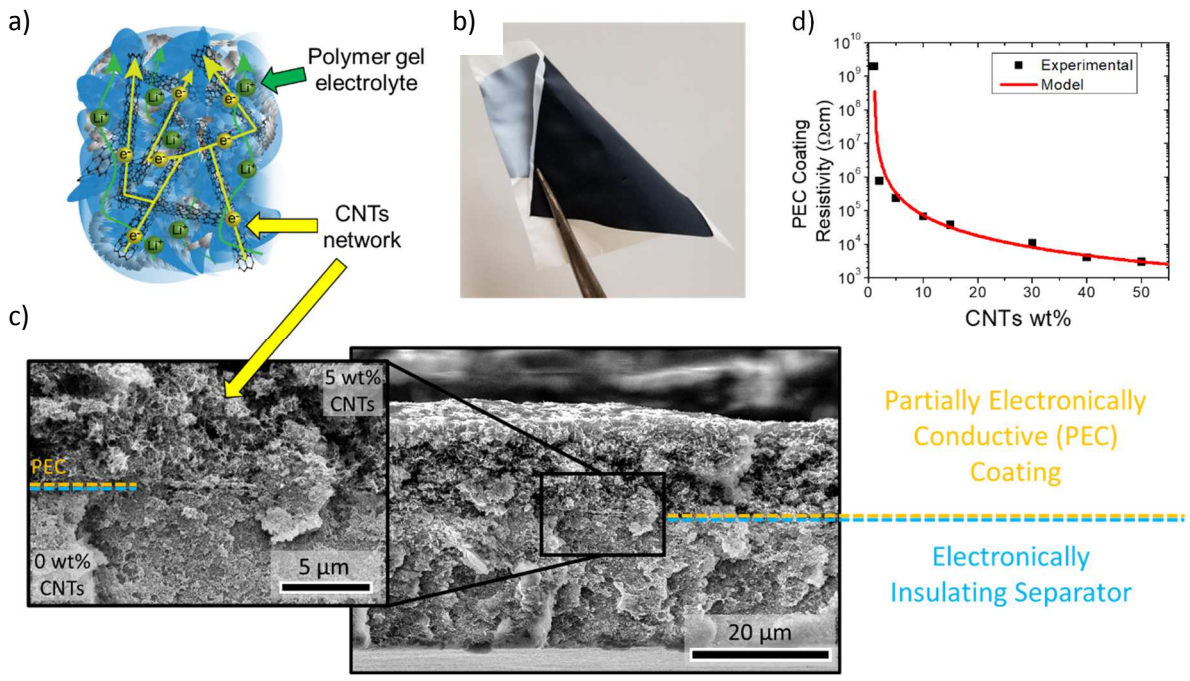

Figure 3.2: a) Schematic of the proposed structure of the polymer gel PVDF-HFP:SiO_2/CNTs nano-composite. b) Photograph of the Janus separator: the black side is a partially electronically conductive (PEC) layer containing 5 wt% CNTs, and the white side is fully insulating with no CNTs. c) Cross-sectional SEM image of the Janus separator at the interface between the PEC coating (top) and the electronically insulating separator (bottom) and of the full separator showing a distinct morphology between the two sides. d) The measured resistivity of freestanding PEC polymer gel composites with various weight loadings of CNTs and the power law model fit.

The separators were fabricated by solution casting a mixture of PVdF-HFP (poly(vinylidene fluoride-co-hexafluoropropylene)), fumed silica, and a plasticizer followed by phase inversion. By incorporating multi-walled carbon nanotubes (CNTs), a nano-composite PEC layer can be formed in which Li^+ ions diffuse through the polymer gel electrolyte and electrons conduct along the CNT network **(Figure 3.2**a**)**. To make the Janus separator shown in **Figure 3.2**b, a polymer gel electrolyte layer containing 0 wt% CNTs is first casted and allowed to dry. Then a PEC polymer gel electrolyte layer containing 5 wt% CNTs is coated directly on top of first layer.

More details can be found in the experimental section. Scanning electron microscopy (SEM) of the cross section **(Figure 3.2c)** of such a Janus separator shows a defined yet intimate interface and distinct morphological difference between the 5 wt% CNTs PEC side and the 0 wt% electronically insulating side. Since the PEC layer is coated on a dry insulating layer, the CNTs appear to be unable to penetrate more than 1 μm past the interface despite being of the same base material, maintaining the integrity of the insulating side of the Janus separator. This is further supported by measuring negligible current when a DC voltage is applied across the Janus separator comparable to that seen with single layer electronically insulating separator (Figure 3.S1, Supporting Information). The overall thickness of the Janus separators is approximately 35 μm, where the PEC side is roughly 15 μm and the insulating side is roughly 20 μm, and is comparable to thicknesses used in commercial applications.

Table 3.S2: General Separator Properties

	Modulus [MPa]	Tensile Strength [MPa]	Electrolyte uptake [g/mm^3]	Bulk Ionic Conductivity (@RT)	Shrinkage Onset Temperature
Single Layer	3.57	3.85	0.157	2.3 E-3 Scm^{-1}	>280 °C
Janus	2.77	4.15	0.156	2.1 E-3 Scm^{-1}	>280 °C

We next characterized the mechanical, thermal, and electrochemical stabilities of the Janus separator. Tensile tests show a maximum stress of 4.2 MPa, a slight improvement of ~0.3 MPa to the tensile strength compared to a single layer 0 wt% separator. The small difference is not

expected to meaningfully change the ability of the separators to block dendrite propagation or otherwise affect shorting mechanism (Figure 3.S2, Supporting Information). Separator wettability and electrolyte uptake is unaffected by the incorporation of CNTs, although the

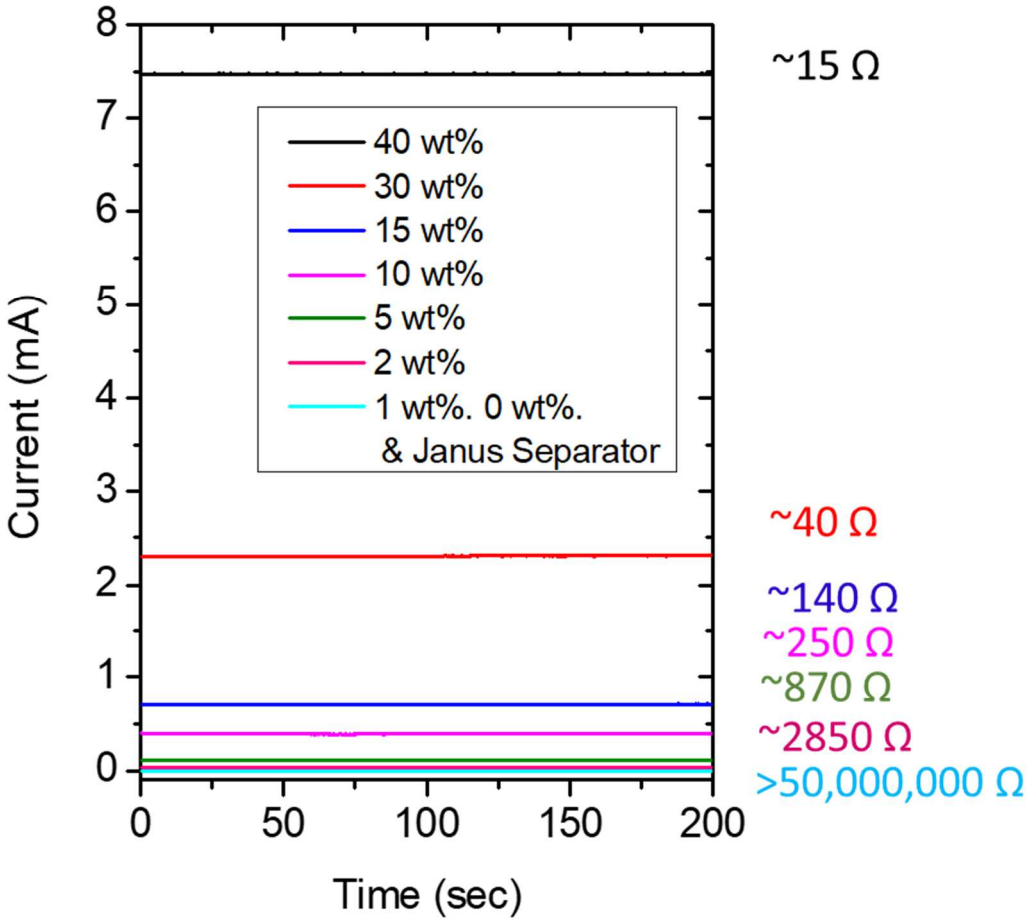

Figure 3.S1: Electronic conductivity measurement of the dry freestanding PEC separators using a DC voltage of 100 mV. Measurements of the 1 wt%, 0 wt%, and the Janus separator resulted in current in the nA to pA range and can be considered fully electronically insulating. This was converted to resistivity and plotted in **Figure 2.2 C.** The power-law relation is defined by the equation:

$$\sigma = \sigma_0 (V_f - V_c)^s$$

where σ is the electrical conductivity of composite, σ_0 is the electrical conductivity of the filler, V_f is the filler volume fraction, V_c is the percolation threshold (1 wt%), and s is a conductivity exponent back calculated from experimental results.

separator no longer becomes transparent when wet and remains dark black (Supporting Video 1). The addition of CNTs also had no observed effect on thermal stability as both separators show no shrinkage at temperature >280 °C (Figure 3.S3, Supporting Information).

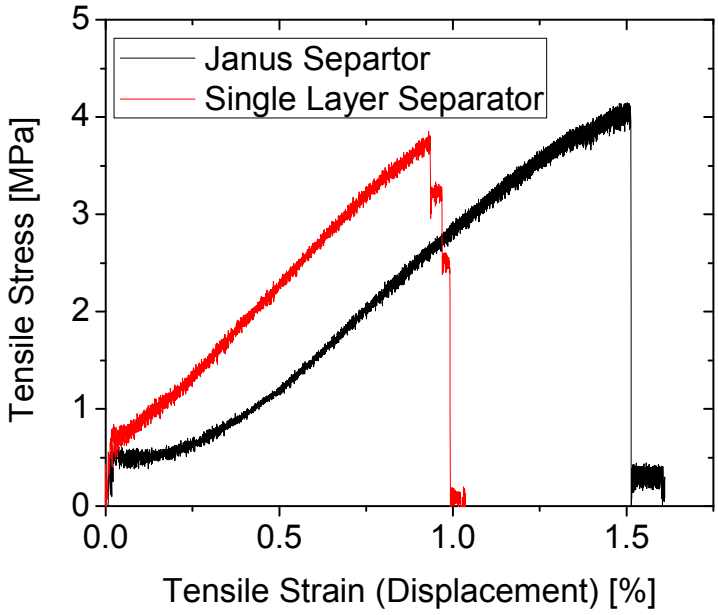

Figure 3.S2: Tensile test of the Janus separator and the single layer separator. The Janus separator has a slight improvement to tensile strength over the single layer separator, ~0.3 MPa.

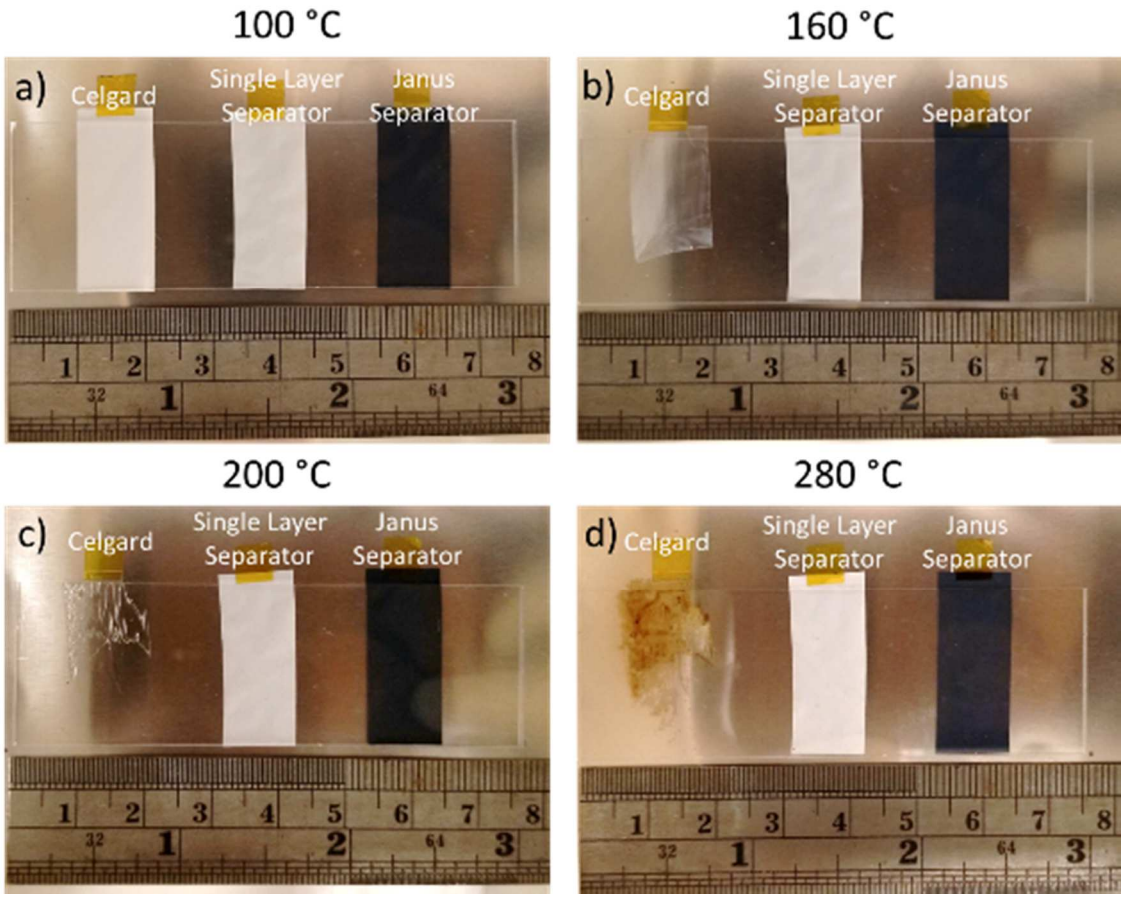

Figure 3.S3: Thermal stability test of Celgard2400, the single layer separator, and the Janus separator after 10 minutes a) at 100 °C b) at 160 °C where shrinkage is observed with Celgard c) at 200 °C where the Celgard has melted and become fully transparent, and d) 280 °C where the Celgard shows burnt coloration. Neither the single layer separator nor the Janus separator display any change in this temperature range.

Linear sweep voltammetry does indicate a reaction between the CNTs and electrolyte at voltages above 4 V (vs Li/Li^+), as is common with the conductive carbon additives use in cathodes[37], but passivates after multiple sweeps (Figure 3.S4, Supporting Information). In fact, the magnitude of parasitic current between the baseline and Janus separator is negligible if one takes into account the large surface area of the CNT network. Indeed, CNTs are used as the

conductive agent in the cathode for this study. Additionally, Bellcore originally applied the polymer gel electrolyte directly to construct the composite cathode containing carbon and the oxide cathode materials—similar to the construction of the Janus separator—and did not report additional side reactions. Furthermore, by varying the amount of CNTs incorporated into the PEC side, control of its electronic conductivity is easily achieved and can be altered by orders of magnitude **(Figure 3.2**d**)** to match the demands of batteries of various formats and capacities. Freestanding PEC membranes were cast with CNT loading ranging from 0-50 wt% (Figure 3.S5 & 3.S6, Supporting Information), with electronic resistivity that varies by nearly 10^3-10^6 Ω cm when measured using a DC voltage bias across the membrane (Figure S1, Supporting Information). The electrical conductivity follows a power law relation with CNT wt% that is consistent with percolation theory and is modeled in **Figure 3.2**d.[38] To test the Janus separator's ability to intercept dendrites and create a controlled short circuit, Li/NMC ($LiNi_{0.5}Mn_{0.3}Co_{0.2}O_2$) coin cells with 1 M $LiPF_6$ in 1:1 ethylene carbo nate:dimethyl carbonate (EC:DMC) electrolyte were cycled at a rate of 2 mA cm^{-2} (or ~1.2 C). It is well known that these conditions result in a slow buil d-up of dendritic lithium which can eventually penetrate the separator and short the cell.[39],[40] By choosing a mechanically weak polymer gel electrolyte as the base separator material, dendrite penetration and internal shorting can be achieved long before other sources of cell failure occur (e.g. dead Li build up, electrolyte depletion, *etc*).[41] We note that dendrites do grow at much lower current densities where the Janus design will still function as designed.

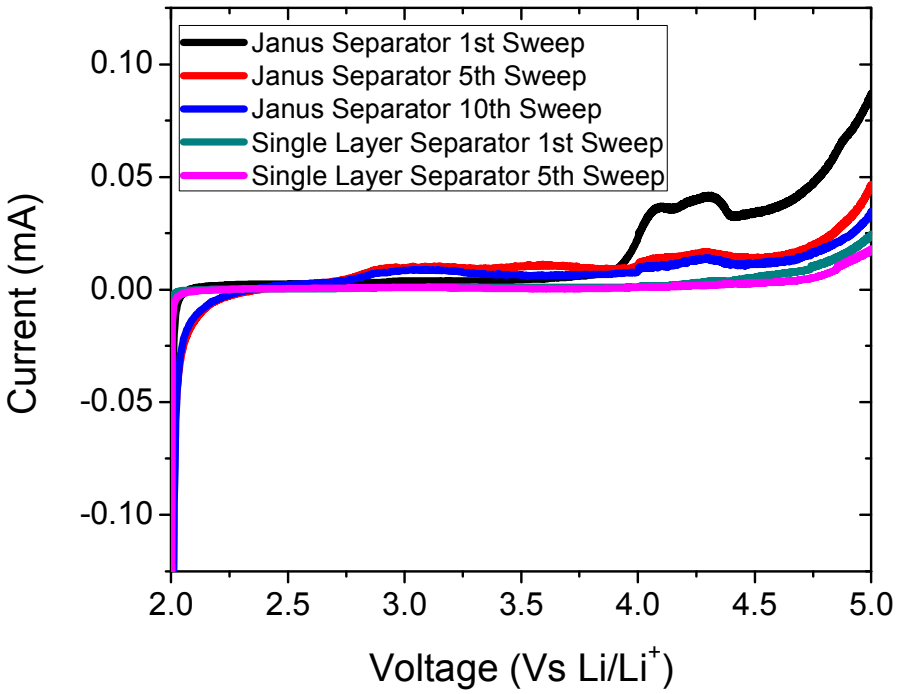

Figure 3.S4: Linear Sweep Voltammetry of Li/Stainless Steel coin cells with the Janus separator and with the single layer separator. The first sweep of the Janus separator shows additional reaction between the CNTs and the electrolyte but begins to passivate by the 5th sweep, and further passivates by the 10th sweep.

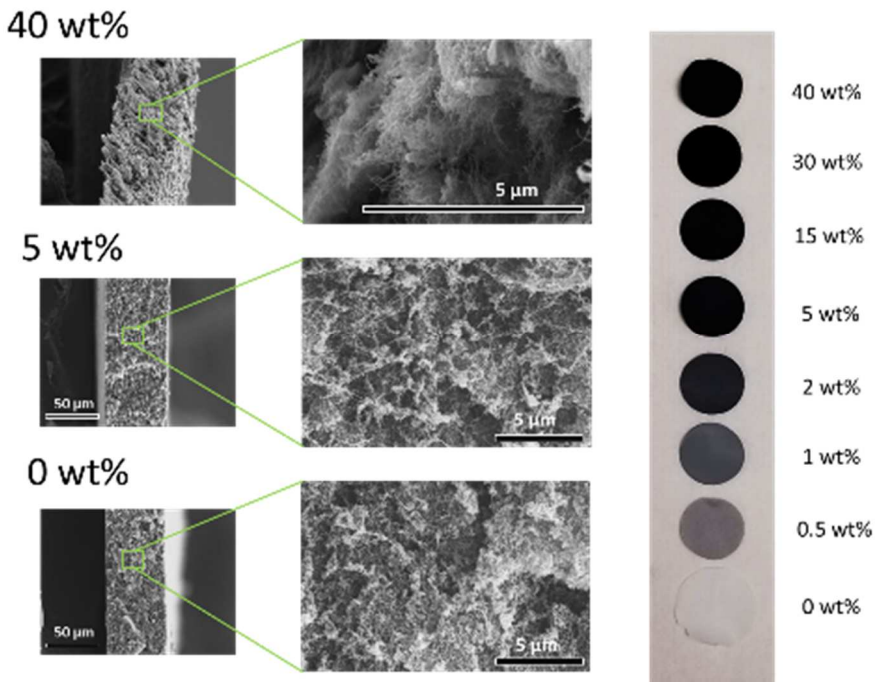

Figure 3.S5: SEM images of cross sections of freestanding PEC separators with 0 wt%, 5 wt%, and 40 wt% CNT loadings. As the weight loading increases the fibrous CNTs become apparent in the nano-composite and the morphology becomes "fuzzier" but still maintains porosity. Also shown is a photograph of coin cell sized PEC layers with various weight loadings of CNT.

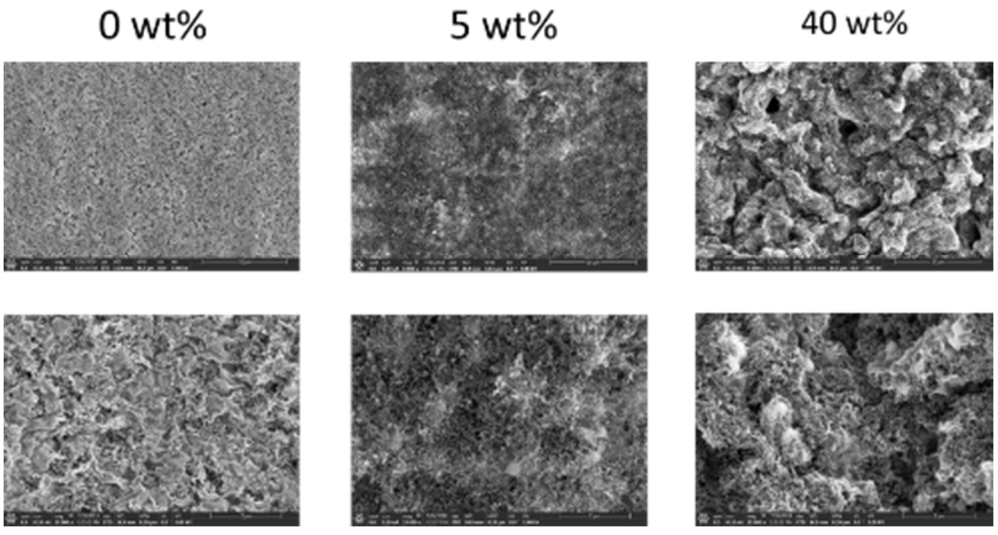

Figure 3.S6: SEM images of the surface of the freestanding PEC separators with different weight loadings of CNT. As the volume becomes dominated by CNTs the separators becomes more of a loose mat than a robust film.

Coin cells containing a Janus separator (as seen in **Figure 3.1**) were compared to cells containing ~40 μm thick single layer separator to test a scenario where the negative control is thicker and inherently safer than the Janus separator if the PEC layer were to not function properly. Both cell configurations showed stable cycling performance until a shorting event occurs, around the 60^{th} cycle for both separators **(Figure 3.3**a). Before shorting occurs, electrochemical impedance spectroscopy measurements show a negligible difference between the cells with single layer separators and Janus separators (Figure 3.S7, Supporting Information).

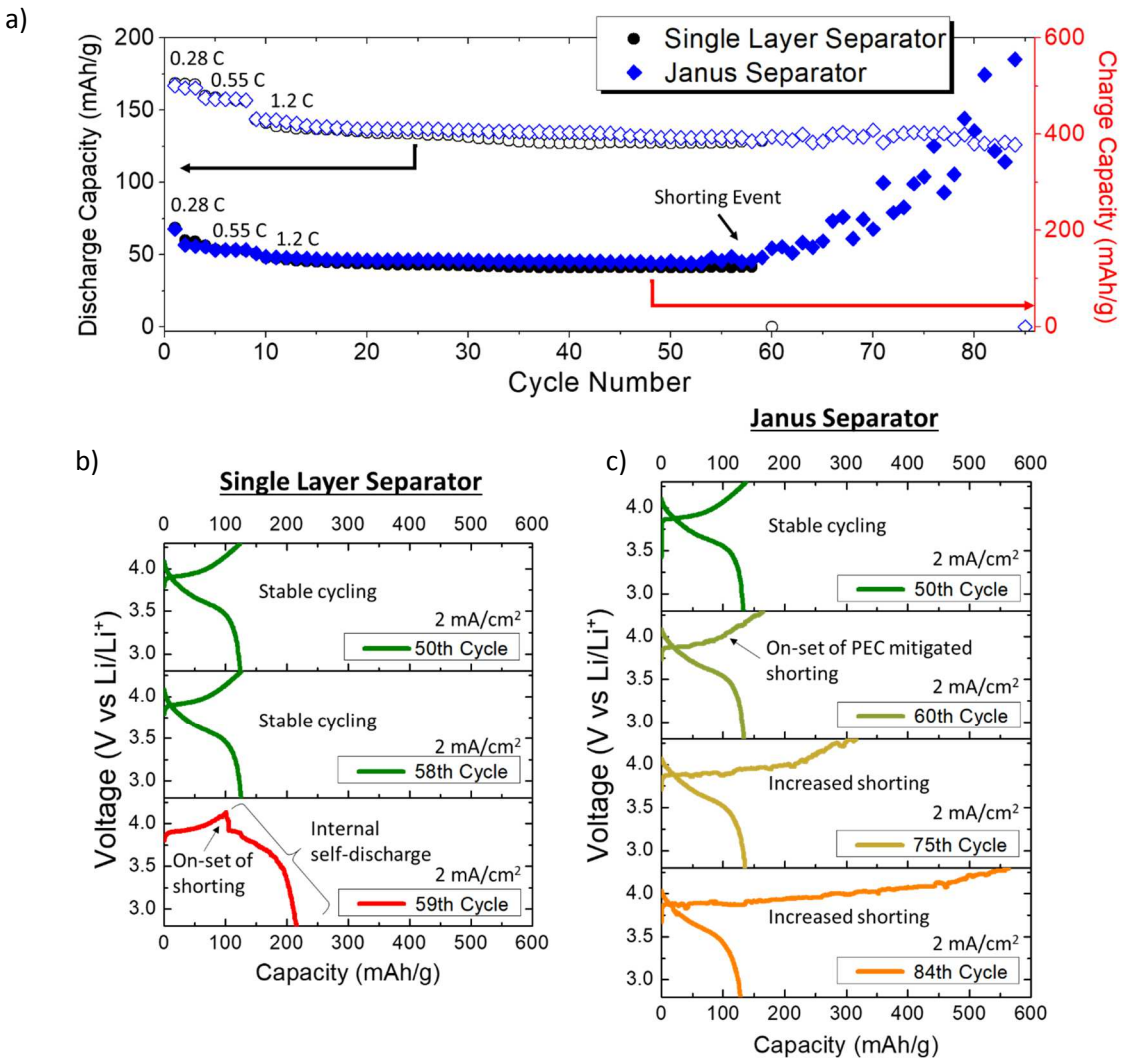

Figure 3.3: a) Charge and discharge capacity profile of galvanostatically cycled Li/NMC532 coin cells with a single layer separator and a Janus separator. b) Selected voltage profiles of the cell with a single layer separator showing stable cycling until sudden on-set of shorting followed by rapid internal self-discharge during the 59th charge. c) Selected voltage profiles of the cell with a Janus separator showing stable cycling until the on-set of PEC mitigated shorting as seen in the 60th cycle. Subsequent cycling after initial shorting results in elongated charge profiles due to increased PEC mitigated shorting and a larger magnitude of self-discharge as seen in the 75th and 84th cycles.

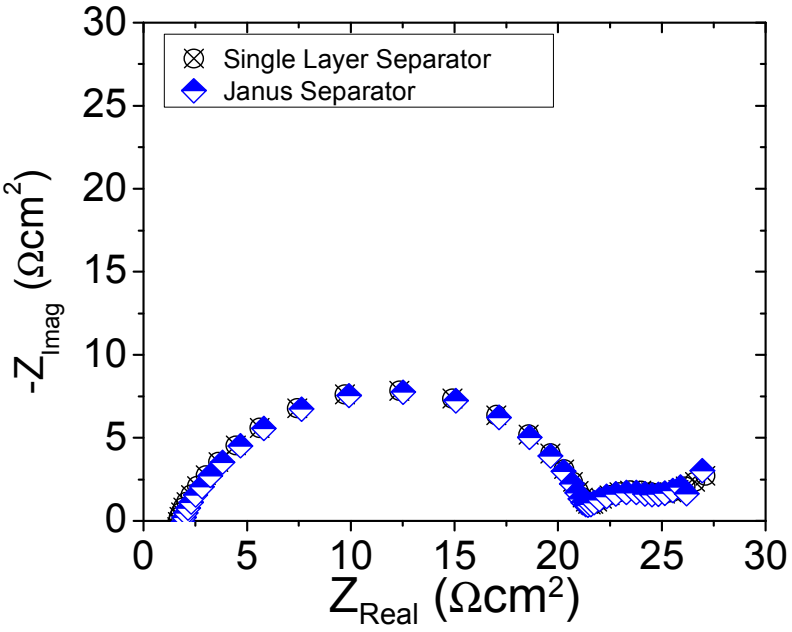

Figure 3.S7: Impedance of the Li/NMC coin cells configuration a single layer separators or a Janus separators before shorting occurred. There is no appreciable difference in the cell impedance between the two configurations. It should be noted that the single layer separator is displayed behind and mostly hidden by the Janus separator data.

Dispite showing similar regular cycling performance and cell coulombic efficiencies (Figure 3.S8, Supporting Information), there is a clear and dramatic difference between the two cells upon shorting. The single laye r separator **(Figure 3.3**b) resulted in a sudden drop of cell potential at the on-set o f shorting during charge in the 59th cycle, indicating internal self-discharge. As expected, the normal separator failed to prevent a low resistance internal short circuit and rapid self-discharge. In contrast, no sudden voltage drop occurs in the cell with a Janus separator and instead a gradual cycle-by-cycle increase of charge capacity appears—as seen in **Figure 3.3**c. After initial stable cycling, the on-set of PEC mitigate shorting occurs sometime around the 60th cycle. This is indicated by the increase of required charge capacity to reach the cut-off voltage,

which generally continues to increase each subsequent cycle. The selected voltage profiles in **Figure 3.3**c show such an increase from the 50th cycle (138 mAh g^{-1}) to the 60th cycle (165 mAh g^{-1}), then to the 75th cycle (317 mAh g^{-1}), and again to the 84th cycle (564 mAh g^{-1}). The increased charge requirement can be explained by the PEC mitigated short circuit allowing internal self - discharge to occur at a rate less than the cell is being charged (*i.e.* < 2 mA cm^{-2}). A recent report employed neutron radiography to directly observe evidence of dendritic Li short-induced self-discharge/charge that results in voltage fluctuation and extended charge time requirement. This is similar to what was seen with the Janus separator, corroborating the competing self-discharge/charge mechanism proposed here.[42] The growing magnitude of internal self-discharge is attributed to increased PEC mitigated shorting as each charge cycle continues to plate additional lithium, increasing the dend ritic short penetration and contact area with the PEC side. This will lower the effective resistance of the PEC side of the Janus separator, thereby increasing the severity of shorting. During the 85th cycle the magnitude of internal shorting and self-discharge rate becomes greater than the rate the cell is being charge (*i.e.* > 2 mA cm^{-2}), voltage declines, and the cell is unable to reach the cut-off voltage (Figure 3.S9, Supporting Information). This multi-cycle failure provides ample time for a battery management system to detect such a shorting event and recommend the battery be replaced. However, despite of this indirect detection of an internal short, it should be noted that the primary purpose of the Janus separator is in fact to mitigate the impact of short and is not necessarily designed as a short detection separator.

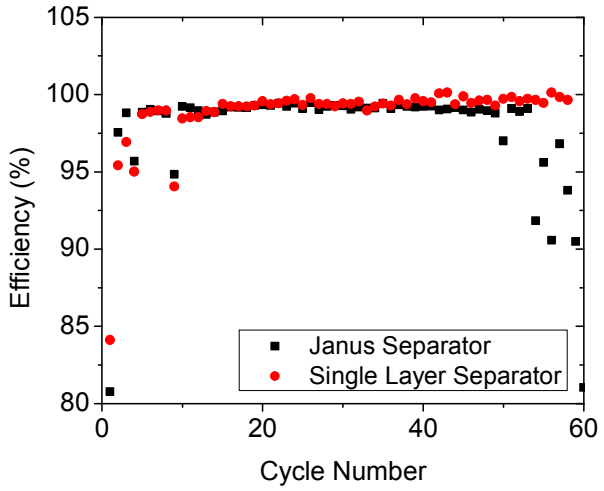

Figure 3.S8: Columbic efficiency data of Li/NMC coin cells with the Janus separator and the single layer separator showing minimal differences between the two cells, until PEC mitigated shorting occurs where calculated efficiency drops due to increased charge requirement.

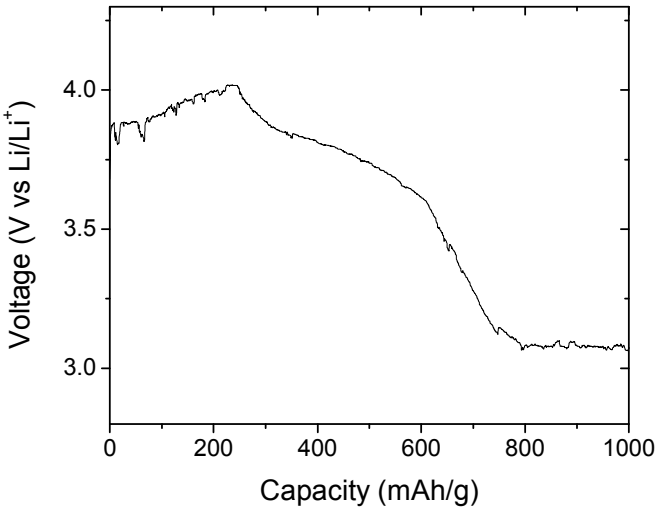

Figure 3.S9: the 85th cycle of the Janus separator coin cell where internal self-discharge rate exceeds the rate the cell is being charged and voltage begins to fall, around 225 mAh g^{-1}

A similar effect can be achieved by coating the PEC layer directly on the cathode (Figure 3.S10, Supporting Information). When cycling tests were repeated with a single layer separator and a ~10 μm PEC coating on the cathode very similar PEC mitigate shorting behavior appears as marked by the increased cycle-by-cycle charge capacity requirement. The PEC layer only needs to intercept the dendrite before fully contacting the cathode and does not necessarily need to be part of the separator. However, the method used to cast the PEC polymer gel electrolyte directly on top of the cathode introduces a mechanical strain, creating cracks in the cathode visible by SEM. This detrimentally effects the capacity of the cell, likely isolating parts of active material. We expect further optimization of the coating process can remedy this issue, opening an alternative route to mitigating internal short circuiting with a PEC material.

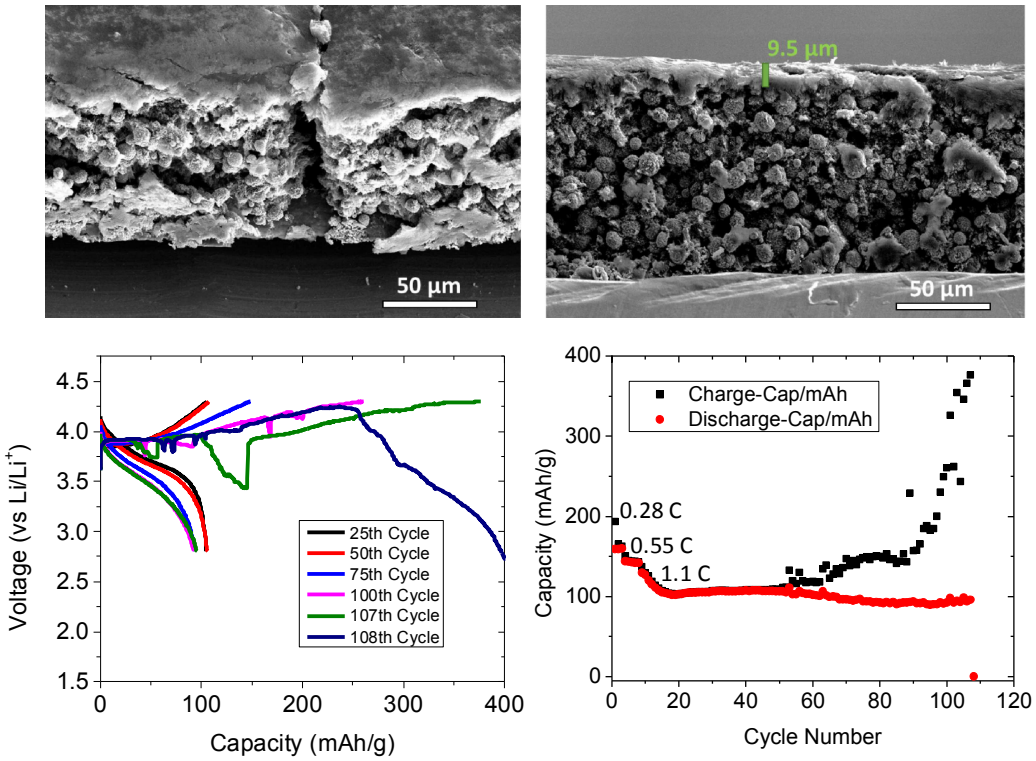

Figure 3.S10: Cross-sectional SEM images, voltage profile and capacity retention for Li/NMC cells where the PEC layer is directly coated on the NMC cathode. The CNT loading is 5 wt% CNTs. A PVDF-HFP:SiO_2/CNTs slurry is casted directly over top of the dry cathode with a channel height set 100 µm above the top surface of the cathode (combined thickness of the current collector and the active material layer).

Commonly used mechanical abuse shorting test such as nail penetration tests or crush tests are poor surrogates to the type of internal shorting that occurs during abusive charging[43] . Considering this, we conducted abusive 4.5 V potentiostatic charging on Li metal/NMC532 pouch cells (active area ~28 cm^2) to induce rapid controllable dendritic shorting as a further proof-of-concept of the Janus separator's ability to mitigate internal shorting. Both the electrical and thermal response of pouch cells containing a single layer separator and a Janus separator were monitored and are shown in **Figure 3.4** a&b. A photograph of the Li metal anode and deposition conditions are found in Figure 3.S11, Supportin g Information. Photographs of the final assembled cells and

thermocouple position are found in Figure 3.S12, Supporting Information. Initial pre-cycling data and impedance measurement of the pouch cells again show no difference in cell performance between the separators (Figure 3.S13, Supporting Information).

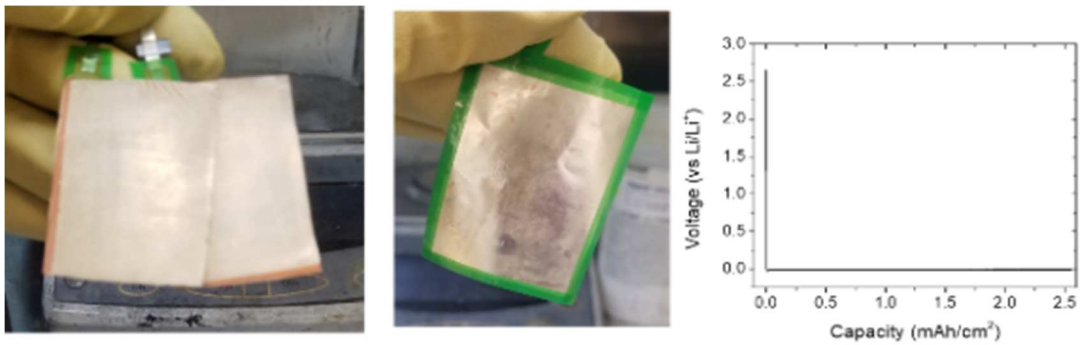

Figure 3.S11: Images of lithium metal anodes deposited (left) and rolled with taped edges (right) to be used in the pouch cells. Also shown is the voltage profile of lithium deposition on copper at 0.1 mA cm^{-2} in 1 M LiTFSI, 0.5 M $LiNO_3$ in 1:1 DOL:DME.

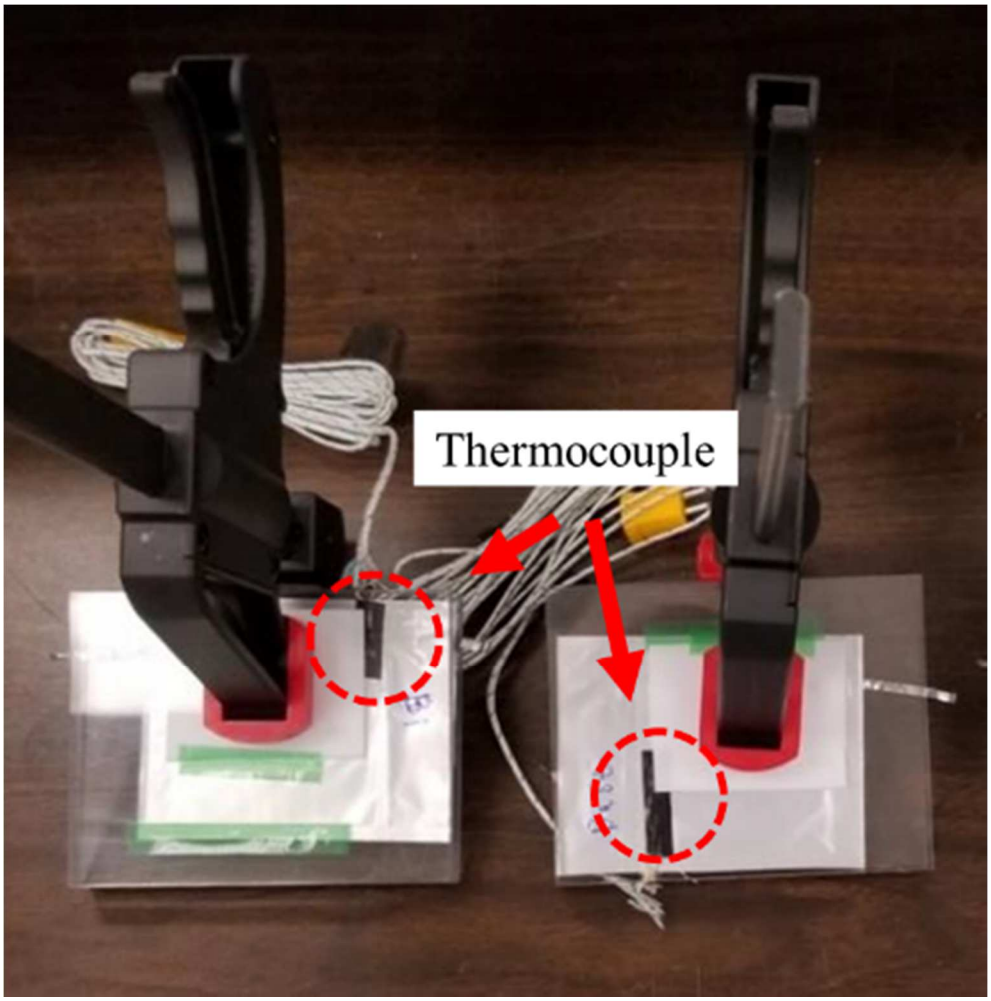

Figure 3.S12: (Top) Picture of a pouch cell with a thermocouple taped to the outer surface near the current collector. The cell dimension is ~ 31 cm^2; (Bottom) The set up for pouch cell testing shown under compression between teflon sheets and teflon plates by hand clamps. Teflon sheets were used to ensure pressure was applied to the active area and gave space for the thermocouple to be taped to the pouch cell. These clamps do not have a pressure gauge, but >100 psi is estimated to be the applied pressure.

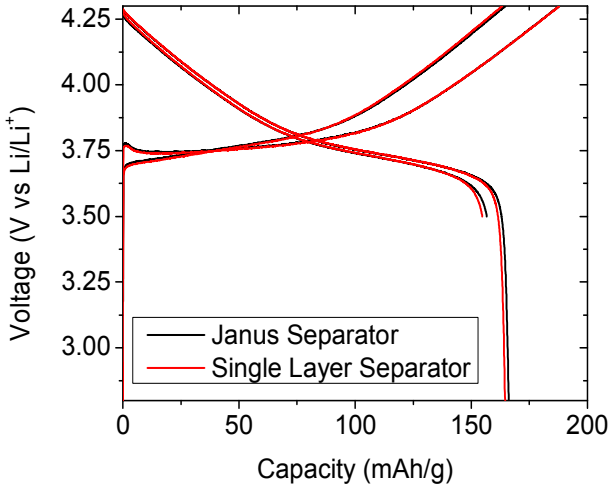

Figure 3.S13: Voltage profiles of the first two cycles of the pouch cells cycled at C/10. The 2nd discharge cut off was set to 3.5 V.

Immediately upon the application of the 4.5 V (vs Li/Li^+) hold, both cells exhibit a brief but large charge current of nearly 1 A or >30 mA cm^{-2}. The current decays down to a diffusion limited regime[44] within 30 seconds; however, this is sufficient to deposit dendritic lithium on the anode surface and shorting occurs at around 250 seconds after the voltage hold is applied. Once shorting occurs, the cell with the single layer separator experiences a short circuit current that reaches nearly 2 A, while the Janus separator cell exhibits almost no rise in current **(Figure 3.4**a). Trailing slightly behind the current, the cell temperature rises in the single layer separator cell by more than 20 °C, whereas the Janus separator cell remains at room temperature **(Figure 3.4**b). It is hypothesized that the ultimate decay in short circuit current in both cells is caused after all available capacity has been exhausted from the cathode; no new Li can be deposited, and the existing dendrites begin to passivate, increasing the electronic resistance of the short circuit.

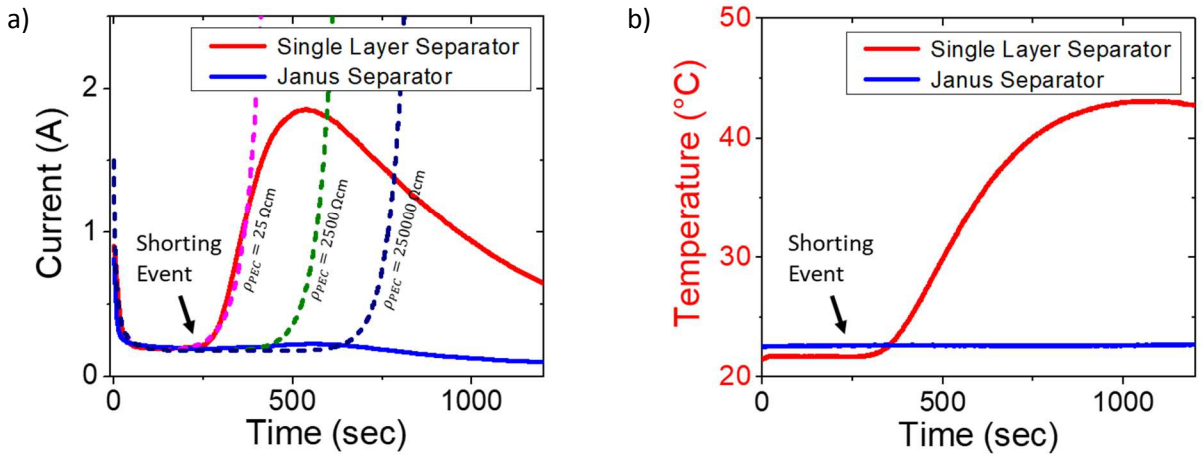

Figure 3.4. Abusive Potentiostatic Charging Induced Short Circuit: a) The current response of Li metal/NMC532 pouch cells with a single layer separator and a Janus separator when a 4.5 V hold was used to charge the cell. Overlaid are modeled current response of cells with a PEC layer with varying electronic resistivity, ρ_{PEC} [Ω cm]. b) Corresponding temperature response measured by a thermocouple located outside of the pouch cell at the negative current collector tab.

To explain the continuous rise in short circuit current and to better quantitatively understand PEC mitigated shorting we developed a simple PEC shorting model, which is seen as the dash overlayer in **Figure 3.4**a. This model attempts to capture how dendritic shorting interacts with the PEC layer of the Janus separator. Normally when dendrites penetrate through the insulating separator, an internal short circuit forms between the anode and the cathode. As charging continues more Li is deposited at the contact point, the short grows more severe, and the resistance—$R_{Short}(t)$—decreases. However, since electrochemical discharge of a battery requires transport of both electrons and Li^+, the total resistance—$R_{Tot}(t)$—that dictates the short circuit current—$I_{SC}(t)$—is the combination of $R_{Short}(t)$ in parallel with internal cell ionic resistance—$R_{Int}(t)$—as shown in the equivalent circuit in **Figure 3.1** and given by **Equation 1**:

$$R_{Tot}(t) = \frac{1}{\frac{1}{R_{Int}(t)} + \frac{1}{R_{Short}(t)}} \quad (1)$$

The resulting shorting circuit current—$I_{sc}(t)$—driven by the electromotive force of the cell—$V_{emf}(Q(t))$—and $R_{Tot}(t)$ is governed by Ohm's Law, **Equation 2:**

$$I_{SC}(t) = \frac{V_{emf}(Q(t))}{R_{Tot}(t)} \quad (2)$$

Large format cells have two primary properties that can drive a large I_{sc}: they have extremely low R_{Int} when considering the entire area of the cell, and will remain at high $V_{emf}(Q(t))$ during self-discharge due to their large capacity, $Q(t)$. When a large format battery shorts across a sufficiently low R_{Short}, these two factors will result in the generation of a significant amount of heat.[45,46]

Introducing the PEC layer can intercept the short and vary the rate at which $R_{Short}(t)$ develops, without affecting $R_{Int}(t)$. With proper tuning of the PEC layer, the short circuit can be controlled, and cell capacity can be slowly and safely drained. To model the effects that tuning the PEC layer has on shorting, the dynamic $R_{Short}(t)$ and resulting $I_{SC}(t)$ of 4.5 V galvanostatic abuse testing were simulated with various PEC layer resistivities—ρ_{PEC} [Ω cm].

Firstly, the transient internal resistance—$R_{Int}(t)$—of the R-RC equivalent circuit described in **Figure 3.1** was estimated by fitting the potentiostatic charging data of the single layer separator cell prior to shorting (0-250 seconds) to **Equation 3** using the Matlab Curve Fitting Toolbox:

$$R_{Tot}(t) = R_{Int}(t) = R_o + (R_{ct} - R_{ct}e^{-\frac{t}{R_{ct}C_p}}) \quad (3)$$

Where R_o is the bulk resistance of the cell, R_{ct} is the charge transfer resistance, and C_p is the electrical double layer capacitance. Fitted values for each parameter are listed in **Table 1**.

Secondly, the fitted $R_{Int}(t)$ was inputted into **Equation 1** and the remaining transient short circuit resistance, $R_{Short}(t)$, was estimated from the same potentiostatic charging data, however, now by fitting over the entire time prior to peak short circuit current (0-550 seconds). Resistivity of the PEC layer and the electrode, as well as the dendrite growth rate and penetration depth are considered when estimating the short circuit resistance as calculated by **Equation 4**:

$$R_{Short}(t) \approx \rho_{PEC} * \alpha e^{-\gamma(t-t_{SC})} \quad (4)$$

The dendrites are modeled as growing rods penetrating a PEC layer with a certain resistivity, ρ_{PEC} [Ω cm^2 cm^{-1} or Ω cm]. Here, α [cm cm^{-2} or cm^{-1}] represents the ratio of rod penetration depth [cm] to the contact area [cm^2] between the rod and the PEC layer. The exponential function containing γ [s^{-1}] represents the dendrite growth rate, encompassing both increasing penetration depth and growing contact area after the onset of shorting at $t = t_{SC}$ (250 seconds). These values were also estimated using the Matlab Curve Fitting Toolbox and are listed in **Table 1**. It should be noted that this model allows $R_{Short}(t)$ to approach zero and does not capture the current decay seen at the end.

Table 3.S3. Fitted parameters to describe potentiostatic charging induced

R_o [Ω]	R_{ct} [Ω]	C_p [F]	α [cm cm^{-2}]	γ [s^{-1}]
3	22.5	1.882	30.17	0.02297

Lastly, simulations of the short circuit current response of cells during 4.5 V potentiostatic charging and shorting are performed using these fitted parameters with different ρ_{PEC} values. The results for the single layer separator ($\rho = 25$ Ω cm, representing the resistivity of cathode alone with no additional PEC layer)[47], and with a PEC layer of $\rho_{PEC} = 2500$ Ω cm and 250000 Ω cm are overlaid in **Figure 3.4**a. Simply enough, the higher the PEC resistivity, the more prolonged the onset of shorting. This allows enough time for the charge capacity to be exhausted and the short to passivate.

As further confirmation of the PEC mitigated shorting mechanism the pouch cells were disassemble and inspected. Both separators have a large amount of dendritic lithium embedded in the anode-facing surface, which was delaminated from the Li anode during disassembly (Figure 3.S14, Supporting Information). However, there is a clear difference visible between the cathode-facing surface of the two separators after shorting: by eye, the Janus separator maintains a black PEC surface similar to the pristine state while there is visible dendrite penetration through the single layer separator. SEM shows a dendrite free PEC surface whereas the single layer separator surface is covered with cracks and lithium penetrating through those cracks (Figure 3.S15, Supporting Information).

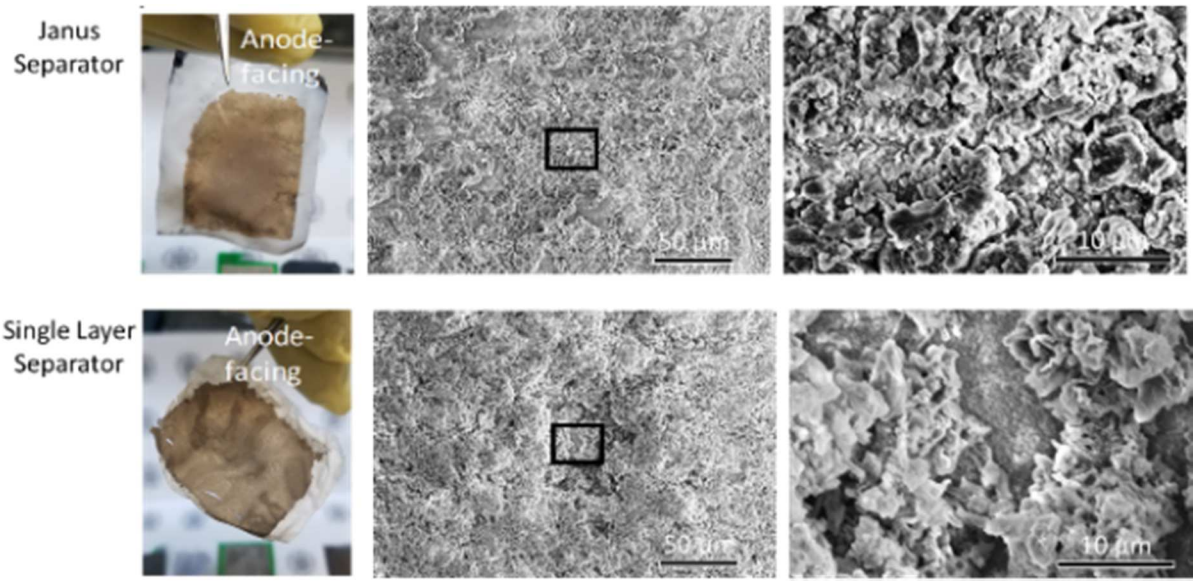

Figure 3.S14: Postmortem optical and SEM images after pouch cell abuse charging of the anode-facing surface of the Janus separator (top) and the anode-facing surface of the single layer separator (bottom). Both show large amounts of dendritic Li embedded into the separator.

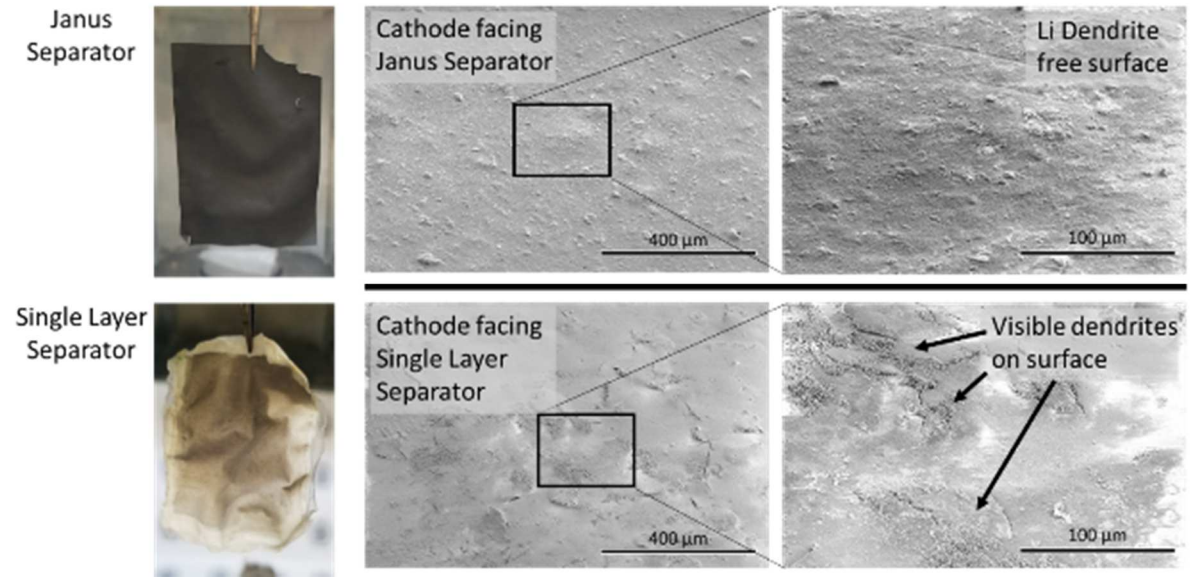

Figure 3.S15: Post mortem optical and SEM images after pouch cell abuse charging of the cathode-facing surface of the Janus separator (top) and the cathode-facing surface of the single layer separator (bottom). The Janus separator maintains a Li free black surface, while the single layer separator has Li penetrating through the separator and is visible on the surface. Adobe Lightroom was used to adjust contrast in SEM figures, particularly due to charging of insulating materials causing bright spots in the image.

Additional SEM and EDS elemental mapping was performed on cross sections of both separators (**Figure 3.5**). In **Figure** 5a, the dendrite c an be seen penetrating through the electronically insulting side of the Janus separator but is then intercepted by the PEC layer. Elemental mapping of O—corresponding to oxidized Li—and F—present in the PVdF-HFP separator—further highlights the dendrite interception **(Figure 3.5**b and Figure 3.S16). Additional cross-sectional SEM along the Janus separator show multiple locations where dendrites were intercepted by the PEC layer and can be found in Figure 3.S17, Supporting Information. Referring again to the tensile test results (Figure 3.S2), it is highly unlikely that the PEC side possess enough additional tensile strength to mechanically suppress dendrites, and the observed dendrite interception at the interface is solely due to the PEC mitigated shorting mechanism. Conversely, the dendrite is observed to have fully penetrated the single layer separator in **Figure 3.5**c&d, resulting in the low resistance internal short circuit and the current response seen during abusive charging.

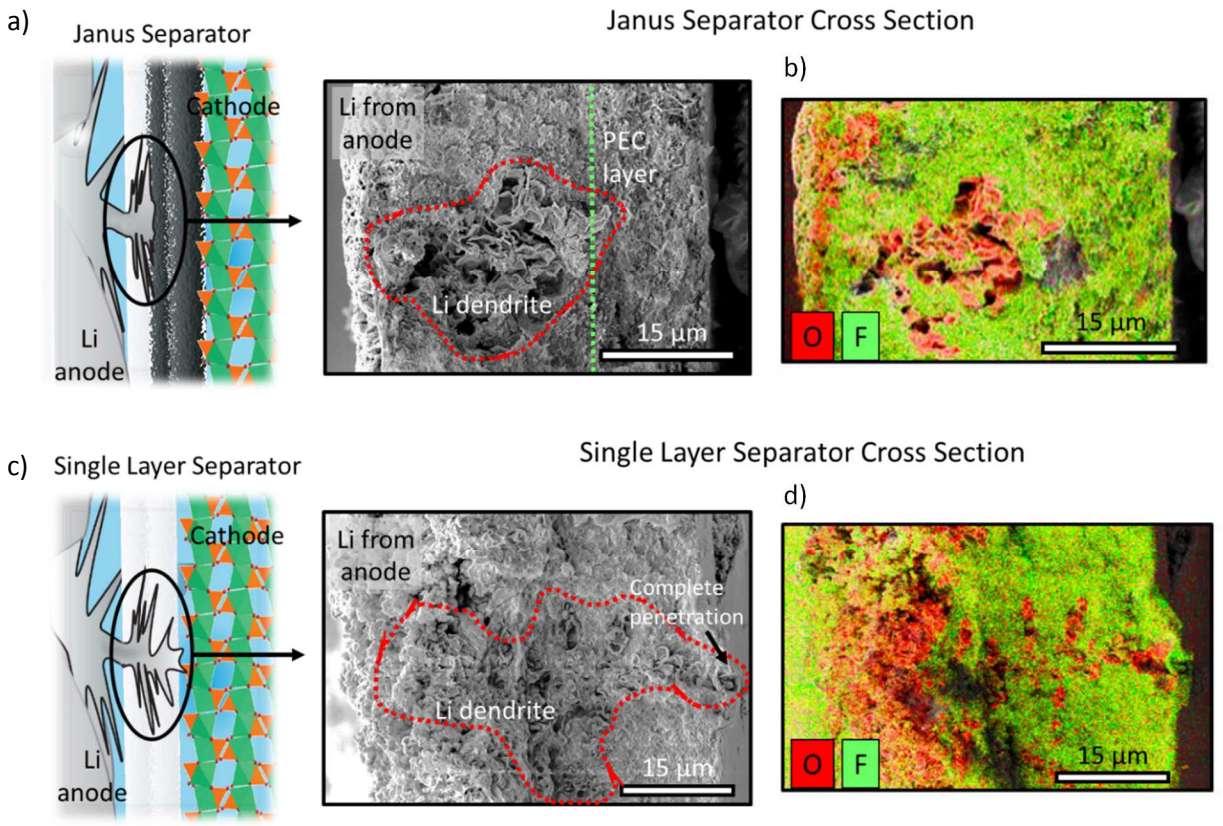

Figure 3.5: Postmortem scanning electron microscopy of the a) Janus separator and the c) single layer separator. Energy-dispersive X-ray spectroscopy of separator cross sections of the b) Janus separator and the d) single layer separator.

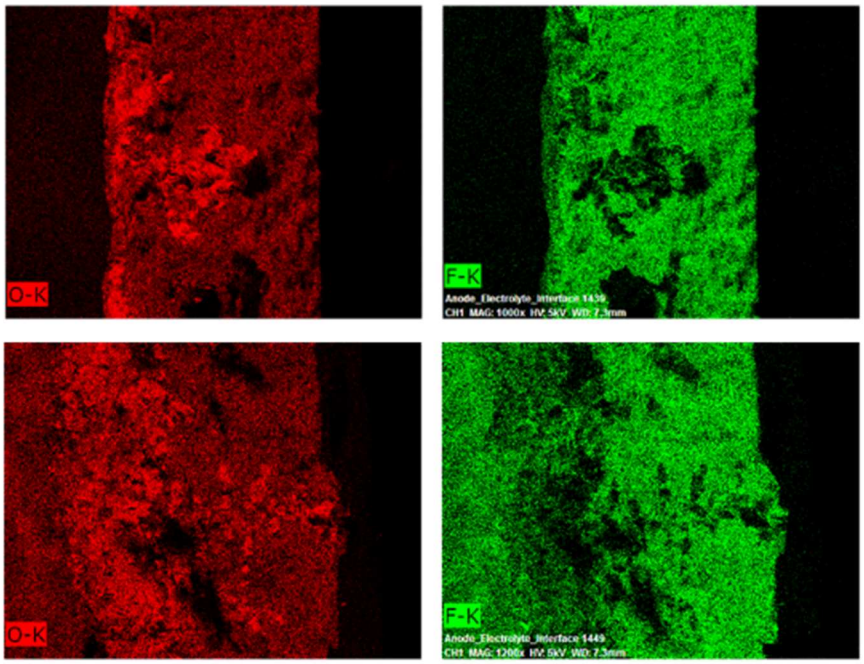

Figure 3.S16: Additional EDS elemental mapping showing the individual O and F signal of the post mortem cross sections of the Janus separator (top) and the single layer separator (bottom). Adobe Lightroom was to increase the color contrast of the reds and greens in EDS images, however no additional signal was added.

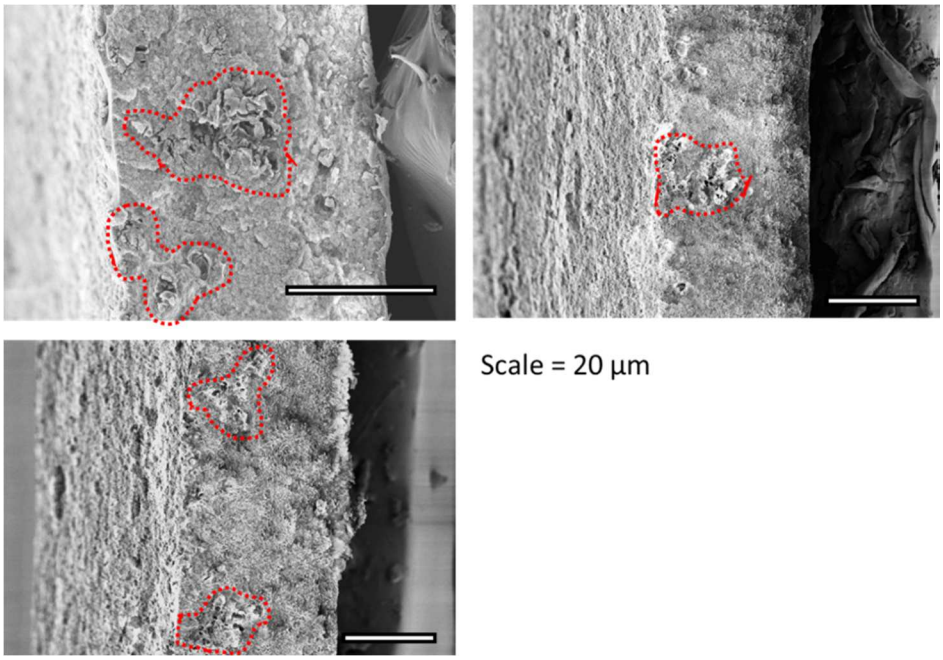

Figure 3.S17: Additional postmortem cross section images of the Janus separator showing dendrite interception by the PEC layer at multiple locations throughout the separator.

In conclusion, we have designed and developed a Janus separator with one side being a partially electronically conductive (PEC) nano-composite layer that has the ability to dramatically reduce short circuit current when an internal shorting incident occurs from Li dendrite growth. The separator, < 35 µm-thick, is fabricated by coating a PEC layer directly on an electronically insulating separator. Various electrochemical shorting tests show that the Janus separator was indeed effective in controlling and raising the resistance of the internal short circuit, thus reducing self-discharge current when compared to cells with a single layer electronically insulting separator. Galvanostatic cycling tests resulted in a gradual failure mechanism in coin cells containing the Janus separator compared to the sudden failure of the single layer separators. During abusive potentiostatic charging, pouch cells assembled with the Janus separator showed little to no rise in

current and tem perature during shorting, whereas cells with conventional separators experienced large increase in current and more than 20 °C rise in external cell surface temperature, which could easily lead to safety incidents in larger cells.

The Janus separator presents a new approach to mitigating the impact of internal shorting. Instead of blocking the dendritic short circuit, the PEC layer allows the short circuit to occur, albeit in a much gentler and safer fashion. While the current iteration of the Janus separator remains a proof-of-concept, a similar Janus design can be applied to commercial separators (e.g. Celgard) although material and process optimization will be needed to address any differences in shorting dynamics due to the different mechanical and chemical properties of the baseline separator. The design is also expected to be effective in lithium-ion batteries where internal short circuits develop due to mechanical compression or conductive filament growth caused by manufacturing defects or overcharging. As a result, the design could find quick adoption in current battery technologies and facilitate the advancement of emerging battery technologies of higher energy density. Our work illustrates the potential of a new, generally applicable safety design mechanism that addresses the impact of internal short circuit.

Experimental Section

Separator Fabrication and Characterization: Kynar Flex® 2801 PVDF-HFP co-polymer powder (Arkema), fumed silica powder (SiO_2, Sigma-Aldrich) were combined in a 3:2 ratio. Multi-walled carbon nanotubes (CNTs) with an average length of 5 μm (purchased from SWENT and used without further modification) were predispersed in acetone by ultra-sonication. The amount of CNTs dispersed is determined by the desired wt% of CNTs in PVDF-HFP/SiO_2. In a

typical process, 1 g of PVDF-HFP/SiO_2 mixture was then added to 10 mL of acetone/CNT dispersion and 2 mL of dibutyl phthalate (DBP). To ensure homogeneity the slurry was mixed by stirring at 60 °C for two days in a sealed container. Finally, the slurry was mixed by an orbital mixer until the polymer was completely dissolved and the CNTs were fully incorporated. The solution was then cast using a doctor blade to form either a freestanding PEC separator, or a coating on a dry 0 wt% separator to form the Janus separator. The porosity was achieved by extracting the DBP plasticizer with diethyl ether based on the methods described in the *Gozdz* et *al.* patent.[34]

To measure the electronic conductivity of the PVDF-HFP:SiO_2:CNTs freestanding PEC separators, they were placed between two stainless steel electrodes in a spring loaded Swagelok cell. A voltage bias of 100 mV was applied between the electrodes. Conductivities were calculated from the current and the sample thicknesses estimated from SEM images (Figure 3.S1, Supporting Information)

Battery Fabrication and Testing Parameters: An 80:10:10 slurry of NMC($LiNi_{0.5}Mn_{0.2}Co_{0.3}O_2$):SuperP carbon:PVDF in N-Methyl-2-pyrrolidone (NMP) was blade coated on Al foil. After drying and calendaring, the electrodes had a thickness of roughly 100 μm with an areal capacity of approximately 1.8 mAh cm^{-2} for coin cells cathodes. A cathode with high capacity of 2.5 mAh cm^{-2} that consists NMC, CNT, and PVDF in a mass ratio of 100:1:1.5 on Al foil (Hunan Hong Xiang New Energy Technology CO.LTD) was used for pouch cell fabrication.

Coin cells were assembled with 2032 stainless steel casings and used 13 mm diameter cathodes paired with a 15 mm diameter Li disk rolled onto a 1 mm thick stainless steel spacer disk. 1.0 M $LiPF_6$ in 1:1 vol/vol ethylene carbonate (EC) and dimethyl carbonate (DMC) (LP30, Gotion) was used as the electrolyte. The cell was sealed in a hydraulic crimper at 1000 psi.

Pouch cells used a lithium anode with a capacity of 2.5 mAh cm^{-2} which was prepared by electroplating lithium on copper foil at 0.1 mAh cm^{-2} in 1 M LiTFSI (Lithium bis(trifluoromethanesulfonyl)imide), 0.5 M $LiNO_3$ in 1:1 wt/wt DOL:DME (1,3-dioxolane : 1,2-dimethoxyethane) using a thick Li source. This electrode was hand rolled smooth and the bare Cu edges were taped (Figure 3.S8, Supporting Information). The laminated pouch cell was sealed using a MTI MSK-115A-S vacuum sealer in an argon filled glove box after the electrolyte was added.

Pouch cells were placed between Teflon sheets and plexiglass plates (Figure 3.S9, Supporting Information). The thermocouples were taped on the outside of the pouch above the negative contact, but between the plexiglass where the smaller Teflon sheet allowed space as to apply pressure only to the active cell area and not to the tip of the thermocouple. A hand clamp was used to apply pressure to improve cycling of the Li metal anodes. This set up does not allow measurement of the pressure applied, however the clamps were tightened to their maximum by hand and pressure is estimated to be >100 psi (Figure 3.S9, Supporting Information).

Coin cells were cycled using a Landt battery tester at 0.5 mA cm^{-2} for three cycles, 1.0 mA cm^{-2} for five cycles, and 2.0 mA cm^{-2} until failure. Coin cells and pouch cells used in the potentiostatic tests were precycled at 0.2 mA cm^{-2} for two cycles (2^{nd} cycle cut-off was set to 3.5 V). Potentiostatic holds and impedance measurements were carried with a Biologic potentiostat using a high current (10 A, 5V) booster channel. Temperature was measured using a K-type thermocouple and HOBOware reader.

Acknowledgements:

The majority of cell fabrication and electrochemical testing was performed in the UCSD-MTI Battery Fabrication and the UCSD-Arbin Battery Testing Facility. We acknowledge

Zhaoqiang Song and Shengqiang Cai in the UCSD Mechanical and Aerospace Egineering for assistance with mechanical testing. We acknowledge Hunan Hong Xiang New Energy Technology CO.LTD for supplying high capacity NMC cathode tapes. P.L. proposed the idea and directed the research along with H.L. All of the authors contributed to the planning, materials fabrication, experimental design and analysis, and manuscript preparation. M.S.G. performed the majority of separator fabrication and characterization as well as cell fabrication, electrochemical testing, and model development. J.Y. and Z.W. assisted with full cell experimental design and cathode fabrication. H.Z. and N.P. aided M.S.G. in separator characterization and model development. V.P. provided insights in composing the manuscript and data organization.

Chapter 3, in full, is a reprint of the material as it appears in Advanced Materials 2020, 32. M. S. Gonzalez, Q. Yan, J. Holoubek, Z. Wu, H. Zhou, N. Patterson, V. Petrova, H. Liu, P. Liu. The dissertation author was the primary investigator and author of this paper.

Chapter 4: Simplifying Safety With Etched Gradient-Conductivity Cathodes

In response to the need of portable electronics and electric vehicles, the energy densities of lithium-ion batteries have continued to rise. In the near term, reduction of inactive materials has proven to be successful. The thickness of commercial battery separators has been reduced to <10 μm,[1] while electrode areal specific capacity [mAh/cm^2] continue to rise.[2] In the long-term, the graphite anode will be replaced by higher capacity electrode materials, namely silicon containing materials[3] and ultimately lithium metal.[4]

These changes in design and materials make battery safety an increasingly difficult challenge.[5] For LIBs, it is well known that mechanical deformation[6] and overcharging[7] can induce internal shorting and dangerous thermal runaway. However, this can also occur without discernable external cause while operating under normal conditions.[8],[9] The suspected cause of these type of events is a failure of the separator creating a low *electronic resistance* internal short circuit within the battery.[10] The challenge of separator failure further increases with the use of lithium metal anodes, especially during rapid charging when the likelihood of Li dendrite penetration increases.[11]

Approaches to improve battery safety generally add a protective element within the battery to block, drain, or cut off the short circuit. Battery separators play an essential role in this function. The addition of various porous polymer layers,[12] non-woven mats,[13] or ceramic coatings[14] have shown improvement of mechanical properties over standard polyolefin separators and aid to physically block dendrite propagation. All ceramic solid ion conductors acting as both separator and electrolyte can also suppress dendritic growth.[15] Materials can be added within the separator that are reactive towards Li and serve to etch away oncoming dendrites, but are limited by the material capacity past which dendrite propagation begins again.[16] Similarly, third electrodes

sandwiched in the separator have been implemented to detect dendrite penetration and diagnose the health of the cell.[17] Most commonly battery separators are designed with an additional layer of porous material that undergoes a phase transformation and pore collapse at elevated temperature to cut off the ionic pathway and suspend shorting—ideally accomplished before thermal runaway initiates.[18]

Another approach beyond modifying the separator is to break the electronic pathways within the electrodes themselves to limit the impact of shorting. Several methods have been developed to electronically isolate the active material. Current collectors have been designed to fracture upon mechanical deformation limiting self-discharge to small, isolated regions.[19] Positive thermal coefficient (PTC) materials have also been coated on the current collector or on the cathode itself to insulate the active material from the current collector or each other upon reaching elevated temperatures.[20],[21],[22] Unlike these temperature-trigged methods, we have recently introduced a partially electronically conductive (PEC) Janus separator to intercept oncoming dendrites. The PEC layer, in contact with the cathode, is permeable to lithium ions but adds electronic resistance to the short circuit formed when a dendrite makes contact, thus limiting the internal short circuiting current and the temperature rise, rendering the short practically harmless.[23]

All of these protection schemes, whether separator or electrode based, involve adding a component to the battery which invariably incurs increased manufacturing costs, adds to the overall volume, and increases the electronic or ionic resistance of the battery. In order for a protection scheme to be not only effective, but also economically scalable, it should ideally utilize the intrinsic properties of the electrode materials and architecture without incurring penalties in cell volume, weight, or resistance.

Here we introduce a method to achieve increased electronic resistance for a short circuit by using a cathode material with a gradient electronic conductivity. Specifically, a reduced electronic conductive (REC) layer is created in the top layer of the cathode facing the separator side. In a common cathode (Figure 4.1b), the active material, usually a metal oxide, is mixed with carbon to increase the electronic conductivity and held together by a polymer binder. If a dendrite contacts the conductive carbon network then the entire cathode is effectively shorted to the anode which can result in rapid self-discharge, Joule heating, and thermal runaway. In contrast, **Figure 4.1a** shows a schematic of the REC interlayer, where the cathode's conductive carbon network has been selectively etched away from the cathode surface. When a dendrite shorts the anode and cathode, the short circuit must travel through the layer of the carbon-free active material. Common transition metal oxides cathode materials have low electronic conductivity (10^{-3} – 10^{-8} S/m),[24],[25],[26] and is the very reason conductive carbon is required to achieve good cycling performance at even low C-rates.[27] In the absence of carbon, however, the active material acts as a convenient high resistance short circuit intercept. Additionally, since the etching is limited to the cathode surface, the bulk of cathode remains electronically connected, which should allow for unaltered cycling performance outside of a failure event.

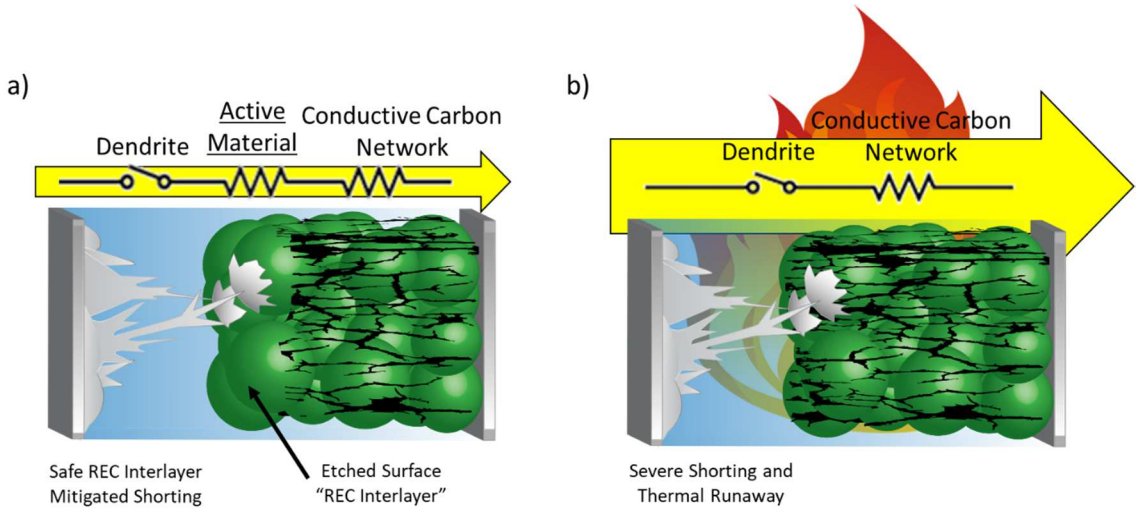

Figure 4.1: Working mechanism of internal short mitigation with a gradient conductivity cathode. **a)** schematic of an etched cathode where the surface carbon is removed and the active material adds an additional resistive element to the short circuit when a dendrite shorts the anode to the cathode. **b)** Schematic of an unetched pristine cathode where the conductive carbon and dendrite generates a low resistance short circuit and possible thermal runaway events.

To selectively etch the surface of the cathode a simple sputter etching technique was employed to remove the carbon species (conductive carbon and polymer binder) from the surface of the cathode without damaging the active material. By reversing the polarity in a laboratory sputtering deposition system, Ar^+ was generated to bombard the cathode and strip away surface materials. The cathodes used are high energy density commercial quality electrode tapes roughly 50 µm thick on Al foil. The active material is $Li_xNi_{0.5}Mn_{0.3}Ni_{0.2}O_2$ (NMC), with PVDF as the binder, and MWCNTs as the conductive carbon network in a weight ratio of 97.5 : 1.5 : 1. **Figure 4.2** shows optical and high magnification SEM images of cathode surfaces that underwent **a)** 30-minute, **b)** 10-minute, and **c)** 5-minute etching as well as a **d)** 0-minute (pristine) electrode. While there is no obvious difference to the naked eye, SEM shows 30-, 10- and 5-minute etching results

in a smooth and carbon free NMC surface, while the pristine cathode has a clear mat of MWCNTS coating the surface giving it a fuzzy appearance.

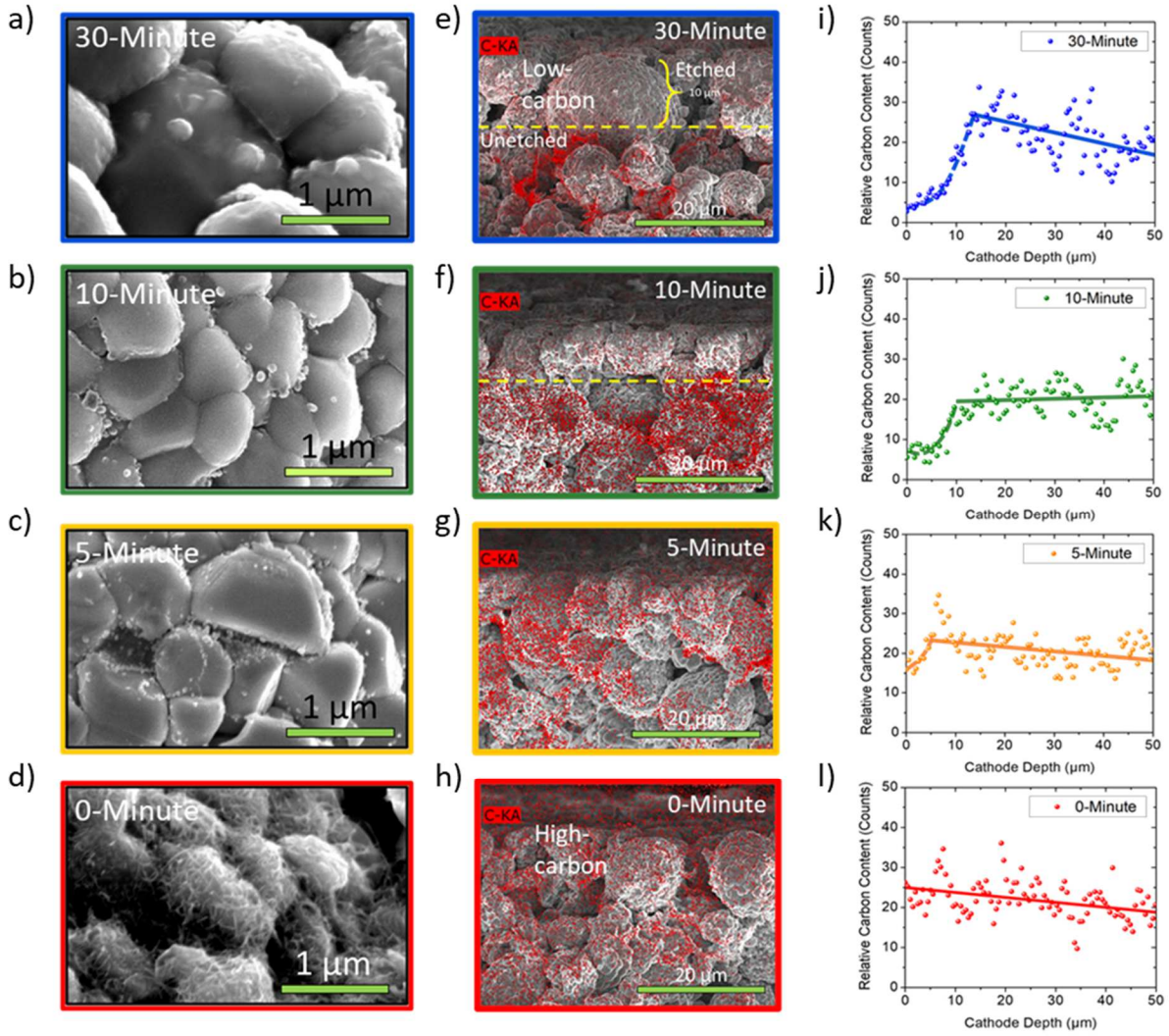

Figure 4.2: Characterization of the conductivity gradient cathodes. Optical and high magnification SEM images of the cathode surface after etching for **a)** 30-minute, **b)** 10-minute, **c)** 5-minute, and **d)** 0-minute. Cross-section SEM titled by 5° focusing on the cathode surface and roughly 20 µm depth with EDS elemental mapping overlay of carbon element for cathodes etched for **e)** 30-minute, **f)** 10-minute, **g)** 5-minute, and the **h)** pristine (0-min) cathode. **i)** The average relative carbon content collected by EDS line scan as a function of cathode depth for each etching time.

Cross-sectional SEM images with EDS elemental mapping of carbon overlayed for electrodes after 30-minute **(Figure 4.2e)** and 10-minute etching **(Figure 4.2f)** show that carbon has been removed from a depth of roughly 10 μm into the cathode surface. Higher magnification SEM focusing a surface particle shows etching removes carbon from only the upper hemisphere of the particle where the lower hemisphere is shaded due to the line-of-sight nature of the sputter etching process (Supporting Information, Figure S1). The 5-minute etching **(Figure 4.2g)**, while sufficient to remove surface carbon, does not appear to penetrate meaningfully into the cathode. The pristine cathode has carbon extending uniformly throughout the cathode including the surface **(Figure 4.2h)**. EDS line scans detecting C were performed at 20 individual cross-section locations along each cathode sample, these were averaged, fitted, and plotted in **Figure 2i**. The 30- and 10-minute etched cathodes again show little relative C signal until a depth of 10 μm where there is significant increase in C content. The C signal intensity plateaus at 4-5x the relative content detected on the surface and remains constant throughout the bulk. The 0-minute (pristine) cathode shows the same relative carbon content that is constant from surface to bottom of the cath ode, while the 5-minute etching shows some removal of surface carbon but fails to penetrate past a depth of < 5 μm. The overall slight downward trend in carbon content through the cathode depth is attributed to a blocking effect decreasing the amount of signal that reaches the EDS detector, and we expect the carbon is most likely constant throughout.

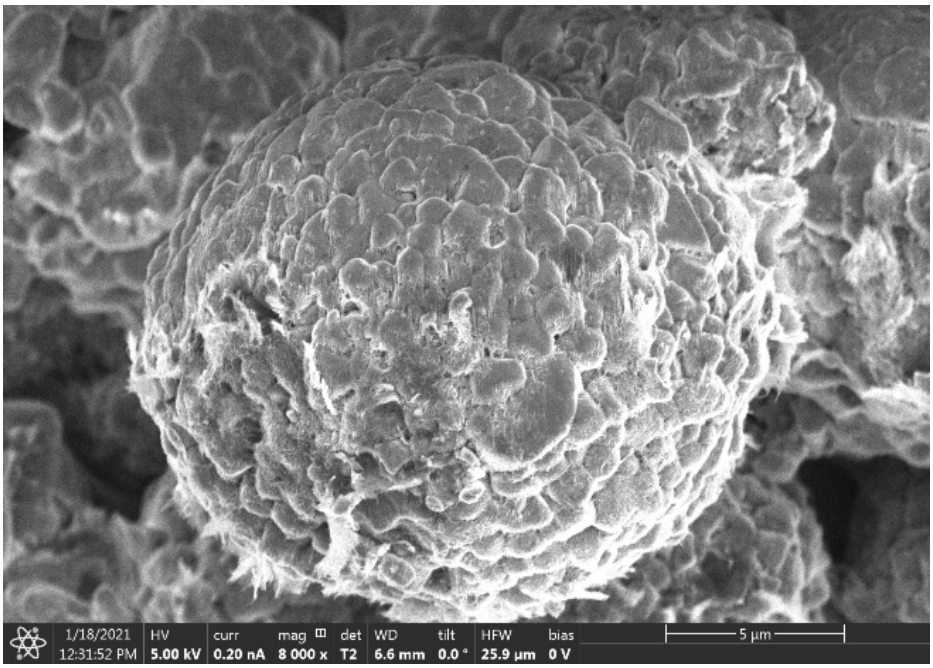

Figure 4.S1: SEM focused on a single 30-minute etched secondary NMC particle showing the etching effect extends only on the exposed upper hemisphere of the particle.

The change in the electronic conductivity due to removing the surface conductive carbon network was measured to correlate etching time with the expected increase in electronic resistance upon an internal short. The resistance measurement was conducted using four parallel copper stripes placed on freestanding sheets of various etched and unetched cathodes. We use the resistance for a given area (Ωcm^2) of the cathode to characterize the impact of etching and the results are summarized in **Table 1**. Note that after etching, the electrode is composed of the REC layer under which is the more conducting, pristine layer. The in-plane resistance is thus very sensitive to the REC layer thickness. Details of resistance calculation are provided in Supporting Information, Figure 4.S2. A continuous increase in resistance is observed as the etching time increases, from 45.1 Ωcm^2 for the 0-minute etched to 203.5 Ωcm^2 for the 30- half of the increase

over the 0-minute etched sample using the in-plane method and was calculated to be 6.8 Ωcm^2, 65.5 Ωcm^2, and 79.2 Ωcm^2 for the 5-minute, 10-minute, and 30-minute etched cathodes, respectively. Note that these are increases of electronic resistance for dry electrodes. As shown below, the battery performance under normal operating conditions is largely unaltered.

Table 4.1: Electrical area specific resistance of 0-minute, 5-minute, 10-minute, and 30-minute etched freestanding cathode tapes, the active material with no conductive carbon, and the active material with no conductive carbon after being overlithiated by direct contact with Li metal.

	Cathode Resistance (Ωcm^2)	Conductivity (S/m)
0-Minute Etched	45.1	3.05×10^{0}
5-Minute Etched	58.6	n/a
10-Minute Etched	176.0	n/a
30-Minute Etched	203.5	n/a
Carbon-Free	6.53×10^{3}	1.63×10^{-5}
Overlithated Carbon-Free	n/a	1.26×10^{-4}

Additionally, a completely carbon-free cathode was also casted with only NMC and PVDF binder (97.5 : 2.5 wt%) to measure the conductivity of the NMC particles themselves. The resistance of this was determined to be 6.53×10^{3} Ωcm^2, and the conductivity σ was calculated to be 1.63×10^{-5} S/m. This is a very large increase over 3.05×10^{0} S/m measured for the pristine cathode tape containing carbon and highlights the need to incorporate a conductive network between the active materials. Furthermore, this carbon-free tape was lithiated by directly contact with Li metal to simulate the chemical state the NMC would be in at the immediate area of Li dendrite contac minute etched cathode tape. The added through plane resistance from etching is

approximately 158.4 ohmcm^2. This overlithiated state has a higher conductivity than the pristine carbon-free NMC, 1.26 x 10^{-4} S/m but is still orders of magnitude lower than that of the normal pristine cathode added with carbon. It is expected that the contact area in immediate contact with Li metal will be reduced to 0 V by the dendrite. *Benedek, et. al.*[28] proposed that $LiMO_2$ materials (where M is a transition metal) undergo a multi-step reduction upon overlithiation that ultimately result in the formation of a physical mixture of M^0 and Li_2O via a conversion reaction mechanism. The reaction resulted in a nearly 4-5x increase in cathode thickness (Supporting Information, Figure 4.S3). The observed higher electronic conductivity in this state compared to the unreacted carbon free tape is likely due to the reduction of the Ni, Mn, and Co to a fully metallic state; however, the other nonconductive product of Li_2O keeps the overall bulk conductivity several orders of magnitude lower than that of the conductive carbon network and should still provide sufficient ele ctronic resistance in the event of a short.

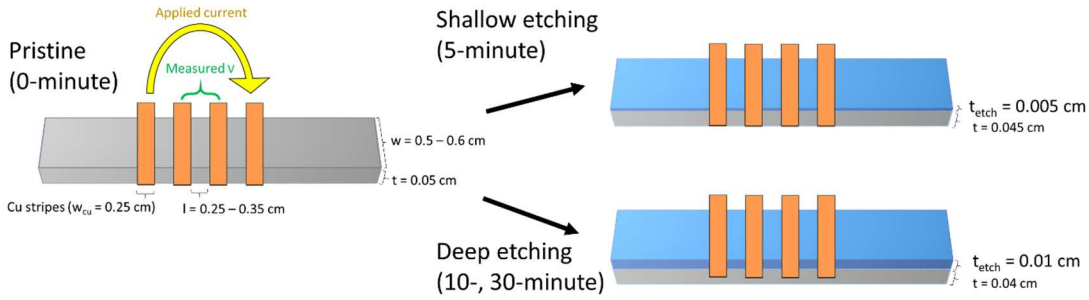

Figure 4.S2: Diagram of the cathode resistance measurement showing the general dimensions of the test. Cathode resistance for the given test area (Ωcm^2) were calculated using Cu stripes on the surface of a freestanding cathode tape. By applying a current between the outer Cu stripes and measure the voltage difference between the inner Cu stripes a resistance can be calculated. This is then normalized by the Cu strip contact area to yield an areal resistance (Ωcm^2). Current is expected to flow primarily through the more conductive unetched layer and to a much less extent through the more resistive top layer. The resistance increase measured in the etched cathodes is due to an increase in the thickness of the non-conductive layer (t_{etch}) as the current must take an increasingly longer route through this layer as etching depth increases. Since etched layer is effectively measured twice, once when current is injected into the cathode and once when it exits, the added through plane resistance was estimated as approximately half of the increase in resistance over the 0-minute (pristine) sample. Cathode conductivity was calculated by now considering the thickness of the cathode tape; however, the etched cathodes are inhomogeneous in composition therefore values were not reported.

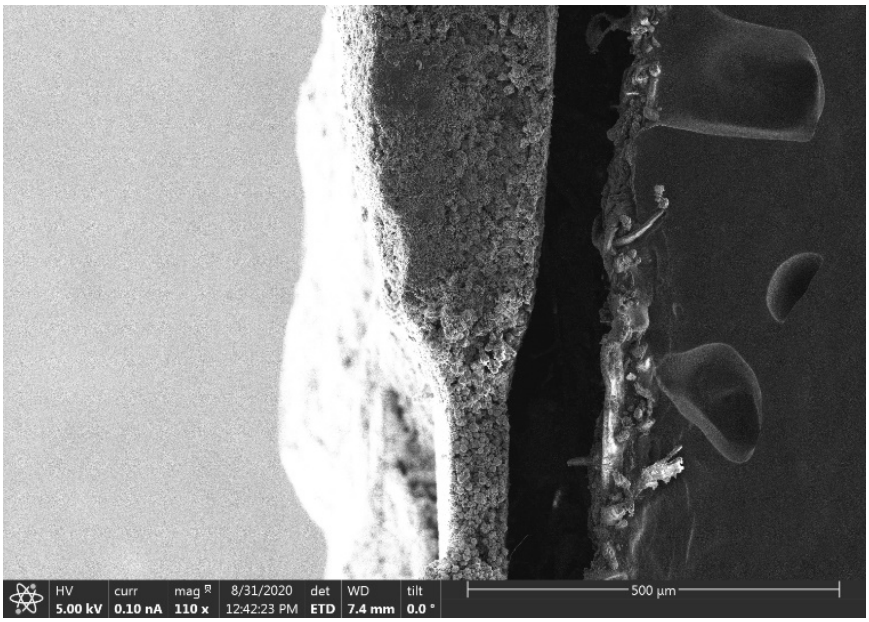

Figure 4.S3: SEM images of an NMC showing the area in direct contact with Li metal. The overlithiated state shows roughly a 4-5x increase in thickness.

SEM investigation of pristine and NMC secondary particles that have been overlithiated by direct contact with Li metal for 24 hours show a clear volume expansion that pulverizes the secondary particles and cracks the primary particles (Supporting Information, Figure 4.S4). This overlithiated product was characterized by XRD to reveal a featureless spectrum when compared to the pristine NMC material (Supporting Information, Figure 4.S5). It has previously been reported that similar overlithiation via the conversion reaction of $LiCoO_2$ material resulted in nanoscale metal domains that were smaller than the coherence of the X-rays, resulting in similar featureless spectra.[29] XPS of the samples show a clear redshift after overlithiation. The peaks positions of Ni at 852.5 eV, Mn at 639.6 eV, and Co at 776.6 eV (Supporting Information, Figure 4.S6) are consistence with what is generally reported for the metallic chemical state of these

elements,[30],[31],[32] and supports the hypothesis that nanodomains of metal Ni, Mn, and Co are mixed with nonconductive Li_2O.

Figure 4.S4: SEM images of an NMC secondary particle before and after overlithiation by direct contact with Li metal which results in large volume expanse an pulverization of the secondary particle. **b)** XRD spectrum of the pristine and overlithiated NMC material. **c)** XPS spectra for Ni, Mn, and Co showing a clear redshift as the transition metals are reduced to their metallic chemical states.

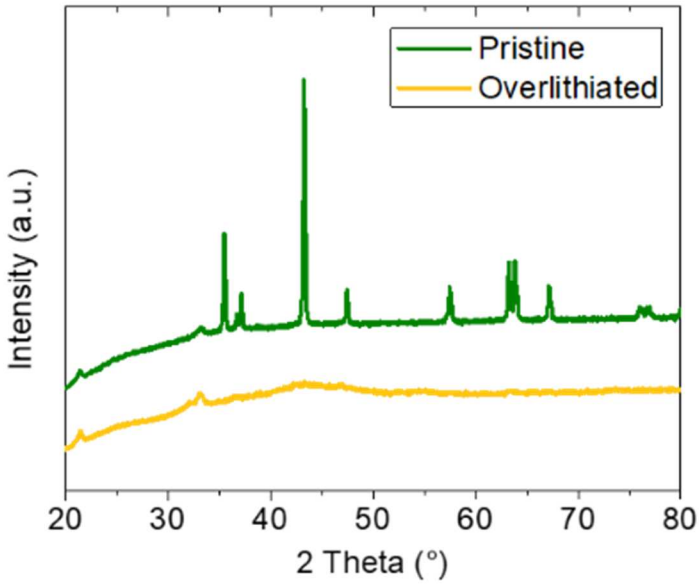

Figure 4.S5: XRD spectrum of the pristine and overlithiated NMC material.

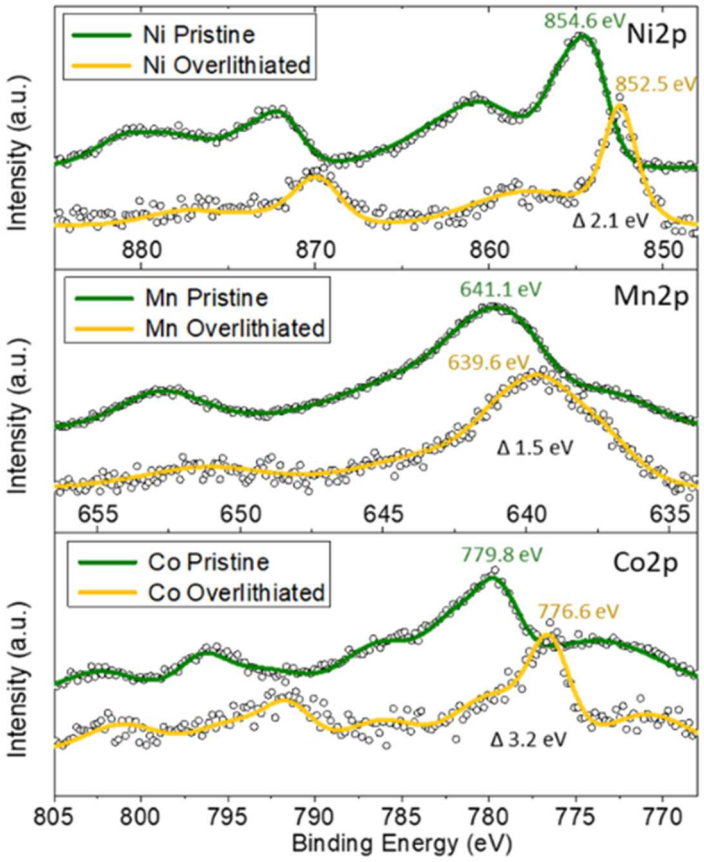

Figure 4.S6: XPS spectra for Ni, Mn, and Co showing a clear redshift as the transition metals are reduced to their metallic chemical states.

While the etching process is not expected to damage the active material since oxides are generally more difficult to remove than carbon and polymer s pecies,[33] electrochemical cycling of the cathodes was carried out to ensure the etching process has no adverse effects on the cathode performance **(Figure 4.3)**. Tests were performed using Li metal as the anode and LP30 as the electrolyte (1 M $LiPF_6$ EC:DMC 1:1 wt%). There is no notable difference between any etched cathodes and the pristine (0-minute etched) cathode during the formation cycle and the 3rd cycle **(Figure 4.3a)** when cycled at a rate of C/10. It should be noted that there is an initial hump in the

voltage profile during the initial formation charging step which appeared in all samples whether etched or unetched. This is often attributed to the aging of cathode that have been exposed to atmospheric moisture and CO_2 for some time, in this case over two years. However, this hump disappears in subsequent cycles and the cathode performance still appears quite good. Since the carbon network provides the necessary electronic conductivity to cycle at high current densities, the cathodes were tested at rates of C/5, C/3, and 1C, again with no apparent difference in cycling performance. As seen in **Figure 4.2**, the conductive carbon network remains on the underside of the surface-most particles even after 30 minutes of etching and provides the necessary electronic pathway to maintain normal performance.

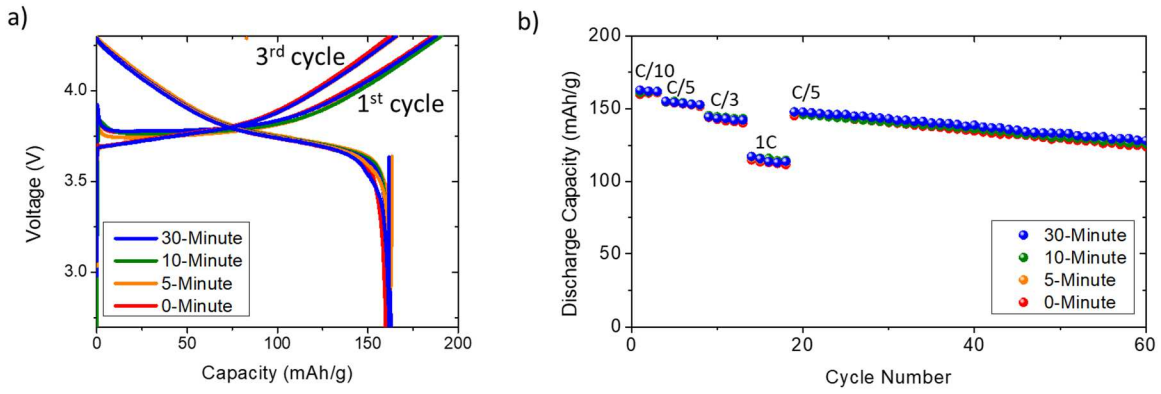

Figure 4.3: a) 1st and 3rd cycle voltage profile and **b)** cycling stability and capacity retention at different rates for the various durations of carbon etching.

EIS of the pristine and 30-minute etched cathode show less than 1 Ωcm^2 in the high frequency region and only a minor increase in the cathode charge transfer resistance due to the surface etching but does not appear to significantly effect performance at normal current densities (Supporting Information, Figure 4.S7). Long-term cycling was carried out at a rate of C/5 and

again shows no apparent difference between any of the cathode samples over the subsequent 50 cycles.

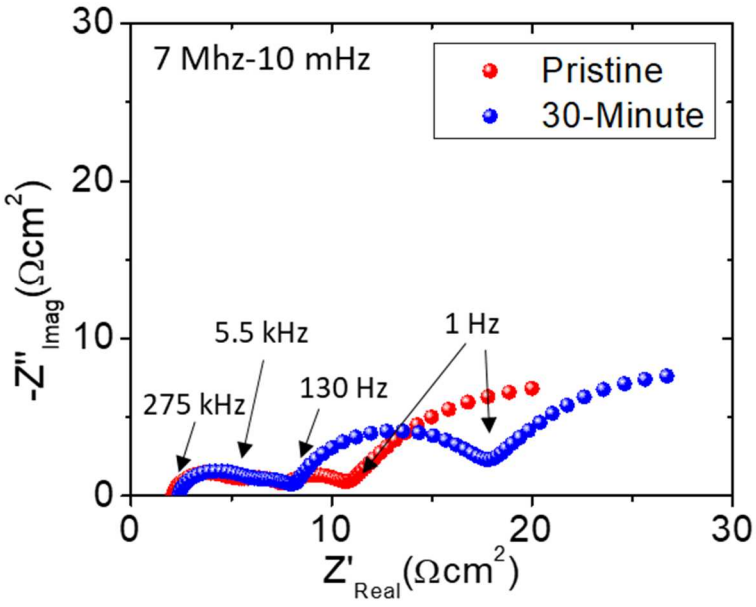

Figure 4.S7: Electrochemical impedance spectroscopy of the pristine and etched cathodes when charged to ~50% S.O.C.

We use an abuse charging protocol to intentionally induce internal dendritic shorting **(Figure 4.4)**. A schematic of the abuse charging set up is shown in **Figure 4.4a**, where a thermocouple is taped to the outer casing of a standard NMC/Li metal coincell to measure tremperature rise, which is then placed in a thermally insulated sheath. **Figure 4.4b** shows an example voltage vs time trace (30-minute etched, 3rd cycle). All batteries were subjected to identical conditions: pre-cycling at a rate of C/3, with a discharge to 3.5 V. The batteries were then subjected to 4.5 V potentiostatic abuse charging step for 15 minutes. By using a potentiostatic hold as opposed to a galvanostatic s cheme, current is allowed to freely flow during the charge process.

This in turn deposites highly dendritic Li on the anode surface which quickly grows to penetrate the separator and short the cell within a matter of minutes.

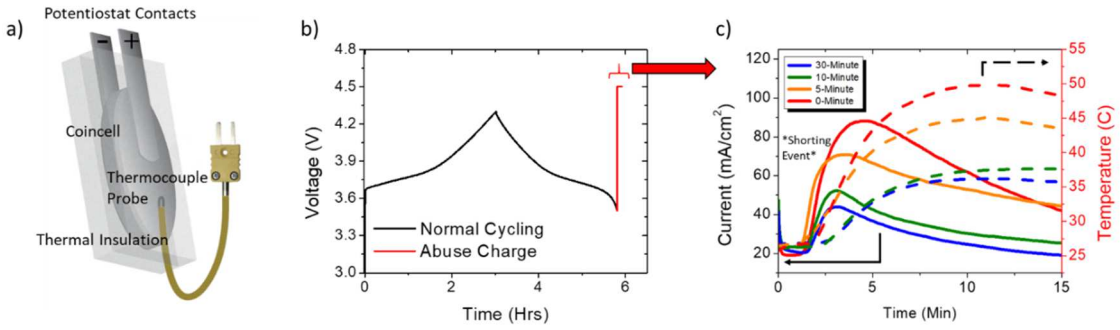

Figure 4.4: Abuse shorting tests. a) Schematic of the abuse charging experimental set up where a thermocouple is attached to the outer coincell casing, which is then placed in a thermally insulating sheath. **b)** Example voltage vs time profile, where cells are normally cycled to a discharge state then subjected to a 4.5 V potentiostatic abuse charging step. **c)** The corresponding potentiostatic abuse charging current and cell temperature profile.

The potentiostatic abuse charging current profiles as well as cell temperture profiles for electrodes prepared with varying etching times are plotted in **Figure 4.4c**. For all cathodes shorting occurred between 2 and 3 minutes due to an extremely high average current density > 20 mA/cm^2, which equates to a charging rate of greater than 10C. When internal shorting was established, the pristine cathode reached a peak current denisty of nearly 90 mA/cm^2 with an accompanying cell temperature rising to over 50 °C. The 30-minute etched cathode was limited to a short current density of 43 mA/cm^2 with the accompanying temperature remaining below 35 °C. The 10-minute etching current-temperature profile was similar, albeit slightly higher by about 10 mA/cm^2 than the 30-minute etched. This matches previous EDS elemental C mapping and conductivity measurements. The 5-minute etching, while managing to mitigate some short circuit current, is

more similar to the pristine cathode, which is also in line with previous carbon content observations. Surface carbon is removed during the 5-minute etch, yet enough carbon remains below the immediate surface to induce significant shorting.

Upon disassembling the cells after abuse shorting test, multiple dendrite contact areas were observed on the 30-minute etched cathode surface **(Figure 4.5a)**. Furthermore, the pristine cathode surface shows nearly identical shorting behavior (Supporting Information, Figure 4.S7). These images show that shorting took place at multiple spots and lithium dendrites appear to grow laterally on the electrode surface. By FIB-SEM cross-section milling of the dendrite/cathode interface and observing this area at an angle (52 °) the lateral growth of these dendrites is clearly seen (Figure 4.5b). Importantly, the short does not appear to penetrate into the depth of the cathode which allows the surface etching strategy to be successful. Furthermore, it is suspected that Li metal continues to deposit on the cathode surface after the short is initiated increasing the shorting area. As the effective shorting area grows, as well as new contacts are initiate, an increase in I_{SC} occurs as seen in **Figure 4.4c**. Once the remaining capacity is expended from the cathode, short growth ceases and the current begins to decay as the highly reactive interface begins to passivate.

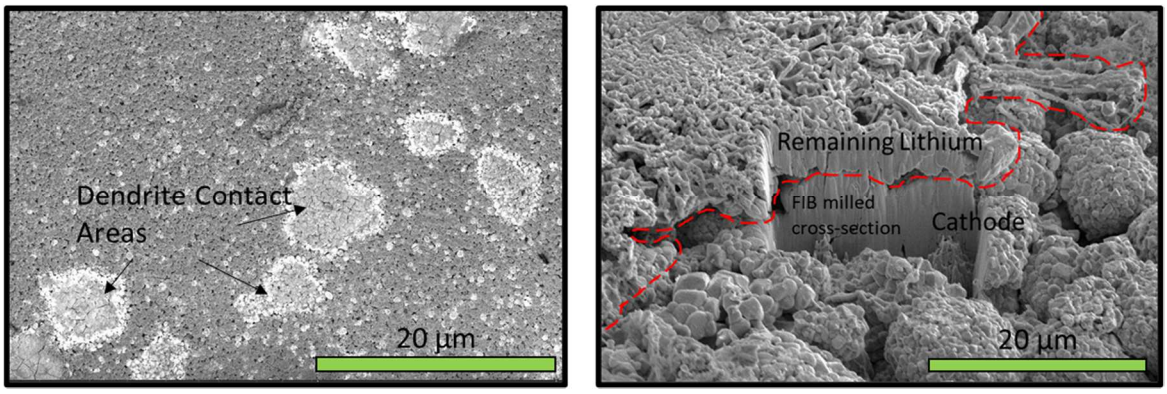

Figure 4.5: Post-morterm analysis of internal shorting. a) SEM image of the 30-minute etched cathode surface after abuse charging showing multiple dendrite contact areas resulting in severe shorting. **b)** FIB-SEM milled cross-section of the dendrite/cathode interface showing a the dendrite remains on the surface and grows laterally without penetrating into the cathode.

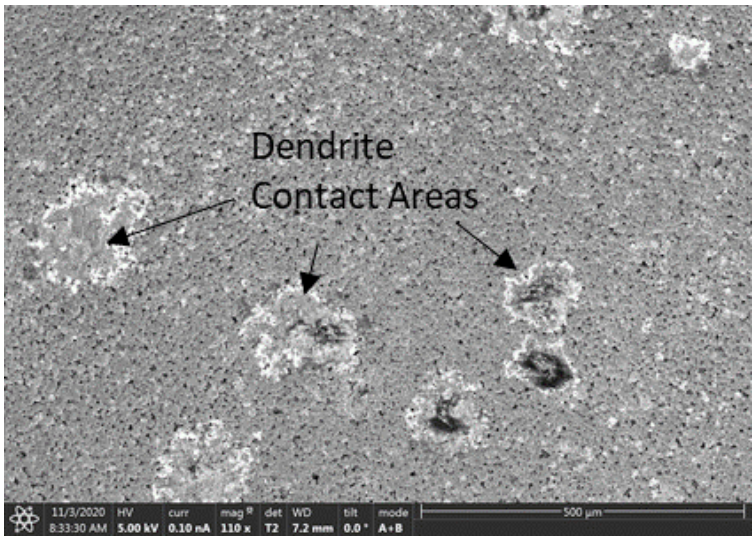

Figure 4.S8: Postmortem SEM of pristine 0-minute etched cathode after abuse shorting showing nearly identical shorting behavior to the etched cathode.

We have presented a new design to mitigate the impact of internal shorting in order to improve lithium battery safety. By selectively etching away the conductive carbon network only

at the surface of the cathode, we create a cathode with an electronic conductivity gradient with the top layer processing reduced conductivity. Etching is limited to roughly 10 μm of depth into the cathode, and the surface-most particles remain electronically connected to the bulk via their underside. This design allows the cathode to maintain normal performance. The presence of a top layer with reduced electronic conductivity results in a significantly higher short circuit resistance which is evident during abuse charging induced shorting experiments, where optimally etched cathode had > 2x reduction in short circuit current and accompanying cell temperature rise. Postmortem SEM characterization of the cathodes reveal a failure mechanism caused by growth of numerous dendritic shorts; however, these contact areas appear to only grow laterally on the cathode surface without penetrating into the bulk of the cathode. This protection scheme is applicable to any common commercial cathode tape that uses a conductive carbon network. The method is simple and scalable, without negatively impacting battery energy density.

Experimental Section

Cathode Details: The cathode is approximately 50 μm thick with a capacity of 2.2 mAh cm^{-2} and contains NMC532 ($Li_xNi_{0.5}Mn_{0.3}Co_{0.2}O_2$), MWCNTs (multiwalled carbon nanotubes), and PVDF (Polyvinylidene fluoride) in a mass ratio of 97.5:1:1.5 on Al foil (Hunan Hong Xiang New Energy Technology CO.LTD).

Etching Details: Roughly 10 cm x 10 cm squares of the cathode tape were cut and placed into the vacuum chamber of a Ladd / Hummer™ 6.2 sputter coat machine equipped with sacrificial Al target and Ar gas. The vacuum chamber was evacuated to 80 mTorr with a steady flow of Ar

and 5, 10, or 30 minutes of reversed polarity sputter etching was performed at a current of 10 mA to remove surface carbon.

4-Probe Measurements: Sheet resistance measurements were collected using 0.5 cm wide, 0.05 cm thick freestanding cathodes with thin strips of conductive Cu tape spaced 0.25 cm apart as electrical contacts. Various currents ranging from 1 μA to 10 mA were applied between the outer two contacts, and the voltage between the inner two was measured. This was convert to resistance, sheet resistance, and conductivity using the formula described in the main text.

Coin Cell Assembly, Cycling, Abuse Shorting Testing: Coin cells were assembled within an Ar atmosphere glovebox (O_2 < 1 ppm, H_2O < 1 ppm) with 2032 stainless steel casings and used 13 mm diameter cathodes paired with a 15 mm diameter Li disk rolled onto a 1 mm thick stainless steel spacer disk. 1.0 M LiPF6 in 1:1 vol/vol ethylene carbonate (EC) and dimethyl carbonate (DMC) (LP30, Gotion) was used as the electrolyte. The cell was sealed in a hydraulic crimper at 1000 psi. Coin cells were cycled using a Landt battery tester. Coin cells the potentiostatic tests were precycled at a rate of C/10 for the first cycle and C/3 for the following two cycles (3rd cycle cut-off was set to 3.5 V). Potentiostatic holds and impedance measurements were carried with a Biologic potentiostat using a high current (10 A, 5V) booster channel. Temperature was measured using a K-type thermocouple and HOBOware reader.

XPS Characterization: XPS spectra (Supporting Information, Figure 4.S6) used to calculate the doping level of iongate material was performed by a PHI Quantera SXM, Scanning X-ray Microprobe and was carried out using Al anode source at 15 kV and all the peaks were fitted based on the reference C–C bond at 284.6 eV. All XPS measurements were collected with a 300 mm × 700 mm spot size using a charge neutralizer during acquisition. Survey scans were

collected with a 1.0 eV step size, and were followed by high resolution scans with a step size of 0.05 eV for Ni2p, Co2p, and Mn2p regions.

Acknowledgements:

P.L. proposed the idea and directed the research along with H.L. All of the authors contributed to the planning, materials fabrication, experimental design and analysis, and manuscript preparation. M.S.G. performed the majority of separator fabrication and characterization as well as cell fabrication, and electrochemical testing. Z.W. and Q.Y. aided in characterization and cell design. J.H. helped in experimental design and analyzing results. The majority of cell fabrication and electrochemical testing was performed in the UCSD-MTI Battery Fabrication and the UCSD-Arbin Battery Testing Facility. We acknowledge Hunan Hong Xiang New Energy Technology CO.LTD for supplying high capacity NMC cathode tapes.

Chapter 4, in full, has been submitted to Advanced Materials 2021. M. S. Gonzalez, Z. Wu, J. Holoubek, Q. Yan, H. Liu, P. Liu. The dissertation author was the primary investigator and author of this material.

References

Chapter 1:

[1] Halmo, P.M., Zhang, X., Vido, P.D., Zhang, Z., Shi, L., Alexander, D.R., Watson, J.V., 2017. Thin battery separators and methods. US9666847B2.

[2] M. Singh, J. Kaiser, H. Hahn, *J. Electrochem. Soc.* **2015**, *162*, A1196.

[3] P. Li, G. Zhao, X. Zheng, X. Xu, C. Yao, W. Sun, S. X. Dou, *Energy Storage Materials* **2018**, *15*, 422.

[4] X.-B. Cheng, R. Zhang, C.-Z. Zhao, Q. Zhang, *Chem. Rev.* **2017**, *117*, 10403.

[5] K. Liu, Y. Liu, D. Lin, A. Pei, Y. Cui, *Science Advances* **2018**, *4*, eaas9820.

[6] D. Ouyang, M. Chen, J. Liu, R. Wei, J. Weng, J. Wang, *RSC Adv.* **2018**, *8*, 33414.

[7] B. Liu, Y. Jia, J. Li, S. Yin, C. Yuan, Z. Hu, L. Wang, Y. Li, J. Xu, *J. Mater. Chem. A* **2018**, *6*, 21475.

[8] H. Maleki, J. N. Howard, *Journal of Power Sources* **2009**, *191*, 568.

[9] P. Ghosh, "Hyundai To Recall 76,000 Electric Vehicles Over Battery Fire Risks," can be found under https://www.forbes.com/sites/palashghosh/2021/02/24/hyundai-to-recall-76000-electric-vehicles-over-battery-fire-risks/ Accessed April 2021.

[10] "Global Automotive Lithium Ion Battery Pack Market Size & Forecast 2025 - Valuates Reports," can be found under https://reports.valuates.com/market-reports/QYRE-Auto-0U1490/global-automotive-lithium-ion-battery, Accessed March 2021

[11] Q. Wang, P. Ping, X. Zhao, G. Chu, J. Sun, C. Chen, *Journal of Power Sources* **2012**, *208*, 210.

[12] W. Na, A. S. Lee, J. H. Lee, S. S. Hwang, E. Kim, S. M. Hong, C. M. Koo, *ACS Appl. Mater. Interfaces* **2016**, *8*, 12852.

[13] W. Yi, Z. Huaiyu, H. Jian, L. Yun, Z. Shushu, *Journal of Power Sources* **2009**, *189*, 616.

[14] A. Gogia, Y. Wang, A. K. Rai, R. Bhattacharya, G. Subramanyam, J. Kumar, *ACS Omega* **2021**, *6*, 4204.

[15] C. Shi, J. Dai, X. Shen, L. Peng, C. Li, X. Wang, P. Zhang, J. Zhao, *Journal of Membrane Science* **2016**, *517*, 91.

[16] K. Liu, D. Zhuo, H.-W. Lee, W. Liu, D. Lin, Y. Lu, Y. Cui, *Advanced Materials* **2017**, *29*, 1603987.

[17] H. Wu, D. Zhuo, D. Kong, Y. Cui, *Nature Communications* **2014**, *5*, 5193.

[18] L. Kong, B. Liu, J. Ding, X. Yan, G. Tian, S. Qi, D. Wu, *Journal of Membrane Science* **2018**, *549*, 244.

[19] M. Naguib, S. Allu, S. Simunovic, J. Li, H. Wang, N. J. Dudney, *Joule* **2018**, *2*, 155.

[20] Z. Chen, P.-C. Hsu, J. Lopez, Y. Li, J. W. F. To, N. Liu, C. Wang, S. C. Andrews, J. Liu, Y. Cui, Z. Bao, *Nature Energy* **2016**, *1*, 1.

[21] X. M. Feng, X. P. Ai, H. X. Yang, *Electrochemistry Communications* **2004**, *6*, 1021.

[22] H. Zhong, C. Kong, H. Zhan, C. Zhan, Y. Zhou, *Journal of Power Sources* **2012**, *216*, 273.

[23] M. S. Gonzalez, Q. Yan, J. Holoubek, Z. Wu, H. Zhou, N. Patterson, V. Petrova, H. Liu, P. Liu, *Advanced Materials* **2020**, *32*, 1906836.

Chapter 2:

[1] J. A. McAl lister, A. E. Farrell, *Energy* **2007**, *32*, 1177.

[2] W. Cole, A. Frazier, *Cost Projections for Utility-Scale Battery Storage: 2020 Update*, National Renewable Energy Lab. (NREL), Golden, CO (United States), **2020**.

[3] "Lithium-ion Batteries — Market Report," can be found under https://roskill.com/market-report/lithium-ion-batteries/

[4] T. Markel, *Plug-in Electric Vehicle Infrastructure: A Foundation for Electrified Transportation: Preprint*, National Renewable Energy Lab. (NREL), Golden, CO (United States), **2010**.

[5] B. Kroposki, G. Martin, *IEEE PES General Meeting* **2010**, DOI 10.1109/PES.2010.5589753.

[6] M. R. Palacín, A. de Guibert, *Science* **2016**, *351*, DOI 10.1126/science.1253292.

[7] S.-M. Bak, E. Hu, Y. Zhou, X. Yu, S. D. Senanayake, S.-J. Cho, K.-B. Kim, K. Y. Chung, X.-Q. Yang, K.-W. Nam, *ACS Appl. Mater. Interfaces* **2014**, *6*, 22594.

[8] T. Bowen, I. Chernyakhovskiy, P. Denholm, Grid-Scale Battery Storage: Frequently Asked Questions**.**, 8.

[9] L. Zhou, Y. Zheng, M. Ouyang, L. Lu, *Journal of Power Sources* **2017**, *364*, 242.

[10] W. Sung, K.-Y. Park, M. Lee, S. Moon, K. Oh, H. Park, L. Sechan, K. Kang, *Energy & Environmental Science* **2018**, *11*, DOI 10.1039/C8EE00186C.

[11] G. Pistoia, A. Antonini, R. Rosati, D. Zane, *Electrochimica Acta* **1996**, *41*, 2683.

[12] A. Blyr, C. Sigala, G. Amatucci, D. Guyomard, Y. Chabre, J.-M. Tarascon, *J. Electrochem. Soc.* **1998**, *145*, 194.

[13] W. Li, J. Hicks-Garner, J. Wang, J. Liu, A. Gross, E. Sherman, J. Graetz, J. Vajo, P. Liu, *Chemistry of Materials* **2014**, *26*, 3403.

[14] I. Bauer, M. Kohl, H. Althues, S. Kaskel, *Chem. Commun.* **2014**, *50*, 3208.

[15] H. Maleki, J. N. Howard, *Journal of Power Sources* **2009**, *191*, 568.

[16] P. Sun, R. Bisschop, H. Niu, X. Huang, *Fire Technol* **2020**, *56*, 1361.

[17] C. Negroni, "Boeing Dreamliner's Lithium-Ion Battery Fails On United Flight To Paris," can be found under

https://www.forbes.com/sites/christinenegroni/2017/12/01/dreamliners-beleaguered-lithium-ion-battery-creates-problem-on-united-flight-to-paris/,

[18] D. J. Noelle, M. Wang, A. V. Le, Y. Shi, Y. Qiao, *Applied Energy* **2018**, *212*, 796.

[19] Q. Wang, P. Ping, X. Zhao, G. Chu, J. Sun, C. Chen, *Journal of Power Sources* **2012**, *208*, 210.

[20] M. Wang, A. V. Le, Y. Shi, D. J. Noelle, Y. Qiao, *Appl. Phys. Lett.* **2017**, *110*, 083902.

[21] Z. Chen, P.-C. Hsu, J. Lopez, Y. Li, J. W. F. To, N. Liu, C. Wang, S. C. Andrews, J. Liu, Y. Cui, Z. Bao, *Nature Energy* **2016**, *1*, 1.

[22] P. Yan, Y. Zhu, X. Pan, H. Ji, *International Journal of Energy Research* **2021**, *45*, 2776.

[23] Y. E. Hyung, D. R. Vissers, K. Amine, *Journal of Power Sources* **2003**, *119–121*, 383.

[24] B. Wu, F. Pei, Y. Wu, R. Mao, X. Ai, H. Yang, Y. Cao, *Journal of Power Sources* **2013**, *227*, 106.

[25] X. Li, W. Li, L. Chen, Y. Lu, Y. Su, L. Bao, J. Wang, R. Chen, S. Chen, F. Wu, *Journal of Power Sources* **2018**, *378*, 707.

[26] J. R. Dahn, J. Jiang, L. M. Moshurchak, M. D. Fleischauer, C. Buhrmester, L. J. Krause, *J. Electrochem. Soc.* **2005**, *152*, A1283.

[27] J. Ding, T. Tian, Q. Meng, Z. Guo, W. Li, P. Zhang, F. T. Ciacchi, J. Huang, W. Yang, *Scientific Reports* **2013**, *3*, 2485.

[28] T.-H. Yu, *Trilayer Shutdown Battery Separator and Process of Manufacture*, **1999**, EP0951080A1.

[29] H. Wu, D. Zhuo, D. Kong, Y. Cui, *Nature Communications* **2014**, *5*, 5193.

[30] M. S. Gonzalez, Q. Yan, J. Holoubek, Z. Wu, H. Zhou, N. Patterson, V. Petrova, H. Liu, P. Liu, *Advanced Materials* **2020**, *32*, 1906836.

[31] C. Deslouis, T. El Moustafid, M. M. Musiani, B. Tribollet, *Electrochimica Acta* **1996**, *41*, 1343.

[32] P. Burgmayer, R. W. Murray, *J. Phys. Chem.* **1984**, *88*, 2515.

[33] C. Weidlich, K.-M. Mangold, *Electrochimica Acta* **2011**, *56*, 3481.

[34] M. E. Abdelhamid, A. P. O'Mullane, G. A. Snook, *RSC Adv.* **2015**, *5*, 11611.

[35] Z. Wang, R. Pan, C. Ruan, K. Edström, M. Strømme, L. Nyholm, *Advanced Science* **2018**, *5*, 1700663.

[36] X.-W. Gao, Y.-F. Deng, D. Wexler, G.-H. Chen, S.-L. Chou, H.-K. Liu, Z.-C. Shi, J.-Z. Wang, *J. Mater. Chem. A* **2014**, *3*, 404.

[37] F.-H. Du, B. Li, W. Fu, Y.-J. Xiong, K.-X. Wang, J.-S. Chen, *Advanced Materials* **2014**, *26*, 6145.

[38] L. Qie, L.-X. Yuan, W.-X. Zhang, W.-M. Chen, Y.-H. Huang, *J. Electrochem. Soc.* **2012**, *159*, A1624.

[39] C. Wang, W. Zheng, Z. Yue, C. O. Too, G. G. Wallace, *Advanced Materials* **2011**, *23*, 3580.

[40] T. Patois, B. Lakard, S. Monney, X. Roizard, P. Fievet, *Synthetic Metals* **2011**, *161*, 2498.

[41] H. Lee, S. M. Dellatore, W. M. Miller, P. B. Messersmith, *Science* **2007**, *318*, 426.

[42] W. Zhang, F. Yang, Z. Pan, J. Zhang, B. Zhao, *Macromolecular rapid communications* **2014**, *35*, DOI 10.1002/marc.201300761.

[43] K. Semin, L. Jang, H. Park, J. Y. Lee, *Scientific Reports* **2016**, *6*, 30475.

[44] S. J. An, J. Li, C. Daniel, S. Kalnaus, D. L. Wood, *J. Electrochem. Soc.* **2017**, *164*, A1755.

[45] J. Shim, R. Kostecki, T. Richardson, X. Song, K. A. Striebel, *Journal of Power Sources* **2002**, *112*, 222.

[46] B. A. Johnson, R. E. White, *Journal of Power Sources* **1998**, *70*, 48.

[47] P. Bai, J. Li, F. R. Brushett, M. Z. Bazant, *Energy Environ. Sci.* **2016**, *9*, 3221.

[48] R. May, Y. Zhang, S. R. Denny, V. Viswanathan, L. E. Marbella, *Cell Reports Physical Science* **2020**, *1*, 100239.

[49] P. Camurlu, *RSC Adv.* **2014**, *4*, 55832.

Chapter 3:

[1] J. A. McAllister, A. E. Farrell, *Energy* **2007**, *32*, 1177.

[2] T. Markel, *Plug-in Electric Vehicle Infrastructure: A Foundation for Electrified Transportation: Preprint*, National Renewable Energy Lab. (NREL), Golden, CO (United States), **2010**.

[3] B. Kroposki, G. Martin, in *IEEE PES General Meeting*, **2010**, pp. 1–4.

[4] P. M. Halmo, X. Zhang, P. D. Vido, Z. Zhang, L. Shi, D. R. Alexander, J. V. Watson, *Thin Battery Separators and Methods*, **2017**, US9666847B2.

[5] M. Singh, J. Kaiser, H. Hahn, *J. Electrochem. Soc.* **2015**, *162*, A1196.

[6] P. Li, G. Zhao, X. Zheng, X. Xu, C. Yao, W. Sun, S. X. Dou, *Energy Storage Materials* **2018**, *15*, 422.

[7] X.-B. Cheng, R. Zhang, C.-Z. Zhao, Q. Zhang, *Chem. Rev.* **2017**, *117*, 10403.

[8] K. Liu, Y. Liu, D. Lin, A. Pei, Y. Cui, *Science Advances* **2018**, *4*, eaas9820.

[9] D. H. Doughty, Vehicle Battery Safety Roadmap Guidance, National Renewable Energy Lab. (NREL), Golden, CO (United States), 2012.

[10] H. Maleki, J. N. Howard, *Journal of Power Sources* **2009**, *191*, 568.

[11] S.-M. Bak, E. Hu, Y. Zhou, X. Yu, S. D. Senanayake, S.-J. Cho, K.-B. Kim, K. Y. Chung, X.-Q. Yang, K.-W. Nam, *ACS Appl. Mater. Interfaces* **2014**, *6*, 22594.

[12] R. Spotnitz, J. Franklin, *Journal of Power Sources* **2003**, *113*, 81.

[13] W. Zhao, G. Luo, C.-Y. Wang, *J. Electrochem. Soc.* **2015**, *162*, A207.

[14] T. Yokoshima, D. Mukoyama, F. Maeda, T. Osaka, K. Takazawa, S. Egusa, S. Naoi, S. Ishikura, K. Yamamoto, *Journal of Power Sources* **2018**, *393*, 67.

[15] https://www.bloomberg.com/news/articles/2019-05-16/tesla-updates-software-after-parked-car-caught-fire-in-hong-kong

[16] J. Steiger, D. Kramer, R. Mönig, *Journal of Power Sources* **2014**, *261*, 112.

[17] H. Kato, Y. Yamamoto, Y. Nishi, 184th ECS Fall Meeting, vol. 93-2, New Orleans, 1993 (Ext. Abstr. 22).

[18] M. Naguib, S. Allu, S. Simunovic, J. Li, H. Wang, N. J. Dudney, *Joule* **2018**, *2*, 155.

[19] P. Arora, Z. (John) Zhang, *Chem. Rev.* **2004**, *104*, 4419.

[20] N. Kanhere, K. Rafiz, G. Sharma, Z. Sun, Y. Jin, Y. S. Lin, *Powder Technology* **2019**, *353*, 230.

[21] Z. Chen, P.-C. Hsu, J. Lopez, Y. Li, J. W. F. To, N. Liu, C. Wang, S. C. Andrews, J. Liu, Y. Cui, Z. Bao, *Nature Energy* **2016**, *1*, 15009.

[22] H. Wu, D. Zhuo, D. Kong, Y. Cui, *Nature Communications* **2014**, *5*, 5193.

[23] A. Jana, D. R. Ely, R. E. García, *Journal of Power Sources* **2015**, *275*, 912.

[24] X.-B. Cheng, T.-Z. Hou, R. Zhang, H.-J. Peng, C.-Z. Zhao, J.-Q. Huang, Q. Zhang, *Adv. Mater.* **2016**, *28*, 2888.

[25] W. Na, A. S. Lee, J. H. Lee, S. S. Hwang, E. Kim, S. M. Hong, C. M. Koo, *ACS Appl. Mater. Interfaces* **2016**, *8*, 12852.

[26] H. Lee, M. Yanilmaz, O. Toprakci, K. Fu, X. Zhang, *Energy Environ. Sci.* **2014**, *7*, 3857.

[27] D. Lin, Y. Liu, Y. Cui, *Nature Nanotechnology* **2017**, *12*, 194.

[28] K. Liu, Y. Liu, D. Lin, A. Pei, Y. Cui, *Science Advances* **2018**, *4*, eaas9820.

[29] T. Nestler, R. Schmid, W. Münchgesang, V. Bazhenov, J. Schilm, T. Leisegang, D. C. Meyer, AIP Conference Proceedings 2014, 1597, 155.

[30] Z. Zhang, *Separator for a High Energy Rechargeable Lithium Battery*, **2002**, US6432586B1.

[31] M. M. Rahman, S. Mateti, Q. Cai, I. Sultana, Y. Fan, X. Wang, C. Hou, Y. Chen, *Energy Storage Materials* **2019**, *19*, 352.

[32] C. Wang, G. Bai, Y. Yang, X. Liu, H. Shao, *Nano Res.* **2019**, *12*, 217.

[33] F. Han, A. S. Westover, J. Yue, X. Fan, F. Wang, M. Chi, D. N. Leonard, N. J. Dudney, H. Wang, C. Wang, *Nature Energy* **2019**, *4*, 187.

[34] A. S. Gozdz, C. N. Schmutz, J.-M. Tarascon, P. C. Warren, *Polymeric Electrolytic Cell Separator Membrane*, **1995**.

[35] J.-M. Tarascon, A. S. Gozdz, C. Schmutz, F. Shokoohi, P. C. Warren, *Solid State Ionics* **1996**, *86–88*, 49.

[36] J.-H. Cao, B.-K. Zhu, Y.-Y. Xu, *Journal of Membrane Science* **2006**, *281*, 446.

[37] R. Jung, M. Metzger, F. Maglia, C. Stinner, H. A. Gasteiger, *J. Phys. Chem. Lett.* **2017**, *8*, 4820.

[38] P. Xie, P. Gu, J. J. Beaudoin, *JOURNAL OF MATERIALS SCIENCE* **1996**, *31*, 4093.

[39] S. Jiao, J. Zheng, Q. Li, X. Li, M. H. Engelhard, R. Cao, J.-G. Zhang, W. Xu, *Joule* **2018**, *2*, 110.

[40] P. Bai, J. Li, F. R. Brushett, M. Z. Bazant, *Energy & Environmental Science* **2016**, *9*, 3221

[41] K. N. Wood, E. Kazyak, A. F. Chadwick, K.-H. Chen, J.-G. Zhang, K. Thornton, N. P. Dasgupta, *ACS Cent. Sci.* **2016**, *2*, 790.

[42] C. Fang, J. Li, M. Zhang, Y. Zhang, F. Yang, J. Z. Lee, M.-H. Lee, J. Alvarado, M. A. Schroeder, Y. Yang, B. Lu, N. Williams, M. Ceja, L. Yang, M. Cai, J. Gu, K. Xu, X. Wang, Y. S. Meng, *Nature* **2019**, *572*, 511.

[42] B. Song, I. Dhiman, J. C. Carothers, G. M. Veith, J. Liu, H. Z. Bilheux, A. Huq, *ACS Energy Lett.* **2019**, *4*, 2402.

[43] V. Ruiz, A. Pfrang, A. Kriston, N. Omar, P. Van den Bossche, L. Boon-Brett, *Renewable and Sustainable Energy Reviews* **2018**, *81*, 1427.

[44] D. J. Noelle, M. Wang, A. V. Le, Y. Shi, Y. Qiao, *Applied Energy* **2018**, *212*, 796.

[45] P. Bai, J. Li, F. R. Brushett, M. Z. Bazant, *Energy Environ. Sci.* **2016**, *9*, 3221.

[46] V. Srinivasan, C. Y. Wang, *J. Electrochem. Soc.* **2003**, *150*, A98.

[47] S. L. Morelly, N. J. Alvarez, M. H. Tang, *Journal of Power Sources* **2018**, *387*, 49.

Chapter 4:

[1] Halmo, P.M., Zhang, X., Vido, P.D., Zhang, Z., Shi, L., Alexander, D.R., Watson, J.V., 2017. Thin battery separators and methods. US9666847B2.

[2] M. Singh, J. Kaiser, H. Hahn, *J. Electrochem. Soc.* **2015**, *162*, A1196.

[3] P. Li, G. Zhao, X. Zheng, X. Xu, C. Yao, W. Sun, S. X. Dou, *Energy Storage Materials* **2018**, *15*, 422.

[4] X.-B. Cheng, R. Zhang, C.-Z. Zhao, Q. Zhang, *Chem. Rev.* **2017**, *117*, 10403.

[5] K. Liu, Y. Liu, D. Lin, A. Pei, Y. Cui, *Science Advances* **2018**, *4*, eaas9820.

[6] D. Ouyang, M. Chen, J. Liu, R. Wei, J. Weng, J. Wang, *RSC Adv.* **2018**, *8*, 33414.

[7] B. Liu, Y. Jia, J. Li, S. Yin, C. Yuan, Z. Hu, L. Wang, Y. Li, J. Xu, *J. Mater. Chem. A* **2018**, *6*, 21475.

[8] H. Maleki, J. N. Howard, *Journal of Power Sources* **2009**, *191*, 568.

[9] P. Ghosh, "Hyundai To Recall 76,000 Electric Vehicles Over Battery Fire Risks," can be found under https://www.forbes.com/sites/palashghosh/2021/02/24/hyundai-to-recall-76000-electric-vehicles-over-battery-fire-risks/ Accessed April 2021.

[10] "Global Automotive Lithium Ion Battery Pack Market Size & Forecast 2025 - Valuates Reports," can be found under https://reports.valuates.com/market-reports/QYRE-Auto-0U1490/global-automotive-lithium-ion-battery, Accessed March 2021

[11] Q. Wang, P. Ping, X. Zhao, G. Chu, J. Sun, C. Chen, *Journal of Power Sources* **2012**, *208*, 210.

[12] W. Na, A. S. Lee, J. H. Lee, S. S. Hwang, E. Kim, S. M. Hong, C. M. Koo, *ACS Appl. Mater. Interfaces* **2016**, *8*, 12852.

[13] W. Yi, Z. Huaiyu, H. Jian, L. Yun, Z. Shushu, *Journal of Power Sources* **2009**, *189*, 616.

[14] A. Gogia, Y. Wang, A. K. Rai, R. Bhattacharya, G. Subramanyam, J. Kumar, *ACS Omega* **2021**, *6*, 4204.

[15] C. Shi, J. Dai, X. Shen, L. Peng, C. Li, X. Wang, P. Zhang, J. Zhao, *Journal of Membrane Science* **2016**, *517*, 91.

[16] K. Liu, D. Zhuo, H.-W. Lee, W. Liu, D. Lin, Y. Lu, Y. Cui, *Advanced Materials* **2017**, *29*, 1603987.

[17] H. Wu, D. Zhuo, D. Kong, Y. Cui, *Nature Communications* **2014**, *5*, 5193.

[18] L. Kong, B. Liu, J. Ding, X. Yan, G. Tian, S. Qi, D. Wu, *Journal of Membrane Science* **2018**, *549*, 244.

[19] M. Naguib, S. Allu, S. Simunovic, J. Li, H. Wang, N. J. Dudney, *Joule* **2018**, *2*, 155.

[20] Z. Chen, P.-C. Hsu, J. Lopez, Y. Li, J. W. F. To, N. Liu, C. Wang, S. C. Andrews, J. Liu, Y. Cui, Z. Bao, *Nature Energy* **2016**, *1*, 1.

[21] X. M. Feng, X. P. Ai, H. X. Yang, *Electrochemistry Communications* **2004**, *6*, 1021.

[22] H. Zhong, C. Kong, H. Zhan, C. Zhan, Y. Zhou, *Journal of Power Sources* **2012**, *216*, 273.

[23] M. S. Gonzalez, Q. Yan, J. Holoubek, Z. Wu, H. Zhou, N. Patterson, V. Petrova, H. Liu, P. Liu, *Advanced Materials* **2020**, *32*, 1906836.

[24] K. Dokko, M. Mohamedi, Y. Fujita, T. Itoh, M. Nishizawa, M. Umeda, I. Uchida, *Electrochem Soc* **2001**, *148*, A422.

[25] M. M. Thackeray, *Progress in Solid State Chemistry* **1997**, *25*, 1.

[26] P. P. Prosini, M. Lisi, D. Zane, M. Pasquali, *Solid State Ionics* **2002**, *148*, 45.

[27] Y. Itou, N. Ogihara, S. Kawauchi, *J. Phys. Chem. C* **2020**, *124*, 5559.

[28] R. Benedek, J. Vaughey, M. M. Thackeray, *Chem. Mater.* **2006**, *18*, 1296.

[29] L. Yu, Y. Tian, X. Xiao, C. Hou, Y. Xing, Y. Si, H. Lu, Y. Zhao, *J. Electrochem. Soc.* **2021**, *168*, 050516.

[30] A. P. Grosvenor, M. C. Biesinger, R. St. C. Smart, N. S. McIntyre, *Surface Science* **2006**, *600*, 1771.

[31] L. Baggetto, N. J. Dudney, G. M. Veith, *Electrochimica Acta* **2013**, *90*, 135.

[32] J. C. Dupin, D. Gonbeau, H. Benqlilou-Moudden, P. Vinatier, A. Levasseur, *Thin Solid Films* **2001**, *384*, 23.

[33] S. J. Pearton, D. P. Norton, *Plasma Processes and Polymers* **2005**, *2*, 16.